

Washington University in St. Louis  
**Washington University Open Scholarship**

---

Engineering and Applied Science Theses &  
Dissertations

McKelvey School of Engineering

---


Spring 5-15-2019

# Defect Chemistry and Ion Intercalation During the Growth and Solid-State Transformation of Metal Halide Nanocrystals

Bo Yin

*Washington University in St. Louis*

Follow this and additional works at: [https://openscholarship.wustl.edu/eng\\_etds](https://openscholarship.wustl.edu/eng_etds)

 Part of the [Materials Science and Engineering Commons](#), [Mechanics of Materials Commons](#), [Nanoscience and Nanotechnology Commons](#), and the [Physical Chemistry Commons](#)

---

## Recommended Citation

Yin, Bo, "Defect Chemistry and Ion Intercalation During the Growth and Solid-State Transformation of Metal Halide Nanocrystals" (2019). *Engineering and Applied Science Theses & Dissertations*. 461.  
[https://openscholarship.wustl.edu/eng\\_etds/461](https://openscholarship.wustl.edu/eng_etds/461)

This Dissertation is brought to you for free and open access by the McKelvey School of Engineering at Washington University Open Scholarship. It has been accepted for inclusion in Engineering and Applied Science Theses & Dissertations by an authorized administrator of Washington University Open Scholarship. For more information, please contact [digital@wumail.wustl.edu](mailto:digital@wumail.wustl.edu).

WASHINGTON UNIVERSITY IN ST. LOUIS

Graduate School of Arts and Sciences  
Institute of Material Science & Engineering

Dissertation Examination Committee:

Bryce F. Sadtler, Chair

Richard A. Loomis

Rohan Mishra

Shankar Sastry

Srikanth Singamaneni

Defect Chemistry and Ion Intercalation During the Growth and Solid-State Transformation of  
Metal Halide Nanocrystals

by

Bo Yin

A dissertation presented to  
The Graduate School  
of Washington University in  
partial fulfillment of the  
requirements for the degree  
of Doctor of Philosophy

May 2019  
St. Louis, Missouri

© 2019, Bo Yin

# Table of Contents

List of Figures .....	v
List of Tables .....	viii
List of Abbreviations and Illustrations .....	ix
Acknowledgements .....	x
Abstract of the Dissertation .....	xiii
<b>Chapter 1: Introduction: Applications of Semiconductor Metal Halides and Factors Affecting Their Performance .....</b>	<b>1</b>
1.1 Semiconductor Metal Halides – Their Properties and Applications .....	2
1.2 The Effects of Morphology and Size of Semiconductor Metal Halides .....	3
1.3 Colloidal Synthesis of Metal Halide Nanocrystals .....	5
1.4 Increasing the Complexity of Metal Halide Nanocrystals .....	6
1.5 Role of Defects in the Morphology of Nanocrystals .....	8
1.6 Contributions and Outline of the Dissertation .....	9
1.7 References .....	11
<b>Chapter 2: Compositionally Induced Twin Defects Control the Shape of Ternary Silver Halide Nanocrystals .....</b>	<b>20</b>
2.1 Introduction .....	21
2.2 Experimental Details .....	23
2.2.1 Materials and $\text{AgBr}_{1-x}\text{I}_x$ Nanocrystal Synthesis .....	23
2.2.2 Details of Characterization .....	24
2.3 Results and Discussion .....	26
2.3.1 Results .....	26
2.3.2 Structures and Binary Phase Diagram of AgBr and AgI .....	32
2.3.3 Twin Boundary and Hexagonal Prismatic Morphology .....	36
2.3.4 DFT Calculations of Ternary $\text{AgBr}_{1-x}\text{I}_x$ System .....	40
2.4 Conclusions .....	44
2.5 Acknowledgements .....	44
2.6 References .....	45

<b>Chapter 3: Conversion of Lead Iodide Microcrystals to CH<sub>3</sub>NH<sub>3</sub>PbI<sub>3</sub> with Methylammonium Iodide Both in Solution and as Plasma.....</b>	<b>54</b>
3.1 Introduction.....	55
3.2 Experimental Details.....	57
3.2.1 Materials and Chemical Synthesis.....	57
3.2.2 Details of Conversion from PbI <sub>2</sub> Microcrystals to CH <sub>3</sub> NH <sub>3</sub> PbI <sub>3</sub> .....	59
3.2.3 Details of Characterization.....	60
3.3 Results and Discussion.....	62
3.3.1 Synthesis of PbI <sub>2</sub> Microcrystals and Their Conversion to CH <sub>3</sub> NH <sub>3</sub> PbI <sub>3</sub> .....	62
3.3.2 In situ Observation of the Conversion from Single PbI <sub>2</sub> Microcrystals to CH <sub>3</sub> NH <sub>3</sub> PbI <sub>3</sub> with Fluorescence Microscopy.....	66
3.3.3 Synthesis of PbI <sub>2</sub> Nanocrystals and Conversion to CH <sub>3</sub> NH <sub>3</sub> PbI <sub>3</sub> .....	70
3.4 Conclusions.....	72
3.5 Acknowledgements.....	73
3.6 References.....	74
<b>Chapter 4: Fluorescence Microscopy of Single Lead Bromide Nanocrystals Reveals Sharp Transitions during Their Transformation to Methylammonium Lead Bromide.....</b>	<b>83</b>
4.1 Introduction.....	84
4.2 Experimental Details.....	85
4.2.1 Materials and Chemical Synthesis.....	85
4.2.2 Details of Characterization.....	88
4.2.3 Flow Cell Preparation.....	90
4.2.4 Monitoring Single Nanocrystal Conversion with Fluorescence Microscopy.....	91
4.2.5 Data Analysis.....	92
4.2.6 Monte Carlo Simulations.....	94
4.3 Results and Discussion.....	96
4.3.1 Synthesis of PbBr <sub>2</sub> Nanocrystals and Their Conversion to CH <sub>3</sub> NH <sub>3</sub> PbBr <sub>3</sub> .....	96
4.3.2 Single-Particle Fluorescence Trajectories.....	101
4.3.3 Statistical Analysis of Single-Particle Fluorescence Trajectory.....	104
4.3.4 Phase Transformation Model for Conversion via Monte Carlo Simulations.....	109
4.3.5 Comparison of Ion Intercalation and Cation Exchange.....	113
4.4 Conclusions.....	115
4.5 Acknowledgements.....	116
4.6 References.....	117

<b>Chapter 5: Conclusions and Future Studies.....</b>	<b>123</b>
5.1 Conclusions.....	124
5.2 Preliminary Results of Anion Exchange from Cl- to Br- in Cesium Lead Halide Nanocrystals.....	125
5.3 Future Studies .....	127
5.3.1 Study the Photocatalytic Activity of Different Crystal Facets with AgBr <sub>1-x</sub> I <sub>x</sub> Nanocrystals.....	127
5.3.2 Study of Single Nanocrystal PL Change with Fluorescence Microscopy .....	129
5.4 References.....	132
<b>Appendix : Matlab Scripts for Data Analysis .....</b>	<b>136</b>

# List of Figures

## **Chapter 1. Introduction: Applications of Semiconductor Metal Halides and Factors Affecting Their Performance**

- Figure 1.1: Morphology Alternation Determines Exposed Facets of Crystals.....4
- Figure 1.2: Schematic of a Screw Dislocation .....9

## **Chapter 2. Compositional Induced Twin Defects Control the Shape of Ternary Silver Halide Nanocrystals**

- Figure 2.1: SEM Images of  $\text{AgBr}_{1-x}\text{I}_x$  Nanocrystals with Different Ratios of Br<sup>-</sup> to I<sup>-</sup>.....27
- Figure 2.2: Size Distribution Histograms of the  $\text{AgBr}_{1-x}\text{I}_x$  Nanocrystals.....28
- Figure 2.3: XRD Patterns of  $\text{AgBr}_{1-x}\text{I}_x$  Nanocrystals with Different Ratios of Br<sup>-</sup> to I<sup>-</sup>.....29
- Figure 2.4: TEM Images and Electron Diffraction Patterns of Single  $\text{AgBr}_{1-x}\text{I}_x$  nanocrystals.....31
- Figure 2.5: AgBr – AgI Phase Diagram.....33
- Figure 2.6: SEM Images of  $\text{AgBr}_{1-x}\text{I}_x$  Nanocrystals with Higher Iodide Contents.....34
- Figure 2.7: XRD Patterns Showing Phase Segregation in  $\text{AgBr}_{1-x}\text{I}_x$  Nanocrystals.....35
- Figure 2.8: Models of Silver Halide Crystal Nuclei Possessing Varying Number of Twin Boundaries.....37
- Figure 2.9: Histogram of the Ratio of Short Edge Length to Long Edge Length for Hexagonal Platelet  $\text{AgBr}_{1-x}\text{I}_x$  Nanocrystals Synthesized with a Br:I Ratio of 11:5.....39
- Figure 2.10: DFT Calculation of Slab Model with a Single Iodide Substitutional Defect.....42

## **Chapter 3. Conversion of Lead Iodide Microcrystals to Methylammonium Lead Iodide Perovskite with Methylammonium Iodide Both in Solution and as Plasma**

- Figure 3.1: SEM Images of  $\text{PbI}_2$  Microcrystals Before and After Reaction with MAI in Solution.....63

Figure 3.2:	XRD Patterns of PbI <sub>2</sub> Microcrystals Before and After Reaction with MAI in Solution.....	64
Figure 3.3:	Schematic Showing the Electrospray Configuration Used to Transform PbI <sub>2</sub> Microcrystals to CH <sub>3</sub> NH <sub>3</sub> PbI <sub>3</sub> .....	65
Figure 3.4:	SEM Images of PbI <sub>2</sub> Microcrystals After MAI Plasma Electrospray.....	66
Figure 3.5:	Schematic Showing the Experimental Configuration Used to Observe the Transformation of Single PbI <sub>2</sub> Microcrystals to CH <sub>3</sub> NH <sub>3</sub> PbI <sub>3</sub> .....	67
Figure 3.6:	Imaging the Conversion of PbI <sub>2</sub> Microcrystals into CH <sub>3</sub> NH <sub>3</sub> PbI <sub>3</sub> via Fluorescence Microscopy.....	68
Figure 3.7:	TEM Images of Single PbI <sub>2</sub> Nanocrystal and Its Diffraction Pattern.....	71
Figure 3.8:	TEM Images of PbI <sub>2</sub> Nanocrystals After Reaction with MAI Solution.....	72

#### **Chapter 4. Fluorescence Microscopy of Single Lead Bromide Nanocrystals Reveals Sharp Transitions during Their Transformation to Methylammonium Lead Bromide**

Figure 4.1:	TEM Images of PbBr <sub>2</sub> Nanocrystals Before and After Reaction with CH <sub>3</sub> NH <sub>3</sub> Br.....	96
Figure 4.2:	Histograms Showing the Size Distribution of PbBr <sub>2</sub> Nanocrystals Before and After the Transformation.....	97
Figure 4.3:	XRD Pattern of the As-synthesized Nanocrystals.....	97
Figure 4.4:	XPS of the As-synthesized PbBr <sub>2</sub> nanocrystals.....	98
Figure 4.5:	Optical Spectra Showing the Conversion of PbBr <sub>2</sub> Nanocrystals to CH <sub>3</sub> NH <sub>3</sub> PbBr <sub>3</sub> .....	99
Figure 4.6:	Experimental Configuration Used to Observe the Transformation of Single PbBr <sub>2</sub> Nanocrystals to CH <sub>3</sub> NH <sub>3</sub> PbBr <sub>3</sub> .....	101
Figure 4.7:	Fluorescence Microscopy Imaging the Transformation of Single PbBr <sub>2</sub> Nanocrystals to CH <sub>3</sub> NH <sub>3</sub> PbBr <sub>3</sub> .....	102
Figure 4.8:	Integrated Fluorescence Intensity Versus Time Over the Entire Field-of-view with Different Concentrations of CH <sub>3</sub> NH <sub>3</sub> Br .....	104
Figure 4.9:	Waiting Times for Different Nanocrystals within the Same Field-of-view Plotted vs. Their Location.....	104



Figure 4.10:	Histograms of the Relative Waiting Times for PbBr <sub>2</sub> Nanocrystals to Transform into CH <sub>3</sub> NH <sub>3</sub> PbBr <sub>3</sub> with Different Concentrations of CH <sub>3</sub> NH <sub>3</sub> Br.....	105
Figure 4.11:	Fittings of Distributions of Waiting Times at Different Concentrations of CH <sub>3</sub> NH <sub>3</sub> Br to Gaussian Distributions.....	106
Figure 4.12:	Switching Time Fitting of Intensity Trajectory for Single Nanocrystal and Its Dependence on CH <sub>3</sub> NH <sub>3</sub> Br Concentration.....	107
Figure 4.13:	Monte Carlo Simulations of Ion Intercalation in PbBr <sub>2</sub> Nanocrystals: Diffusion-limited Model and Phase Transformation Model.....	109
Figure 4.14:	Histograms of Waiting Times for Various Initial Equilibrium Constants That Correspond to Varied Ion Concentrations.....	111
Figure 4.15:	Ensemble and Individual Intercalation Trajectories for Three Additional Models: Sudden Nucleation, Continuous Nucleation and Positive Cooperativity.....	112

## Chapter 5. Conclusions and Future Studies

Figure 5.1:	Comparison of Average Switching Time of Anion Exchange from CsPbCl <sub>3</sub> to CsPbBr <sub>3</sub> Nanocrystals and Conversion from PbBr <sub>2</sub> to CH <sub>3</sub> NH <sub>3</sub> PbBr <sub>3</sub> Nanocrystals.....	126
Figure 5.2:	Schematic of Experimental Set-up to Test Photocatalytic CO <sub>2</sub> Reduction of Ternary AgBr <sub>1-x</sub> I <sub>x</sub> Nanocrystals.....	128

# List of Tables

## **Chapter 2. Compositional Induced Twin Defects Control the Shape of Ternary Silver Halide Nanocrystals**

Table 2.1: Reaction Conditions Used to Synthesize  $\text{AgBr}_{1-x}\text{I}_x$  Nanocrystals Described in Chapter 2 and Their Composition as Measured by EDS.....26

# List of Abbreviations and Illustrations

SEM	scanning electron microscope
TEM	transmission electron microscope
XRD	X-ray diffraction
XPS	X-ray photoelectron spectroscopy
PL	photoluminescence
EDS	energy-dispersive X-ray spectroscopy
FCC	face-center-cubic crystal structure
HCP	hexagonal close-packed crystal structure
DFT	density functional theory
UV-Vis	ultraviolet-visible spectroscopy
ALD	atomic layer deposition
MAI	methylammonium iodide
IPA	2-propanol or iso-propanol
PVP	polyvinylpyrrolidone
ITO	indium-doped tin oxide

**conduction band:** in solid-state physics, the lowest range of vacant electronic states at 0 K.

**valence band:** in solid-state physics, the highest range of electron energies where electrons are present at 0 K.

**band gap:** the energy difference between the conduction band and the valence band.

**quantum confinement:** Once the dimensions of a material is of the same magnitude as the de Broglie wavelength of the electron wave function, the electronic and optical properties deviate substantially from those of bulk materials.

# Acknowledgments

I want to thank a lot of people for their help, patience and constant encouragement during my Ph.D research and study.

First of all, I would like to thank my advisor, Prof. Bryce F. Sadtler. Before come to Washington University I have never worked in a chemistry lab before. Prof. Sadtler was very patient and informative and he taught me everything I need to know to work in a chemistry lab. During the course of my research there were a lot of obstacles and I could always count on him to give suggestions. I am grateful for all the valuable time Prof. Sadtler invested in me. I am a better researcher, presenter and writer now by working with him. I learned the most from Prof. Sadtler as a researcher and scientist. I really enjoy the last 5 years working in his group and I want to thank him for giving me this opportunity.

Next I want to thank members of my Dissertation Advisory Committee, Prof. Richard Loomis, Prof. Rohan Mishra, Prof. Srikanth Singamaneni, Prof. Shankar Sastry and Dr. Cynthia Lo. Thank all of them for sharing time with me to discuss my projects and guide me through the course of my Ph.D study. Prof. Rohan Mishra has been especially helpful with the DFT calculations and Monte Carlo simulations in my work.

I also thank Prof. Willam Buhro's group. Summer 2014 when I first came to join Prof. Sadtler's group, our lab was still under renovation. Thanks to Prof. Buhro for letting me use their lab and equipment, so I could start my research in an early time. Dr. Fudong Wang, Dr. Linjia Mu and Dr. Yang Zhou also helped me greatly in equipment and characterization techniques.

I thank all of the staff of the Institute of Material Science and Engineering (IMSE), including Director Prof. Katharine Flores, assistant Beth Gartin and lab manager Dr. Huafnag Li and Dr.

Tyrone Daulton. Prof. Flores recruited me more than 5 years ago into the Ph.D program and I thank her for this amazing opportunity. For all the staff in IMSE, your efforts and hard work on running the department have made my life much easier.

I also want to give many thanks to our group members. Dong Wang gave a lot of good suggestions on how to make the experiment more efficient. Meikun Shen assisted me with the fluorescence microscope operations. Daniel Khan was an undergraduate in our lab who helped me with the data analysis of trajectories. I am thankful to Craig Laing who was my undergraduate mentee for two years. Other members, Dr. Wenlei Zhu, Chu Qin, Che Tan and Dongyan Zhang, thank you guys for all the daily conversations. The life in the lab would be much less interesting without your guys.

Next I would like to thank Washington University in St. Louis and National Science Foundation for the financial support for my research projects.

Last but not the least, I want to thank my family for their love and support through all the frustration and happiness. My parents, Yuling Wang and Zhian Yin, have done more than what a son can ask for to support me to follow my dream. None of these amazing experiences would happen without their unreserved support and encouragement. I am eternally grateful.

Bo Yin

*Washington University in St. Louis*

*Louderman Hall*

*May 2019*

Dedicated to my dear grandma and grandpa.

# **Abstract of the Dissertation**

Defect Chemistry and Ion Intercalation During the Growth and Solid-state Transformation of  
Metal Halide Nanocrystals

by

Bo Yin

Doctor of Philosophy

Material Science

Washington University in St. Louis, 2019

Professor Bryce F. Sadtler, Chair

Semiconductor metal halides as light-sensitive materials have applications in multiple areas, such as photographic film, antibacterial agents and photocatalysts. One focus of this dissertation is to achieve novel morphologies of ternary silver bromoiodide ( $\text{AgBr}_{1-x}\text{I}_x$ ,  $0 < x < 1$ ) nanocrystals by intentionally introducing defects into the system. Organic-inorganic hybrid perovskite (methylammonium lead halide,  $\text{CH}_3\text{NH}_3\text{PbX}_3$ ,  $X = \text{Cl}, \text{Br}$  or  $\text{I}$ ) is another example of semiconductor metal halide that recently has been focused a lot of research attention due to its outstanding performance in solar cells and light-emitting diodes. One of the common methods to synthesize  $\text{CH}_3\text{NH}_3\text{PbX}_3$  perovskite is the solid-state intercalation of methylammonium halide ions into lead halide compounds. Another goal of this work is to study the reaction kinetic of this solid-state transformation in single lead bromide ( $\text{PbBr}_2$ ) nanocrystals via fluorescence microscopy.

For the silver halide system, we demonstrate that the anion composition of  $\text{AgBr}_{1-x}\text{I}_x$  nanocrystals determines their shape through the introduction of twin defects as the nanocrystals are made more iodide-rich.  $\text{AgBr}_{1-x}\text{I}_x$  nanocrystals grow as single-phase, solid solutions with the

rock salt crystal structure for anions compositions ranging from  $0 \leq x < 0.38$ . With increasing iodide content the morphology of the nanocrystals evolves from cubic to truncated cubic to hexagonal prismatic. Structural characterization indicates the cubic nanocrystals are bound by  $\{100\}$  facets whereas the hexagonal platelet nanocrystals possess  $\{111\}$  facets as their top and bottom surface. Calculations based on first-principles density functional theory show that iodide substitution in AgBr stabilizes  $\{111\}$  surfaces and that twin defects parallel to these surfaces possess a low formation energy. Our experimental observations and calculations are consistent with a growth model in which the presence of multiple twin defects parallel to a  $\{111\}$  surface enhances lateral growth of the side facets and changes the nanocrystal shape.

To study the reaction kinetic of solid-state conversion, we use the change in fluorescence brightness to image the transformation of individual lead bromide ( $\text{PbBr}_2$ ) nanocrystals to methylammonium lead bromide ( $\text{CH}_3\text{NH}_3\text{PbBr}_3$ ) via intercalation of  $\text{CH}_3\text{NH}_3\text{Br}$ . Analyzing this reaction one nanocrystal at a time reveals information that is masked when the fluorescence intensity is averaged over many particles. Sharp rises in the intensity of single nanocrystals indicate they transform much faster than the time it takes for the ensemble average to transform. Furthermore, the intensity rises for individual nanocrystals are insensitive to the  $\text{CH}_3\text{NH}_3\text{Br}$  concentration. To explain these observations, we propose a phase transformation model in which the reconstructive transitions necessary to convert a  $\text{PbBr}_2$  nanocrystal into  $\text{CH}_3\text{NH}_3\text{PbBr}_3$  initially create a high energy barrier for ion intercalation. A critical point in the transformation occurs when the crystal adopts the perovskite phase, at which point the activation energy for further ion intercalation becomes progressively smaller. Monte Carlo simulations that incorporate this change in activation barrier into the likelihood of reaction events reproduce key experimental observations for the intensity trajectories of individual particles. The insights



gained from this study may be used to further control the crystallization of  $\text{CH}_3\text{NH}_3\text{PbBr}_3$  and other solution-processed semiconductors.

In this dissertation, we are focusing on two different systems, silver halide and lead halide perovskite. Even though the systems are different, we find that solid-state immiscibility between different halide compounds plays an important role in both reactions we are studying. In  $\text{AgBr}_{1-x}\text{I}_x$ , the structural immiscibility between rock salt AgBr and wurtzite AgI causes the formation of twin boundaries, which change the nanocrystal morphology. For the lead halide system, the sharp transition in fluorescence intensity observed in single nanocrystals is also due to structural immiscibility which causes the sudden phase transition from  $\text{PbBr}_2$  to the perovskite phase. This structural immiscibility between different halide compounds plays a critical role for both metal halide systems.

# **Chapter 1**

## **Introduction: Applications of Semiconductor Metal Halides and Factors Affecting Their Performance**

## 1.1 Semiconductor Metal Halides – Their Properties and Applications

We were starting to study and apply metal halide crystal in our everyday life at a surprisingly early time. Silver halide crystals (AgCl, AgBr and AgI) were introduced and used as light-sensitive chemicals in photographic process, called daguerreotype, in 1839.<sup>1</sup> Until nowadays silver halide crystals are still being used in photographic films even though the resolution of the film improves dramatically. Besides being used in photographic films, silver halide is also found to be a good antibacterial agent<sup>2-5</sup> and photocatalyst<sup>6-17</sup>. These features of silver halide are all related to the semiconductor nature of the material, which means silver halide can absorb visible light and utilize the photon energy. By absorption of sunlight, the overall energy of the silver halide increases. With the elevated energy there are a lot of things silver halide crystals can do. They can be used to oxidize organic pollutants in the water.<sup>6-13</sup> Also it has been reported that silver halide crystals can reduce CO<sub>2</sub> into methanol and/or ethanol which can be used as fuel.<sup>13-17</sup> In modern society with increasing human activity, the environmental problems like water pollution and greenhouse effect caused by excess CO<sub>2</sub> emission become more and more urgent. Silver halide material may have more applications in the future.

Organometal halide perovskite (e.g. CH<sub>3</sub>NH<sub>3</sub>PbX<sub>3</sub>, X = Cl, Br or I) is another promising group of semiconductor metal halide which has focused a lot of research attention in recent years. Victor Goldschmidt described the notable crystal structure of perovskite in 1926.<sup>18</sup> However applications of organometal halide perovskite in solar cells,<sup>19-24</sup> light emitting diodes (LED) and other optoelectronic devices are fairly recent.<sup>22-29</sup> Based on the report of National Renewable Energy Laboratory, the first certified record of perovskite based solar cell was in 2012 which is about 13%.<sup>30</sup> As to 2018 the efficiency of perovskite based solar cell has

increased to 23.3%, which is comparable to crystalline silicon based solar cell that has been developed in 1970s.<sup>30</sup> Halide perovskite are also used in LED applications because of their direct band gap, high mobility and long exciton lifetime. The prominent rate of increase in efficiency, relatively easy synthesis method, and their low cost make the metal halide perovskite one of the most competitive candidates to replace silicon in optoelectronic devices. However, metal halide perovskite is not famous for its stability under ambient moisture condition, which needs a lot of improvement in the future.

## 1.2 The Effects of Morphology and Size of Semiconductor Metal Halides

For the applications of semiconductor metal halide in photocatalysis or as light-sensitive chemicals in that matter, it is really important to control the morphology and size of the semiconductor metal halide material. For example, large platelet microcrystals of AgBr are a desirable morphology for photography as they provide a high surface area for photochemical reactions to take place and can easily be processed into photographic films. Since all the catalytic reactions occurs on the surface of photocatalysts, the morphologies greatly affect the performance of semiconductor metal halides as photocatalysts.<sup>31-37</sup> Also if the metal halide is single crystalline in nature, the morphology defines what crystal facets are exposed. As shown in **Figure 1.1**, under the assumption of face-center-cubic (FCC) crystal structure of the demonstrated material, the exposed crystal facets, edges and corners alter by changing the morphology of the particles from cube to truncated cube to octahedron (**a to d** in **Figure 1.1**). It has been well known that different crystal facets interact differently with reactant molecules leading to different catalytic activities.<sup>31-37</sup>

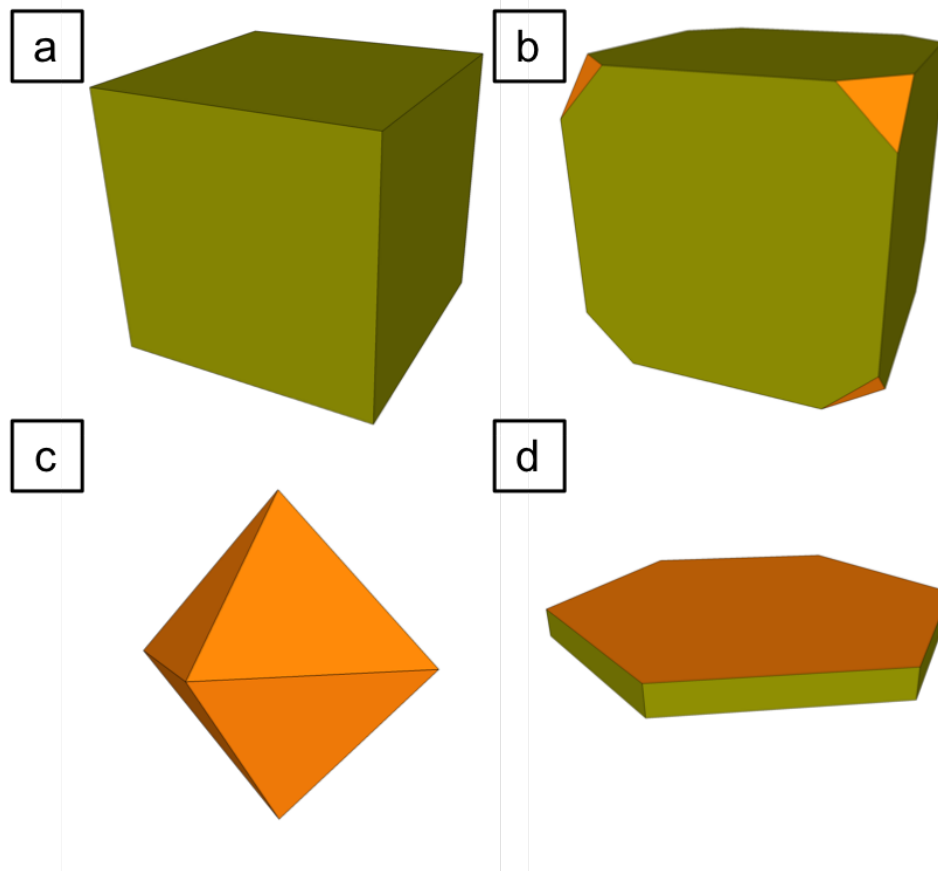


**Figure 1.1** Morphology alteration and the presence of extended defects determines exposed facets, edges and corners in a face-center-cubic (FCC) crystal. (a) perfect cube; (b) truncated cube; (c) octahedron; (d) hexagonal prism. Green color represents (100) facets and (111) facets are shown in orange color.

The size of the semiconductor metal halides is another important factor for their applications. The surface-to-volume ratio increases as the particle size decreases. As mentioned above, all heterogeneous catalytic reactions occur on a surface. Therefore, generally speaking more surface area means more reactive sites for photocatalysis and the rate of photocatalysis would increase accordingly even though some surface facets may have more reactive sites than others as mentioned before. The effect of size of metal halides is even more prominent for the applications in LED since the emitting wavelength of light could be affected by the size of metal

halides. The size of the semiconductor particles is reduced to a scale where the electrons of the semiconductor can “sense” the boundaries of the particle during their motions. (E.g. the size of the particles is the same magnitude to the Bohr radius of the electron in the material.) Then quantum confinement effects start to dominate the absorption and emission properties of the particle. In the region of quantum confinement, the difference in energy between filled electron states and empty states increases with decreasing size of the particle. (This difference in energy is called band gap in a semiconductor.) Therefore, the absorption and emission spectrum would gradually shift to higher energy with increasing band gap of semiconductor particle.<sup>24,29,38-41</sup> Of course, this phenomenon is not specific to semiconductor metal halides. However, it is still a useful tool since we can tune the absorption and emission wavelength of semiconductor metal halide through controlling the size of the crystal.

### **1.3 Colloidal Synthesis of Metal Halide Nanocrystals**

One of the most common methods to synthesize metal halide nanocrystals is colloidal synthesis.<sup>22,24,7,42-45</sup> Colloidal synthesis can produce high quality, uniform and well dispersed metal halide nanocrystals with good repeatability and its synthesis procedures are relatively easy to follow. In general, colloidal synthesis involves controlling the precipitation/nucleation and subsequent growth of nanocrystals in solution by varying the temperature, concentration of precursor, pressure and various surfactants. In order to narrow the size distribution of synthesized particles there are two key aspects, temporal separation of nucleation and growth and diffusion-limited growth.<sup>46,47</sup> Surfactants can be used in these cases to control certain facets in diffusion-limited growth regime. Such surfactants include polyvinylpyrrolidone (PVP),<sup>7,42-43</sup> tri-*n*-octylphosphine oxide (TOPO)<sup>44,45</sup> and tetrabutylammonium bromide (TBAB)<sup>24</sup>. It has been

argued that different surfactants preferentially adsorb to different crystal facets of nanocrystals and therefore alter the morphology of nanocrystal by changing the growth rate of crystal facets.<sup>44,45</sup> Crystal facets with faster growth rates are replaced by ones with slower growth rate during crystal growth.<sup>45</sup> Strong adsorption of a surfactant will slow down the growth of a facet such that it becomes dominant in the final morphology of the particle. Polarity difference of solvents can also be used in colloidal synthesis of metal halide nanocrystals.<sup>8,16</sup> For example, Chen et al. synthesized silver halide photocatalysts in an oil-in-water system.<sup>16</sup>

## 1.4 Increasing the Complexity of Metal Halide Nanocrystals

As semiconductor metal halides have wide range of applications, there is a need to fine tune the properties of metal halide in different scenarios. Therefore, more complex metal halide nanocrystals are desirable.

One way to achieve that complexity is to make metal halides that contain two or more cations or anions, such as a ternary halide solid solution. The halide ions ( $\text{Cl}^-$ ,  $\text{Br}^-$  or  $\text{I}^-$ ) have similar properties and sizes. Therefore, they are interchangeable in a lot of cases.<sup>22,48,43,16</sup> It has been reported that in ternary silver chlorobromide ( $\text{AgCl}_x\text{Br}_{1-x}$ ) nanocrystal system  $\text{Cl}^-$  and  $\text{Br}^-$  ions are completely interchangeable, and properties in-between that of  $\text{AgCl}$  and  $\text{AgBr}$  are achievable.<sup>16,43</sup> For example, the lattice constant of ternary  $\text{AgCl}_x\text{Br}_{1-x}$  is between lattice constant of  $\text{AgBr}$  and  $\text{AgCl}$ . The band gap of ternary halide solution is also between  $\text{AgBr}$  and  $\text{AgCl}$ , which makes their light absorption start somewhere in between. Through complex metal halide crystals, such as ternary halide solid solution, photocatalysts with better performance can be achieved.<sup>16</sup> Through partially replacing some of the halide ions with a different kind, it offers

an extra handle for us to tailor the properties of semiconductor metal halide to better suit the applications.

Another way to acquire complexity is to make metal halides with more complex structures. Decorating metal halides with other semiconductors, noble metals or graphene can broaden the overall absorption or facilitate exciton separation and transportation.<sup>4,6-8,10,12-13,17</sup> There have been a lot of reports that couple metal halides with other semiconductors such as titanium dioxide (TiO<sub>2</sub>).<sup>2,5,3,14,9</sup> Decorated with other semiconductors, it broadens the range of light absorption for metal halide photocatalysts. If the properties of decorated semiconductor are complementary to metal halide, it would increase their performance as photocatalysts.<sup>2,3,5,9,14</sup> Noble metals when connected with metal halides can serve as charge separation centers to facilitate electron and hole separation and reduce recombination. In addition, noble metals with nanometer size such as gold and silver would have surface plasmon effect which would also increase the light absorption in the metal halides.<sup>6-8,10-12</sup>

Last but not the least, solid-state transformation can also alter the composition and achieve more complex metal halide nanocrystals. Different from directly synthesizing metal halides nanocrystals with complex composition, solid-state transformation is a post-synthesis reaction. It has the advantage of facilitating the preparation of materials that are difficult to make by direct colloidal synthesis. Furthermore, typically after solid-state transformation the morphology of the parental material is preserved. Therefore by controlling the shape of parental crystal, the morphology of the product of solid-state transformation can be determined.<sup>49-54</sup> One well-known example of solid-state transformation reaction would be cation-exchange reaction between CdSe and Ag<sup>+</sup> cation where Cd<sup>2+</sup> in CdSe would be replaced by Ag<sup>+</sup> cation to form Ag<sub>2</sub>Se nanocrystals.<sup>49-50</sup> Furthermore, recently the anion-exchange reactions between CsPbCl<sub>3</sub>,



CsPbBr<sub>3</sub> and CsPbI<sub>3</sub> have been on the research spotlight. By anion exchange Cl<sup>-</sup> with Br<sup>-</sup> and I<sup>-</sup>, the continuous shift of photoluminescence wavelength of cesium lead perovskite is achieved.<sup>22,48</sup> With solid-state transformation we can alter the composition of metal halide nanocrystals and achieve morphologies otherwise hard to get using other synthesis method.

## 1.5 Role of Defects in the Morphology of Nanocrystals

Defects by their nature are places where the irregular arrangement of atoms in crystal. They possess higher formation energy compared to a perfect crystal. Therefore, defects tend to promote anisotropic growth of crystal along the directions they extend. We can make nanocrystals with morphologies of anisotropic dimensions by intentionally introducing and utilizing defects during the nucleation and growth of nanocrystals. Recently researchers have demonstrated that using defects, such as screw dislocations and twin boundaries, one-dimensional growth of PbS and ZnO nanostructures can be achieved.<sup>56-61</sup> The influence of dislocations in crystal growth was first reported in 1949 by Frank.<sup>55</sup> Shown in **Figure 1.2** is a schematic representation of a screw dislocation. For the following growth of the crystal, the incoming atoms prefer to grow on the vertical step that the screw dislocation created because it creates less surface area to grow on the step than to nucleate somewhere else. With further growth of the crystal, the screw dislocation grows with it and never goes away. Therefore, crystal growth rate along the direction of screw dislocations is higher. Anisotropic growth along the screw dislocations can achieve new morphologies of the crystal. There are a lot of efforts trying to reduce the amount of defects in material. They are indeed not desirable in many applications. However, defects can be used as an effective tool to modify the morphology of crystals.

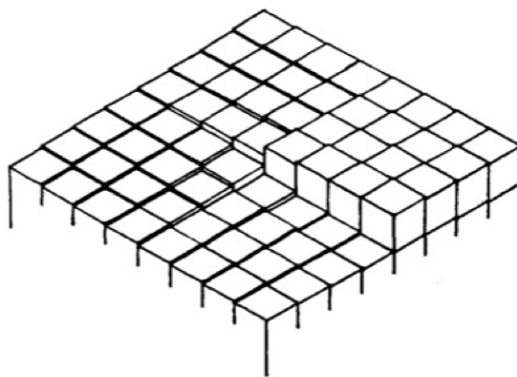


**Figure 1.2** schematic of a screw dislocation.<sup>55</sup> Adapted from (Frank, F. C., The influence of dislocations on crystal growth, *Discuss. Faraday Soc.* **1949**, 5, 48-54.) with permission from the Royal Society of Chemistry.

During the solid-state transformation, defects also play an important role. Since defects come with higher energy, it would take less formation energy for the new phase to nucleate at the locations of defect. There are several reports that solid-state transformations start at defects such as grain boundaries and edges of crystal.<sup>48,62,63</sup> If there are multiple nucleation sites of the new phase during the transformation, the product would be polycrystalline after the solid-state transformation.

## 1.6 Contributions and Outline of the Dissertation

In this dissertation, ternary silver bromoiodide nanocrystals were successfully synthesized which is compositionally more complex than binary silver halide. We intentionally induced twin defects into this ternary silver bromoiodide system to alter the morphology of nanocrystals to hexagonal prism which give us the control of the morphology of the nanocrystals. This dissertation also gives insights to the reaction mechanism and kinetics of the solid-state

transformation from lead bromide nanocrystals to  $\text{CH}_3\text{NH}_3\text{PbBr}_3$ , which is one of the most used methods to synthesize halide perovskite materials.

In this dissertation, we are focusing on two metal halide systems, ternary silver halide and methylammonium lead halide. **Chapter 2** studies the use of defect chemistry to alter the morphology of ternary silver halide nanocrystals. Study of solid-state transformation from lead iodide microcrystals to methylammonium lead iodide is given in **Chapter 3**. **Chapter 4** is focusing on in situ observing the transformation of single lead bromide nanocrystals to  $\text{CH}_3\text{NH}_3\text{PbBr}_3$  via fluorescence microscopy.

## 1.7 References

1. Hannavy, J., *Encyclopedia of Nineteenth-Century Photography*, Routledge; **2013**.
2. Elahifard, M. R.; Rahimnejad, S.; Haghghi, S.; Gholami, M. R., Apatite-coated Ag/AgBr/TiO<sub>2</sub> visible-light photocatalyst for destruction of bacteria, *J. Am. Chem. Soc.* **2007**, 129(31), 9552-9553.
3. Hou, Y.; Li, X.; Zhao, Q.; Chen, G.; Raston, C. L., Role of hydroxyl radicals and mechanism of escherichia coli inactivation on Ag/AgBr/TiO<sub>2</sub> nanotube array electrode under visible light irradiation, *Environ. Sci. Technol.* **2012**, 46(7), 4042-4050.
4. Shi, H.; Li, G.; Sun, H.; An, T.; Zhao, H.; Wong, P. K., Visible-light-driven photocatalytic inactivation of E. coli by Ag/AgX-CNTs (X = Cl, Br, I) plasmonic photocatalysts: Bacterial performance and deactivation mechanism, *Appl. Catal. B Environ.* **2014**, 158(159), 301-307.
5. Hu, C.; Lan, Y.; Qu, J.; Hu, X.; Wang, A., Ag/AgBr/TiO<sub>2</sub> visible light photocatalyst for destruction of azodyes and bacteria. *J. Phys. Chem. B.* **2006**, 110(9), 4066-4072.
6. Choi, M.; Shin, K. H.; Jang, J., Plasmonic photocatalytic system using silver chloride/silver nanostructures under visible light, *J. Colloid Interface Sci.* **2010**, 341(1), 83-87.
7. An, C.; Peng, S.; Sun, Y., Facile synthesis of sunlight-driven AgCl: Ag plasmonic nanophotocatalyst, *Adv. Mater.* **2010**, 22(23), 2570-2574.

8. Zhu, M.; Chen, P.; Liu, M., Ag/AgBr/Graphene oxide nanocomposite synthesized via oil/water and water/oil microemulsions: A comparison of sunlight energized plasmonic photocatalytic activity, *Langmuir* **2012**, 28(7), 3385-3390.
9. Ye, L.; Liu, J.; Gong, C.; Tian, L.; Peng, T.; Zan, L., Two different roles of metallic Ag on Ag/AgX/BiOX (X = Cl, Br) visible light photocatalysts: Surface plasmon resonance and Z-Scheme bridge, *ACS Catal.* **2012**, 2(8), 1677-1683.
10. Hu, C.; Peng T.; Hu X.; Nie, Y.; Zhou, X.; Qu, J.; He, H., Plasmon-Induced Photodegradation of Toxic Pollutants with Ag–AgI/Al<sub>2</sub>O<sub>3</sub> under Visible-Light Irradiation, *J. Am. Chem. Soc.* **2010**, 132(2), 857-862.
11. Wang, Y.; Sun, L.; Fugetsu, B., Morphology-controlled synthesis of sunlight-driven plasmonic photocatalysts Ag@AgX (X = Cl, Br) with graphene oxide template, *J. Mater. Chem. A* **2013**, 1, 12536-12544.
12. Dong, R.; Tian, B.; Zeng, C.; Li, T.; Wang, T.; Zhang, J., Ecofriendly synthesis and photocatalytic activity of uniform cubic Ag@AgCl plasmonic photocatalyst, *J. Phys. Chem. C* **2013**, 117(1), 213-220.
13. Cai, B.; Wang, J.; Gan, S.; Han, D.; Wu, Z.; Niu, L., A distinctive red Ag/AgCl photocatalyst with efficient photocatalytic oxidative and reductive activities, *J. Mater. Chem. A* **2014**, 2(15), 5280-5286.
14. Asi, M. A.; He, C.; Su, M.; Xia, D.; Lin, L.; Deng, H.; Xiong, Y.; Qiu, R.; Li, X., Photocatalytic reduction of CO<sub>2</sub> to hydrocarbons using AgBr/TiO<sub>2</sub> nanocomposites under visible light. *Catal. Today* **2011**, 175(1), 256-263.

15. Zhang, X.; Li, J.; Lu, X.; Tang, C.; Lu, G., Visible light induced CO<sub>2</sub> reduction and Rh B decolorization over electrostatic-assembled AgBr/palygorskite, *J. Colloid Interface Sci.* **2012**, 377, 277-283.
16. Cai, B.; Wang, J.; Han, D.; Gan, S.; Zhang, Q.; Wu, Z.; Niu, L., Ternary alloyed AgCl<sub>x</sub>Br<sub>1-x</sub> nanocrystals: Facile modulation of electronic structures toward advanced photocatalytic performance. *Nanoscale* **2013**, 5(22), 10989-10995.
17. An, C.; Wang, J.; Jiang, W.; Zhang, M.; Ming, X.; Wang, S.; Zhang, Q., Strongly visible-light responsive plasmonic shaped AgX:Ag (X = Cl, Br) nanoparticles for reduction of CO<sub>2</sub> to methanol, *Nanoscale* **2012**, 4(18), 5646-5650.
18. Golschmidt, V. M., Die Gesetze der Krystallochemie, *Die Naturwissenschaften* **1926**, 21(21), 477-485.
19. Bryant, D.; Aristidou, N.; Pont, S.; Sanchez-Molina, I.; Chotchunangatchaval, T.; Wheeler, S.; Durrant, J. R.; Haque, S. A., Light and oxygen induced degradation limits the operational stability of methylammonium lead triiodide perovskite solar cells, *Energy Environ. Sci.* **2016**, 9(5), 1655-1660.
20. Zuo, L.; Dong, S.; De Marco, N.; Hsieh, Y. T.; Bae, S. H.; Sun, P.; Yang, Y., Morphology evolution of high efficiency perovskite solar cells via vapor induced intermediate phases, *J. Am. Chem. Soc.* **2016**, 138(48), 15710-15716.
21. Chen, Q.; Zhou, H.; Hong, Z.; Luo, S.; Duan, H. S.; Wang, H.; Liu, Y.; Li, G.; Yang, Y., Planar heterojunction perovskite solar cells via vapor-assisted solution process, *J. Am. Chem. Soc.* **2014**, 136(2), 622-625.

22. Protesescu, L.; Yakunin, S.; Bodnarchuk, I. M.; Krieg, F.; Caputo, R.; Hendon, H. C.; Yang, R.; Walsh, A.; Kovalenko, V. M., Nanocrystals of cesium lead halide perovskites (CsPbX<sub>3</sub>, X = Cl, Br, and I): novel optoelectronic materials showing bright emission with wide color gamut, *Nano Lett.* **2015**, 15(6), 3692-3696.
23. Lee, M. M.; Teuscher, J.; Miyasaka, T.; Murakami, Y. N.; Snaith, H. J., Efficient hybrid solar cells based on meso-superstructured organometal halide perovskites, *Science* **2012**, 338, 643-647.
24. Hassan, Y.; Song, Y.; Pensack, R. D.; Abdelrahman, A. I.; Kobayashi, Y.; Winnik, M. A.; Scholes, G. D., Structure-tuned lead halide perovskite nanocrystals, *Adv. Mater.* **2016**, 28(3), 566-573.
25. Xing, J.; Yan, F.; Zhao, Y.; Chen, S.; Yu, H.; Zhang, Q.; Zeng, R.; Demir, H. V.; Sun, X.; Huan, A.; Xiong, Q., High-efficiency light-emitting diodes of organometal halide perovskite amorphous nanoparticles, *ACS Nano* **2016**, 10(7), 6623-6630.
26. Lee, S.; Park, J. H.; Nam, Y. S.; Lee, B.; Zhao, B.; Di Nuzzo, D.; Jung, E. D.; Jeon, H.; Kim, J. Y.; Jeong, H. Y.; Friend, R. H.; Song, M. H., Growth of nanosized single crystals for efficient perovskite light-emitting diodes, *ACS Nano* **2018**, 12(4), 3417-3423.
27. Zhao, L.; Yeh, Y.; Tran, N. L.; Wu, F.; Xiao, Z.; Kerner, R. A.; Lin, Y.; Scholes, G. D.; Yao, N.; Rand, B. P., In situ preparation of metal halide perovskite nanocrystal thin films for improved light-emitting devices, *ACS Nano* **2017**, 11(4), 3957-3964.
28. Yan, F.; Xing, J.; Xing, G.; Quan, L.; Tan, S. T.; Zhao, J.; Su, R.; Zhang, L.; Chen, S.; Zhao, Y.; Huan, A.; Sargent, E. H.; Xiong, Q.; Demir, H. V., Highly efficient visible

- colloidal lead-halide perovskite nanocrystal light-emitting diodes, *Nano Lett.* **2018**, 18(5), 3157-3164.
29. Kim, Y. H.; Wolf, C.; Kim, Y. T.; Cho, H.; Kwon, W.; Do, S.; Sadhanala, A.; Park, C. G.; Rhee, S. W.; Im, S. H.; Friend, R. H.; Lee, T. W., Highly efficient light-emitting diodes of colloidal metal-halide perovskite nanocrystals beyond quantum size, *ACS Nano* **2017**, 11(7), 6586-6593.
30. Best research-cell efficiencies, National Renewable Energy Laboratory.  
<https://www.energy.gov/eere/solar/downloads/research-cell-efficiency-records>. Published **2018**.
31. Jaramillo, T. F.; Jørgensen, K. P.; Bonde, J.; Nielsen, J. H.; Horch, S.; Chorkendorff, I., Identification of active edge sites for electrochemical H<sub>2</sub> evolution from MoS<sub>2</sub> nanocatalysts, *Science* **2007**, 317(5834), 100-102.
32. Liu, G.; Sun, C.; Yang, H.; Smith, S. C.; Wang, L.; Lu, G.; Cheng, H., Nanosized anatase TiO<sub>2</sub> single crystals for enhanced photocatalytic activity, *Chem. Commun.* **2010**, 46(5), 755-757.
33. Xie, Y. P.; Liu, G.; Yin, L.; Cheng, H. M., Crystal facet-dependent photocatalytic oxidation and reduction reactivity of monoclinic WO<sub>3</sub> for solar energy conversion, *J. Mater. Chem.* **2012**, 22(14), 6746-6751.
34. Wang, D.; Jiang, H.; Zong, X.; Xu, Q.; Ma, Y.; Li, G.; Li, C., Crystal facet dependence of water oxidation on BiVO<sub>4</sub> sheets under visible light irradiation, *Chem - A Eur J.* **2011**, 17(4), 1275-1282.



35. Martin, D. J.; Umezawa, N.; Chen, X.; Ye, J.; Tang, J., Facet engineered Ag<sub>3</sub>PO<sub>4</sub> for efficient water photooxidation, *Energy Environ. Sci.* **2013**, 6(11), 3380-3386.
36. Zhu, W.; Michalsky, R.; Metin, Ö.; Lv, H.; Guo, S.; Wright, C. J.; Sun, X.; Peterson, A. A.; Sun, S., Monodisperse Au nanoparticles for selective electrocatalytic reduction of CO<sub>2</sub> to CO, *J. Am. Chem. Soc.* **2013**, 135(45), 16833-16836.
37. Xu, H.; Wang, W.; Zhu, W., Shape evolution and size-controllable synthesis of Cu<sub>2</sub>O octahedra and their morphology-dependent photocatalytic properties, *J. Phys. Chem. B* **2006**, 110(28), 13829-13834.
38. Bruchez, M.; Moronne, M.; Gin, P.; Weiss, S.; Alivisatos, A. P., Semiconductor nanocrystals as fluorescent biological labels, *Science* **1998**, 281(5385), 2013-2016.
39. Milliron, D.; Hughes, S. M.; Cui, Y.; Manna, L.; Li, J.; Wang, L.; Alivisatos, A. P., Colloidal nanocrystal heterostructures with linear and branched topology, *Nature* **2004**, 430(6996), 190-195.
40. Huynh, W. U.; Dittmer, J. J.; Alivisatos, A. P., Hybrid nanorod-polymer solar cells, *Science* **2002**, 295(5564), 2425-2427.
41. Eisler, H.; Bawendi, M. G.; Hollingsworth, J., Optical gain and stimulated in nanocrystal emission quantum dots, *Science* **2000**, 290(5490), 314-317.
42. Peng, S.; Sun, Y., Ripening of bimodally distributed AgCl nanoparticles, *J. Mater. Chem.* **2011**, 21(31), 11644-11650.

43. Li, Z.; Okasinski, J. S.; Gosztola, D. J.; Ren, Y.; Sun, Y., Silver chlorobromide nanocubes with significantly improved uniformity: synthesis and assembly into photonic crystals, *J. Mater. Chem. C* **2015**, 3(1), 58-65.
44. Yin, Y.; Alivisatos, A. P., Colloidal nanocrystal synthesis and the organic – inorganic interface, *Nature* **2005**, 437(29), 664-670.
45. Manna, L.; Scher, E. C.; Alivisatos, A. P., August R. V., Synthesis of soluble and processable rod-, arrow-, teardrop-, and tetrapod-shaped CdSe nanocrystals, *J. Am. Chem. Soc.* **2000**, 122(27), 12700-12706.
46. Penner, R. M., Mesoscopic metal particles and wires by electrodeposition, *J. Phys. Chem. B* **2002**, 106, 3339-3353.
47. Peng, X.; Wickham, J.; Alivisatos, A. P., Kinetics of II-VI and III-V colloidal semiconductor nanocrystal growth: “ Focusing ” of size distributions, *J. Am. Chem. Soc.* **1998**, 120(98), 5343-5344.
48. Karimata, I.; Kobori, Y.; Tachikawa, T., Direct observation of charge collection at nanometer-scale iodide-rich perovskites during halide exchange reaction on  $\text{CH}_3\text{NH}_3\text{PbBr}_3$ , *J. Phys. Chem. Lett.* **2017**, 8(8), 1724-1728.
49. Routzahn, A. L.; Jain, P. K., Single-nanocrystal reaction trajectories reveal sharp cooperative transitions, *Nano. Lett.* **2014**, 14, 987-992.
50. Routzahn, A. L.; Jain, P. K., Luminescence blinking of a reacting quantum dot, *Nano. Lett.* **2015**, 15, 2504-2509.

51. Sadtler, B.; Demchenko, D. O.; Zheng, H.; Hughes, S. M.; Maxwell, G., Selective facet reactivity during cation exchange in cadmium sulfide nanorods, *J. Am. Chem. Soc.* **2009**, 131(14), 5285–5293.
52. Luther, J. M.; Zheng, H.; Sadtler, B.; Alivisatos, A. P., Synthesis of PbS nanorods and other ionic nanocrystals of complex morphology by sequential cation exchange reactions, *J. Am. Chem. Soc.* **2009**, 131(46), 16851-16857.
53. Robinson, R. D.; Sadtler, B.; Demchenko, D. O.; Erdonmez, C. K.; Wang, L.; Alivisatos, A. P., Spontaneous superlattice formation in nanorods through partial cation exchange, *Science* **2007**, 317(5836), 355-358.
54. Mu, L.; Wang, F.; Sadtler, B.; Loomis, R. A.; Buhro, W. E., Influence of the nanoscale Kirkendall effect on the morphology of copper indium disulfide nanoplatelets synthesized by ion exchange, *ACS Nano* **2015**, 9(7), 7419-7428.
55. Frank, F. C., The influence of dislocations on crystal growth, *Discuss. Faraday Soc.* **1949**, 5, 48-54.
56. Morin, S. A.; Jin, S., Screw dislocation-driven epitaxial solution growth of ZnO nanowires seeded by dislocations in GaN substrates, *Nano Lett.* **2010**, 10(9), 3459-3463.
57. Bierman, M. J.; Lau, Y. K. A.; Kvit, A. V.; Schmitt, A. L.; Jin, S., Dislocation-driven nanowire growth and Eshelby twist, *Science* **2008**, 320(5879), 1060-1063.
58. Millan, A., New method for the production of silver halide tabular crystals, *J. Cryst. Growth*, **2000**, 208, 592-598.

59. Ohzeki, K.; Hosoya, Y., A study on the probability of twin plane formation during the nucleation of AgBr and AgCl crystals in the aqueous gelatin solution, *J. Cryst. Growth*, **2007**, 305, 192-200.
60. Bogels, G.; Pot, T. M.; Meekes, H.; Bennema, P.; Bollen, D., Side-face structure and growth mechanism of tabular silver bromide crystals, *Acta Cryst.* **1997**, A(53), 84-94.
61. Jagannathan, R.; Mehta, R. V.; Timmons, J. A.; Black, D. L., Anisotropic growth of twinned cubic crystals, *Phys. Rev. B* **1993**, 48(18), 13261-13265.
62. Zhu, F.; Men, L.; Guo, Y.; Zhu, Q.; Bhattacharjee, U.; Goodwin, P. M.; Petrich, J. W.; Smith, E. A.; Vela, J., Shape evolution and single particle luminescence of organometal halide perovskite nanocrystals, *ACS Nano* **2015**, 9(3), 2948-2959.
63. Brenner, T. M.; Rakita, Y.; Orr, Y.; Klein, E.; Feldman, I.; Elbaum, M.; Cahen, D.; Hodes, G., Conversion of single crystalline PbI<sub>2</sub> to CH<sub>3</sub>NH<sub>3</sub>PbI<sub>3</sub>: structural relations and transformation dynamics, *Chem. Mater.* **2016**, 28(18), 6501-6510.

## **Chapter 2**

# **Compositionally Induced Twin Defects Control the Shape of Ternary Silver Halide Nanocrystals**

Adapted with permission from (Yin, B.; Huang, X.; Mishra, R.; Sadtler, B., Compositionally induced twin defects control the shape of ternary silver halide nanocrystals, *Chem. Mater.* **2017**, 29(3), 1014-1021.). Copyright (2017) American Chemical Society.

## 2.1 Introduction

In many nano- and microcrystalline catalysts, control over the facets, edges, and corners that make up the crystal surface can be used to enhance catalytic activity.<sup>1-7</sup> A common route to control the shape of crystals grown in solution is to introduce chemical binding agents that selectively adsorb to specific crystalline facets during growth.<sup>8,9</sup> More recently, an alternative method to tune the morphology of nanoscale materials is through the controlled introduction of crystal defects, which has been used to synthesize nanowires and branched structures grown from both solution and vapour phase.<sup>10-12</sup> The termination of an extended defect, such as a stacking fault, screw dislocation, or twin plane, at the surface of the crystal promotes anisotropic growth by serving as a preferential site for the nucleation of new atomic layers.<sup>13-16</sup>

We are interested in controlling the morphology of silver halide nanocrystals for applications in photocatalysis. In photocatalysis using semiconductor particles, the crystalline facets present at the semiconductor–liquid interface affect both the lifetimes and pathways of electron and hole charge carriers and determine the absorption strength of reactant and product molecules during photochemical reactions.<sup>17,18</sup> The solid-state chemistry of silver halide microcrystals has been studied over the last several decades to improve their light sensitivity for use in photography.<sup>19-26</sup> Large platelet microcrystals of AgBr are a desirable morphology for photography as they provide a high surface area for photochemical reactions to take place and can easily be processed into photographic film. More recently, colloidal methods have been developed to synthesize AgBr,

AgCl, and AgI nanocrystals as well as ternary compositions in which the anions either form a solid solution or a phase-segregated mixture.<sup>27-43</sup> Silver halide particles with small clusters of reduced Ag<sup>0</sup> on their surface are active photocatalysts for both the degradation of organic molecules and the reduction of carbon dioxide to produce methanol and ethanol.<sup>32-50</sup> The photocatalytic activity of silver halide nanocrystals has been studied for different compositions and morphologies of single crystal particles<sup>32-43</sup> as well as polycrystalline particles.<sup>44-50</sup> Similar to their increased sensitivity in the photographic process, sheet-like morphologies provide a high surface area for heterogeneous catalysis.<sup>1-4</sup> For example, AgCl and AgBr particles that expose {111} or higher index facets have shown higher activity for photocatalytic dye degradation compared to cubic crystals made up of {100} facets.<sup>34-38,51</sup> For a recent review of the photocatalytic properties of silver halide nanocrystals see reference 50.

As AgCl and AgBr both possess the cubic rock salt structure, AgCl, AgBr, and ternary AgCl<sub>1-x</sub>Br<sub>x</sub> nanocrystals produced by colloidal synthesis often possess cubic morphologies.<sup>30-33</sup> Reports of other morphologies for AgBr nanocrystals have been attributed to selective passivation of specific facets during growth.<sup>36-38</sup> Because of the different crystal structures of AgBr and AgI, we reasoned that an alternative strategy to tune the morphology of silver halide nanocrystals may be to incorporate I<sup>-</sup> into the rock salt AgBr lattice. AgI possesses higher covalency between the ions compared to AgCl and AgBr.<sup>52</sup> At temperatures below 145°C AgI exists in either the wurtzite β-phase or a metastable zinc blend γ-phase.<sup>53,54</sup> AgI nanocrystals with the β-phase typically grow as hexagonal platelets due to the three-fold symmetry of the wurtzite lattice parallel to the {001} facet.<sup>28,41,42</sup> The different crystal structures of AgBr and AgI, as shown in **Figure 2.5**, lead to limited solid solubility for ternary compositions.<sup>55</sup> At room temperature AgBr can dissolve an equilibrium concentration of 16% I<sup>-</sup>, and β-AgI can dissolve up to 4% Br<sup>-</sup>. Thus, previous reports of silver halide nanocrystals containing Br<sup>-</sup> and I<sup>-</sup> consisted

of a phase-segregated mixture of bromide-rich rock salt and iodide-rich wurtzite.<sup>29,45</sup> We adapted methods for the synthesis of  $\text{AgCl}_{1-x}\text{Br}_x$  nanocubes to produce single-phase  $\text{AgBr}_{1-x}\text{I}_x$  nanocrystals.<sup>31</sup> In this chapter we describe the structure and morphology of colloidal  $\text{AgBr}_{1-x}\text{I}_x$  nanocrystals as a function of the anion composition, the effect of iodide substitution on the energy of  $\{111\}$  and  $\{100\}$  facets and planar twin defects, and their role in controlling the nanocrystal shape.

## 2.2 Experimental Details

### 2.2.1 Materials and $\text{AgBr}_{1-x}\text{I}_x$ Nanocrystal Synthesis

*Materials:* Potassium bromide ( $\text{KBr}$ ,  $\geq 99\%$ ), potassium iodide ( $\text{KI}$ ,  $\geq 99\%$ ), silver nitrate ( $\text{AgNO}_3$ ,  $\geq 99\%$ ), polyvinylpyrrolidone (PVP) with an average molecular weight of 40,000, and ethylene glycol (EG,  $\geq 99\%$ ) were purchased from Sigma-Aldrich Inc. Ethanol (EtOH, 190 Proof) was purchased from Decon Labs, Inc. or Pharmco-Aaper. All chemicals were used as received.

*Synthesis of  $\text{AgBr}_x\text{I}_{1-x}$  nanocrystals:* Ternary  $\text{AgBr}_{1-x}\text{I}_x$  nanocrystals were synthesized by a solvothermal method in an ethylene glycol solution following a similar procedure for ternary silver chlorobromide,  $\text{AgCl}_x\text{Br}_{1-x}$  nanocrystals.<sup>31</sup> In a typical reaction, the potassium halide salts,  $\text{KBr}$  and  $\text{KI}$  (a total of 0.34 mmol with varying molar ratio of  $\text{KBr}$  to  $\text{KI}$ ), and 2.5 g of PVP were added to 12 mL of EG in a 3-neck, 50 mL, round-bottom flask. The reaction flask was stirred, purged with nitrogen, and heated to  $60^\circ\text{C}$  using an oil bath and heating/stirring plate for 1.5 hours to dissolve the PVP before injection of the  $\text{AgNO}_3$  solution. Next, 1 mL of a  $\text{AgNO}_3$  solution (0.35 M in ethylene glycol) was injected at a rate of 1 mL/min using a syringe pump.



The reaction was held at a temperature of 60°C under nitrogen and stirred for the entire reaction. Aluminum foil was used to cover the round-bottom flask and keep the reaction in dark. After 2 to 3 hours the reaction flask was removed from the oil bath. **Table 2.1** provides additional details for the synthesis of each sample described in this chapter and their composition as measured by energy dispersive spectroscopy.

After each reaction, the nanocrystal solution was divided into four aliquots of approximately 3 mL, and 30 mL of EtOH was added to each aliquot. The diluted dispersions were centrifuged at 11,000 ( $\times g$ ) for 5 min, and the supernatant from each centrifuge tube was decanted. The nanocrystal precipitate at the bottom of the centrifuge tube was then redispersed in 30 mL of EtOH via sonication. The process of centrifugation, removal of the supernatant, and redispersion of the precipitate were repeated two more times. The nanocrystals were then dispersed in approximately 5 mL of EtOH for further characterization.

## 2.2.2 Details of Characterization

X-ray diffraction (XRD) patterns were collected by a Bruker D8 Advance X-ray Diffractometer (Cu  $K\alpha = 0.15418$  nm). The step size for the XRD measurements was  $0.02^\circ$  in  $2\theta$ , and the scan rate was 0.5 s per step. Several drops of the nanocrystal dispersion were drop-cast onto a zero-background, silicon diffraction plate for XRD (MTI Corporation). The solution was then allowed to dry on the substrate in open air.

Scanning electron microscopy (SEM) images were recorded with a JEOL 7001LVF field-emission scanning electron microscope operated at an acceleration voltage of 8 keV. The SEM was equipped with an energy dispersive X-ray spectrometer (EDS) (Oxford Instruments INCA

Energy 350 Si(Li) X-ray detector EDXS system), and EDS spectra were collected at an acceleration voltage of 15 keV. For SEM imaging, a few drops of nanocrystal dispersion produced after cleaning were diluted by approximately 30 times using EtOH. The diluted solution was drop cast onto a n-type, single crystal silicon substrate with the (111) orientation. Samples for EDS analysis were made more concentrated compared to samples for SEM imaging. ImageJ software was used to measure size distributions of the different ternary  $\text{AgBr}_{1-x}\text{I}_x$  nanocrystal samples from SEM images taken at a magnification of 20,000 $\times$ . At least 100 particles were measured for each sample to obtain the size histograms in **Figure 2.2**. In **Figure 2.9**, 150 nanocrystals from the sample shown in **Figure 2.1e** (Br:I = 11:5) were measured to generate the histogram of the short edge length to the long edge length in the hexagonal prisms.

Transmission electron microscopy (TEM) images and electron beam diffraction patterns were recorded using a JEOL 2000FX transmission electron microscope operated at an acceleration voltage of 200 keV. For TEM imaging a few drops of the nanocrystal dispersion were diluted by approximately 50 times using EtOH. Two drops of the diluted solution were then cast onto a TEM grid (Ted Pella, Inc #01811). After the TEM grid was completely dry, a sputtering system (Cressington 108, vacuum level = 0.2 mbar) was used to deposit gold onto the TEM grid for 90 s under an argon environment. We found that sputtering was necessary to minimize degradation of the silver halide nanocrystals under the electron beam of the TEM.

**Table 2.1:** Reaction conditions used to synthesize  $\text{AgBr}_{1-x}\text{I}_x$  nanocrystals described in this chapter and their composition as measured by EDS

Sample #	Sample shown in Figure X	Reaction time (hours)	Br:I used in reaction	Br:I from EDS	Ag:X from EDS
1	2.1a, 2.3, 2.4a, 2.2a	2	16:0	16:0	1:1
2	2.1b, 2.3, 2.2b	2	15:1	15:1	1:1
3	2.1c, 2.3, 2.2c	3	14:2	14:2	1:1
4	2.1d, 2.3, 2.2d	3	13:3	13.2:2.8	1:0.9
5	2.1e, 2.3, 2.4b, 2.2e, 2.9	2	11:5	11:5	1:1
6	2.1f, 2.3, 2.2f	2	10:6	9.3:6.7	1:1
7	2.6a, 2.7	2	9:7	9:7	1:1
8	2.6b, 2.7	2	8:8	8.2:7.8	1:1
9	2.6c, 2.7	2	3:13	3.3:12.7	1:0.9

## 2.3 Results and Discussion

### 2.3.1 Results

Ternary silver bromiodide,  $\text{AgBr}_{1-x}\text{I}_x$ , nanocrystals were prepared using a similar protocol to the previously reported synthesis of silver chlorobromide nanocrystals.<sup>31</sup> In brief, a solution of silver nitrate ( $\text{AgNO}_3$ ) in ethylene glycol was added to a solution of potassium halide salts (KBr

and KI) and polyvinylpyrrolidone in ethylene glycol at 60°C and stirred for 2 to 3 hours (see **Experimental Details 2.2.1** for full experimental details). The major difference in our procedure was that the molar amount of AgNO<sub>3</sub> (0.35 mmol) was in slight excess relative to the total molar amount of halide ions (0.34 mmol) to ensure consumption of the Br<sup>-</sup> and I<sup>-</sup> anions in the reaction. The average composition of the resulting AgBr<sub>1-x</sub>I<sub>x</sub> nanocrystals as measured by energy dispersive spectroscopy (EDS) closely matched the initial molar ratio of KBr to KI used for each reaction. The EDS results for all the samples used in this chapter are shown in **Table 2.1** at the end of the **Experimental Details**.

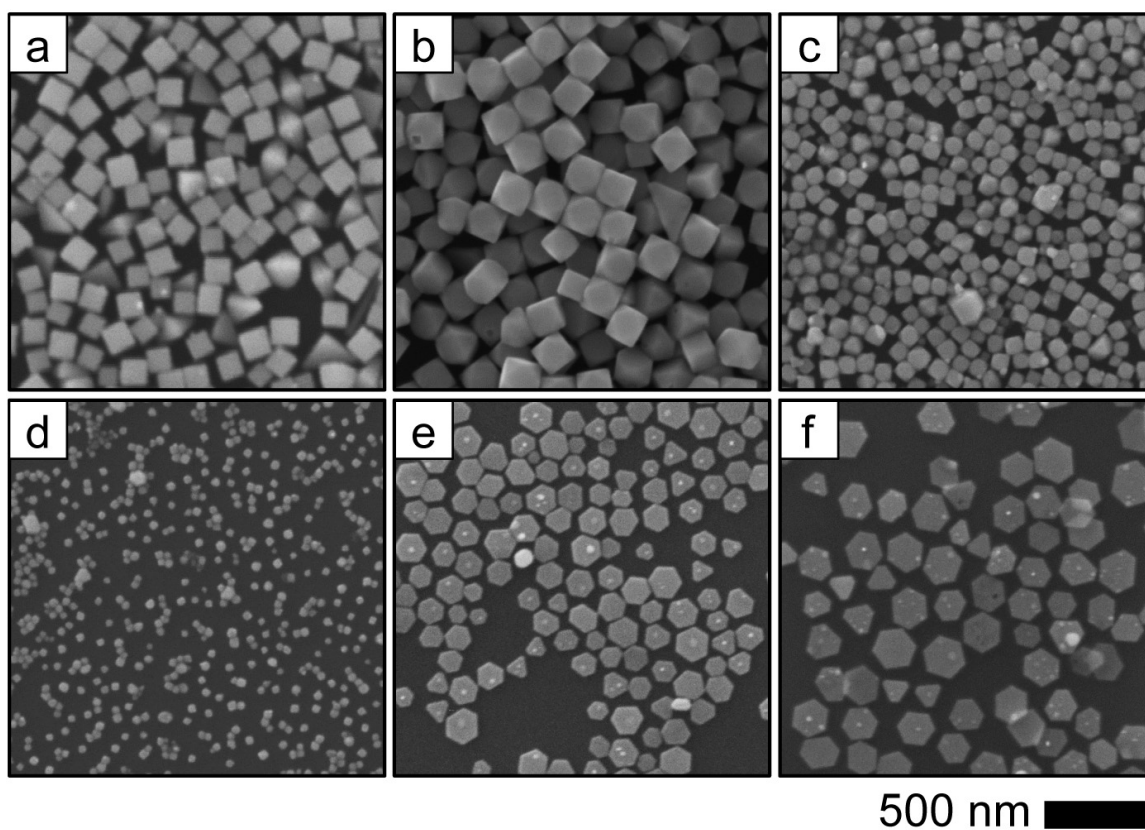


**Figure 2.1.** Scanning electron microscopy (SEM) images of AgBr<sub>1-x</sub>I<sub>x</sub> nanocrystals synthesized with different molar ratios of Br<sup>-</sup> to I<sup>-</sup> anions. (a) Br:I = 16:0 ( $x = 0$ ), (b) Br:I = 15:1 ( $x = 0.06$ ), (c) Br:I = 14:2 ( $x = 0.13$ ) (d) Br:I = 13:3 ( $x = 0.19$ ), (e) Br:I = 11:5 ( $x = 0.31$ ), (f) Br:I=10:6 ( $x = 0.38$ ). The scale bar of 500 nm applies to all images. The higher contrast spots seen on some of the AgBr<sub>1-x</sub>I<sub>x</sub> nanocrystals are formed during imaging due to electron beam damage creating regions of Ag<sup>0</sup> metal.

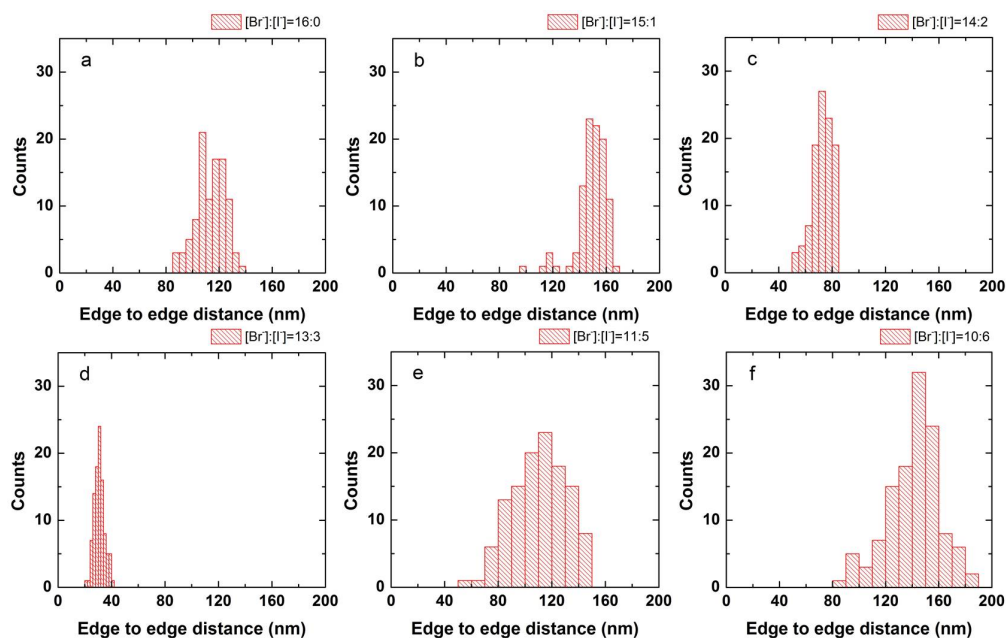


**Figure 2.2.** Size distribution histograms of the  $\text{AgBr}_{1-x}\text{I}_x$  nanocrystals shown in **Figure 2.1**. The ratio of halide anions used to synthesize the nanocrystals were: (a) Br:I = 16:0 ( $x = 0$ ), (b) Br:I = 15:1 ( $x = 0.06$ ), (c) Br:I = 14:2 ( $x = 0.13$ ), (d) Br:I = 13:3 ( $x = 0.19$ ), (e) Br:I = 11:5 ( $x = 0.31$ ), and (f) Br:I=10:6 ( $x = 0.38$ ).

The size and morphology of the  $\text{AgBr}_{1-x}\text{I}_x$  nanocrystals were found to be dependent on the anion composition. **Figure 2.1** shows SEM images of  $\text{AgBr}_{1-x}\text{I}_x$  nanocrystals synthesized using different molar ratios of Br to I. Pure AgBr nanocrystals possessed a cubic shape (**Figure 2.1a**), which has previously been observed for AgBr nanocrystals synthesized by similar methods.<sup>31,32</sup> The average edge length of the cubes was measured to be  $114 \pm 11$  nm (average  $\pm$  1<sup>st</sup> standard deviation from over 100 measurements). Size distribution histograms for each of the samples shown in **Figure 2.1** are provided in **Figure 2.2**. Ternary  $\text{AgBr}_{1-x}\text{I}_x$  nanocrystals over the compositional range  $0.06 < x < 0.19$  (i.e. for Br:I ratios between 15:1 and 13:3) possessed a truncated cubic shape. The size of the particles in this compositional range decreased as the iodide content increased. The average sizes of the particles (as measured by the distance between opposite facets) synthesized with Br:I ratios of 15:1, 14:2, and 13:3 were  $150 \pm 11$  nm,  $73 \pm 7$  nm, and  $31 \pm 4$  nm, respectively (see **Figures 2.1, 2.2**). At a Br:I ratio of 13:3, the

majority of nanocrystals still possessed a truncated cubic shape. Upon increasing the iodide content further, the morphology of the  $\text{AgBr}_{1-x}\text{I}_x$  nanocrystals dramatically changed from truncated cubic to hexagonal prismatic. The lowest iodide content in which we observed the hexagonal prismatic shape was synthesized with a halide ratio  $\text{Br}:\text{I} = 11.5:4.5$  or  $x = 0.28$  (not shown here). However, the size distribution of this sample was broader relative to those shown in **Figure 2.1**. **Figure 2.1e, f** shows hexagonal prismatic nanocrystals synthesized with  $\text{Br}:\text{I}$  ratios of 11:5 and 10:6. The sizes of these hexagonal platelets (as measured by the distance between opposite facets) were  $110 \pm 20$  nm and  $141 \pm 20$  nm, respectively (**Figure 2.2**).

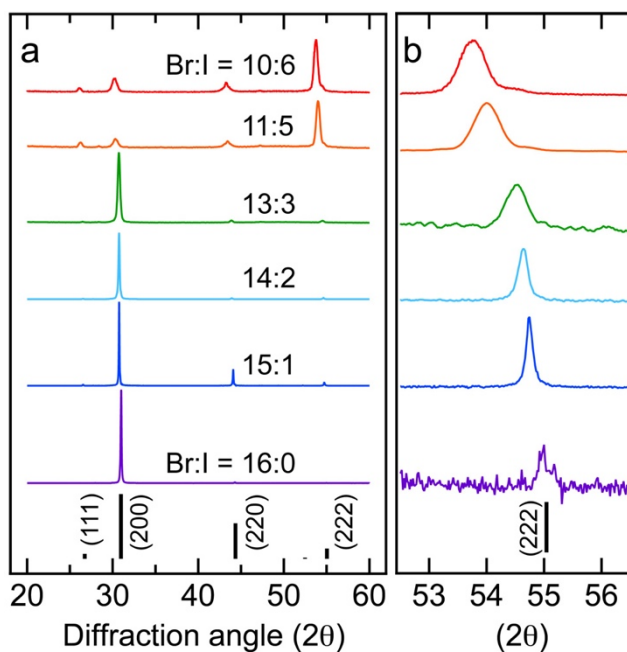


**Figure 2.3.** (a) X-ray diffraction (XRD) patterns of  $\text{AgBr}_{1-x}\text{I}_x$  nanocrystals synthesized with different molar ratios of  $\text{Br}^-$  and  $\text{I}^-$  anions. (b) Expansion of the XRD patterns around the (222) reflection to highlight the peak shift as the anion composition changes. The black lines at the bottom of each plot are the reflections for a standard XRD powder pattern of  $\text{AgBr}$  (JCPDS file: 006-0438).

The ternary  $\text{AgBr}_{1-x}\text{I}_x$  nanocrystals shown in **Figure 2.1** were determined to be single-phase solid solutions possessing the rock salt crystal structure for iodide contents up to  $x = 0.38$ . In the bulk binary phase diagram for  $\text{AgBr} - \text{AgI}$ , the thermodynamic solid solubility limit of  $\text{I}^-$  in

AgBr at 60°C (i.e. the growth temperature we used to synthesize the nanocrystals) was measured to be  $x = 0.17$ .<sup>55</sup> Metastable solid solutions exhibiting greater solubility for I<sup>-</sup> in rock salt AgBr<sub>1-x</sub>I<sub>x</sub> have been observed.<sup>55,56</sup> The **Section 2.3.2** provides further discussion of the AgBr – AgI phase diagram. X-ray diffraction (XRD) patterns of ternary AgBr<sub>1-x</sub>I<sub>x</sub> nanocrystals over the compositional range  $0 \leq x \leq 0.38$  (i.e. for Br:I ratios between 16:0 and 10:6) are shown in **Figure 2.3**. The reflections in each pattern were indexed to the rock salt structure, but with relative peak intensities and peak positions (for compositions with  $x > 0$ ) that differ from the bulk powder pattern for pure AgBr. Comparing the SEM images in **Figure 2.1** to the corresponding diffraction patterns in **Figure 2.3**, the hexagonal platelet nanocrystals occupy a compositional region within the AgBr – AgI phase diagram in which single-phase solid solutions are metastable. For Br:I ratios greater than 10:6, the XRD patterns contained a mixture of two phases, bromide-rich rock salt and iodide-rich wurtzite (shown in **Figures 2.6, 2.7**). With increasing iodide content the intensity of the (200) reflection decreased, and the intensity of the (222) reflection increased and broadened. XRD measurements were performed on drop-cast films prepared in a similar way to the samples shown in **Figure 2.1**, but with colloidal dispersions that were more concentrated to prepare thicker films. Cubes lying flat on one side lead to the (200) atomic planes being preferentially oriented parallel to the substrate. The changes in relative intensity of the (200) and (222) reflections are consistent with the (222) atomic planes becoming preferentially oriented parallel to the substrate as the morphology changes from cubic to truncated cubic to hexagonal prismatic. The broadening of the (222) reflection with increasing iodide content indicates the presence of an increasing number of planar defects parallel to the (222) atomic planes along with a reduction of the crystallite size along the [222] direction.

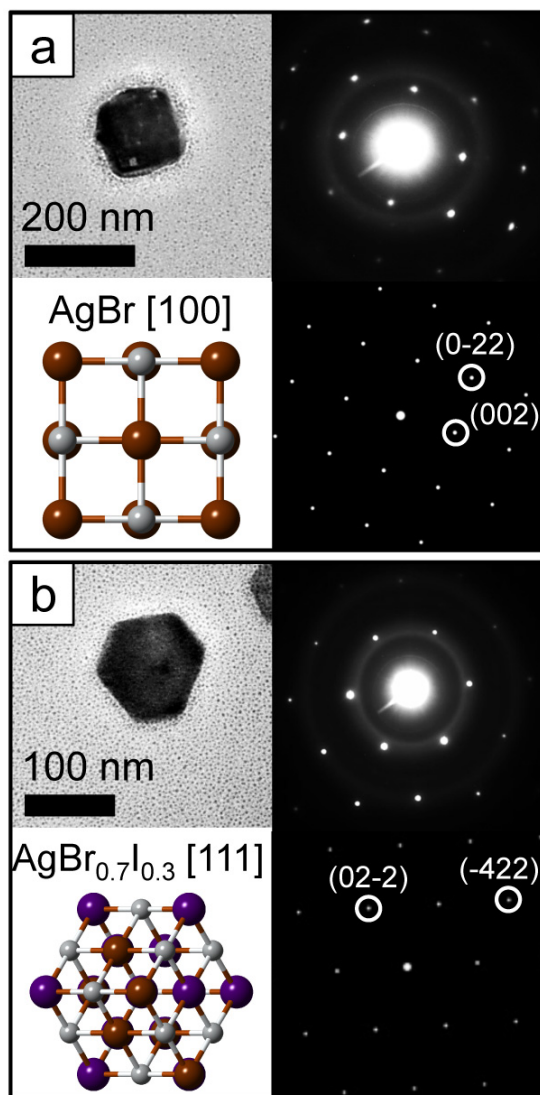


**Figure 2.4.** Transmission electron microscopy (TEM) images and electron diffraction patterns of single  $\text{AgBr}_{1-x}\text{I}_x$  nanocrystals. (a) Pure AgBr nanocrystal with a cubic shape. (b) Hexagonal prismatic  $\text{AgBr}_{1-x}\text{I}_x$  nanocrystal grown using an anion ratio, Br:I = 11:5. The top left panels for both (a) and (b) show a TEM image of the nanocrystal used to measure the electron diffraction pattern, and the top right panels show the corresponding experimental diffraction pattern. The bottom left panels show a model of the crystal lattice either oriented along the [100] zone axis for the pure AgBr nanocrystal in (a) or oriented along the [111] zone axis for the  $\text{AgBr}_{0.7}\text{I}_{0.3}$  nanocrystal in (b). The bottom right panels show simulated electron diffraction patterns for each crystal model.

The SEM images combined with XRD patterns suggest that the predominate crystallographic facets bounding the surface of the  $\text{AgBr}_{1-x}\text{I}_x$  nanocrystals changes from {100} facets to {111} facets as the iodide content increases. Electron diffraction was used to determine the



crystallographic orientation of the rock salt lattice for single nanocrystals with cubic and hexagonal platelet morphologies. **Figure 2.4a** shows a TEM image and the corresponding electron diffraction pattern for a single cubic AgBr nanocrystal. The experimental electron diffraction pattern matches a simulated diffraction pattern for a rock salt AgBr crystal oriented along the [100] zone axis. **Figure 2.4b** shows a TEM image and the corresponding electron diffraction pattern for a single hexagonal prismatic  $\text{AgBr}_{1-x}\text{I}_x$  nanocrystal grown using an anion ratio of Br:I = 11:5 ( $x = 0.31$ ). The electron diffraction pattern matches a simulated diffraction pattern for a rock salt  $\text{AgBr}_{0.7}\text{I}_{0.3}$  crystal oriented along the [111] zone axis. Taken together with the texture effects observed in the XRD patterns, the electron diffraction patterns indicate that the cubic nanocrystals are bound by {100} side facets with {111} facets truncating the cube corners. The hexagonal prismatic nanocrystals are bound by {111} facets as the top and bottom of the platelets.

### 2.3.2 Structures and Binary Phase Diagram of AgBr and AgI

AgBr possesses the cubic, rock salt structure (space group #225,  $a = 5.77 \text{ \AA}$ ,  $Z = 4$ ).<sup>55</sup> AgI often exists as two polymorphs at ambient temperature and pressure, the hexagonal, wurtzite  $\beta$ -phase (space group #186,  $a = 4.59 \text{ \AA}$ ,  $c = 7.51 \text{ \AA}$ ,  $Z = 2$ ) and the cubic, zinc blend  $\gamma$ -phase (space group #216,  $a = 6.50 \text{ \AA}$ ,  $Z = 4$ ).<sup>53,54</sup> The  $\beta$ -phase is considered to be thermodynamically stable and the  $\gamma$ -phase metastable.<sup>57,58</sup> The two phases can easily convert between one another. For example, grinding and pressing AgI powder into a pellet can convert the  $\beta$ -phase into the  $\gamma$ -phase.<sup>57</sup> Both of these close-packed structures transform at a temperature between 144 and 147°C into the cubic  $\alpha$ -phase in which the iodide sublattice adopts a body-centered cubic

arrangement, and the silver ions occupy a statistical distribution of different sites with high mobility.<sup>54,57-58</sup>

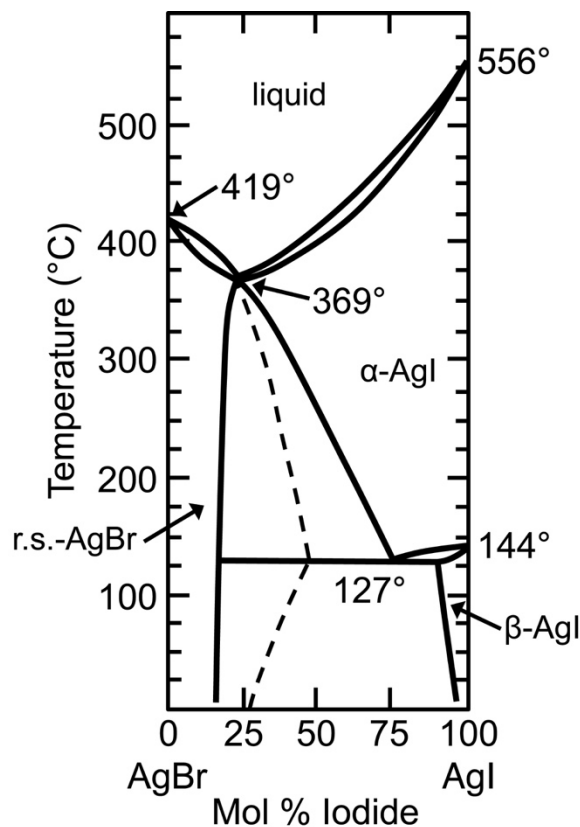


**Figure 2.5.** Sketch of AgBr – AgI phase diagram measured by Groznetskii and co-workers.<sup>55</sup> The single-phase regions possessing the bromide-rich, rock salt structure (r.s.-AgBr), iodide-rich, wurtzite structure ( $\beta$ -AgI), and body-centered cubic structure ( $\alpha$ -AgI) are labeled.

A sketch of the bulk AgBr – AgI phase diagram measured by Groznetskii and co-workers is shown in **Figure 2.5**.<sup>55</sup> The thermodynamic solubility of I<sup>-</sup> in rock salt AgBr<sub>1-x</sub>I<sub>x</sub> at 60°C (i.e. the growth temperature we used to synthesize the nanocrystals) was measured to be  $x = 0.17$ . The dashed line in the phase diagram indicates the existence of metastable solid solutions that were observed with higher solubility of I<sup>-</sup>. The maximum metastable solubility for I<sup>-</sup> in rock salt AgBr<sub>1-x</sub>I<sub>x</sub> was measured to be  $x = 0.47$  at 127°C, and the metastable solubility at 60°C was  $x = 0.36$ . In accordance with this bulk phase diagram we observed that AgBr<sub>1-x</sub>I<sub>x</sub> nanocrystals

synthesized with Br:I ratios up to 10:6 ( $x = 0.375$ ) only showed peaks in their XRD pattern corresponding to rock salt with no detectable peaks from wurtzite. In an earlier phase diagram measured by Takahashi and co-workers the maximum solubility of I<sup>-</sup> in  $\text{AgBr}_{1-x}\text{I}_x$  was measured to be  $x = 0.48$  at 128°C.<sup>56</sup> Takahashi et al. considered the metastable boundary (i.e. dashed line in **Figure 2.5**) measured by Groznetskii et al. to be the thermodynamically stable phase boundary between a rock salt  $\text{AgBr}_{1-x}\text{I}_x$  solid solution and the two-phase region containing a bromide-rich, rock salt phase and an iodide-rich, wurtzite phase. The discrepancy between whether this phase boundary is a thermodynamically stable or a kinetically metastable boundary may be due to the presence of cubic  $\gamma$ -AgI. The zinc blend  $\gamma$ -phase of AgI is structurally more similar with rock salt AgBr than the wurtzite  $\beta$ -phase is with AgBr (i.e. in both zinc blend and rock salt the anions possess a face-centered cubic arrangement). Therefore, the presence of metastable  $\gamma$ -AgI would likely increase the solubility of I<sup>-</sup> in AgBr.

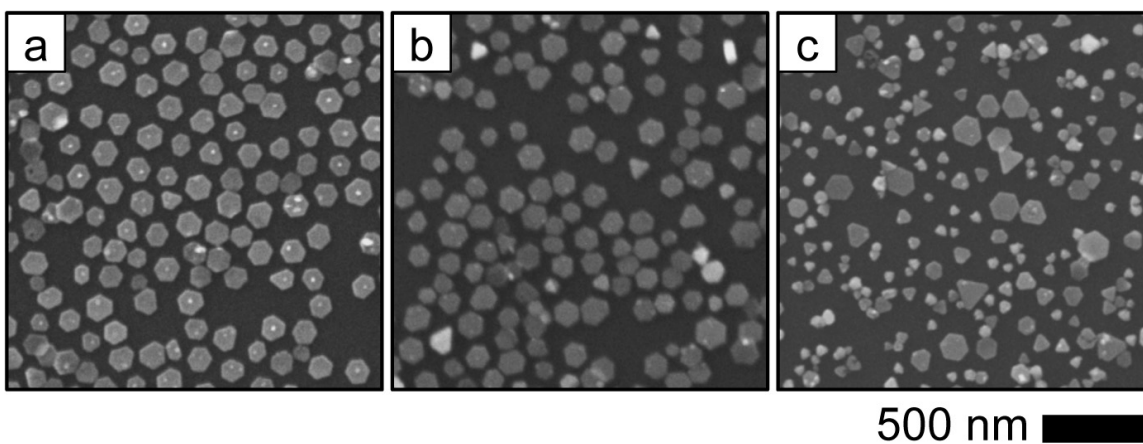


**Figure 2.6.** SEM images of  $\text{AgBr}_{1-x}\text{I}_x$  nanocrystals synthesized with higher iodide contents. The ratio of halide anions used to synthesize the nanocrystals were: (a) Br:I = 9:7 ( $x = 0.44$ ), (b) Br:I = 8:8 ( $x = 0.50$ ), (c) Br:I = 3:13 ( $x = 0.81$ ). The scale bar of 500 nm applies to all images.

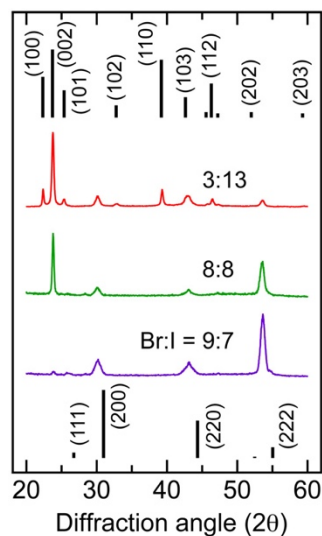


**Figure 2.7.** X-ray diffraction (XRD) patterns of  $\text{AgBr}_{1-x}\text{I}_x$  nanocrystals. The Br:I ratios are provided above each pattern. The black lines at the bottom of the plot are the reflections for a standard XRD powder pattern of AgBr (JCPDS file: 006-0438). The black lines at the top of the plot are the reflections for a standard XRD powder pattern of  $\beta$ -AgI (JCPDS file: 009-0374). The major hkl indices for the reflections in the two standard patterns are labeled.

We observed phase segregation in  $\text{AgBr}_{1-x}\text{I}_x$  nanocrystals synthesized using iodide contents with  $x > 0.4$ . For  $\text{AgBr}_{1-x}\text{I}_x$  nanocrystals synthesized with Br:I ratios of 9:7, 8:8, and 3:13 (i.e.  $0.44 < x < 0.81$ ), the morphology was still observed to be hexagonal prismatic, but the size distribution increased with iodide content (**Figure 2.6**). XRD patterns of these samples show reflections belonging to both the bromide-rich, rock salt and iodide-rich wurtzite phases (**Figure 2.7**). As the iodide content increases the intensity of peaks belonging to the wurtzite phase, such as the (002), (110), and (112) reflections increase while peaks belonging to the rock salt phase decrease.

### 2.3.3 Twin Boundary and Hexagonal Prismatic Morphology

The incorporation of iodide at sufficient concentration in the ternary  $\text{AgBr}_{1-x}\text{I}_x$  nanocrystals induced a change in their morphology from cubic to hexagonal prismatic while retaining the rock salt structure. The shape of these hexagonal prismatic  $\text{AgBr}_{1-x}\text{I}_x$  nanocrystals is similar to the platelet, or tabular AgBr microcrystals used in photographic film.<sup>19-23</sup> The mechanism of anisotropic growth leading to tabular AgBr microcrystals has been attributed to the formation of planar twin defects parallel to  $\{111\}$  facets during nucleation of the crystal. Enhanced lateral growth of the side facets produces the platelet morphology with (111) and (-1-1-1) facets forming the top and bottom surfaces of the tabular crystal. Several reports have suggested different structures for the side facets of tabular AgBr microcrystals, but it is generally agreed upon that the sides are composed of  $\{111\}$  and  $\{100\}$  facets.<sup>19-23</sup> **Figure 2.8** shows models for cuboctahedral nuclei of silver halide crystals with varying numbers of twin planes parallel to the top and bottom  $\{111\}$  facets. These models are based on some of the side-facet structures previously observed for millimeter scale AgBr single crystals that were large enough to measure the relative angles of the side facets by SEM.<sup>22</sup> In comparing the models in **Figure 2.8a** and **2.8b**, it can be seen that a single twin plane is equivalent to rotating the bottom half of the crystal by  $60^\circ$ . For the single twin defect shown in **Figure 2.8b**,  $\{100\}$  facets on the top half of the crystal connect with  $\{100\}$  facets on the bottom half; the same is true for  $\{111\}$  facets connecting on either side of the twin plane. Multiple twin boundaries (**Figure 2.8c, d**) lead to connections between  $\{100\}$  and  $\{111\}$  facets on either side of the twin boundary, which produce ridges and grooves on the sides of the crystal.

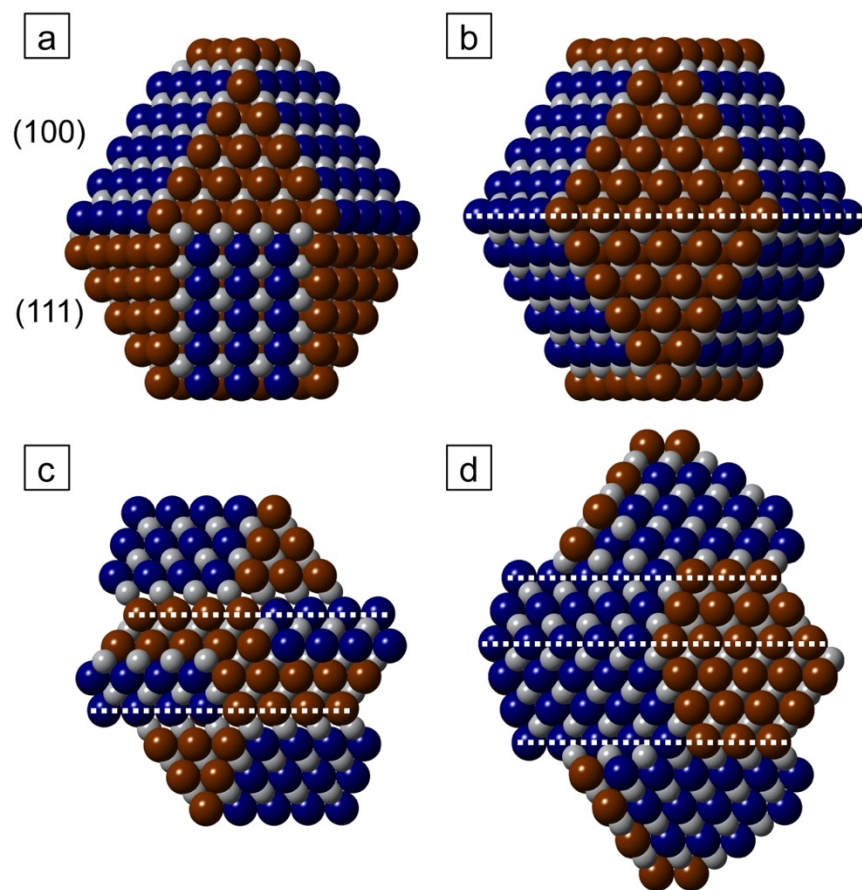


**Figure 2.8.** Models of silver halide crystal nuclei possessing varying numbers of twin boundaries. (a) Defect-free cuboctahedral crystal bound by  $\{100\}$  and  $\{111\}$  facets. The silver ions are colored grey. Halide anions on a  $\{111\}$  surface facet are colored reddish brown, and halide anions on a  $\{100\}$  surface facet are colored dark blue. (b) Cuboctahedral nuclei with a single twin boundary denoted by the dashed white line parallel to the  $\{111\}$  facets on the top and bottom of the crystal. (c) Silver halide crystal nuclei possessing two twin boundaries and (d) silver halide crystal nuclei with three twin boundaries showing the ridge and grooves that make up the sides of crystals possessing multiple parallel twin planes.

The hexagonal prismatic shape is likely formed in a kinetically controlled regime based on differences in growth rates for the sides and basal surfaces of the platelet.<sup>8</sup> In the growth model developed for tabular AgBr crystals (which has been extended to other face-centered cubic crystals with planar defects, such as stacking faults), twin boundaries create a substep where the two side facets meet at the edge of the twin boundary.<sup>14-16,19-23</sup> This substep can serve as a continuous source for the addition of new layers on both sides of the ridge or groove formed by

the twin defect and promote anisotropic growth. The growth model is similar to the self-perpetuating step source provided by a screw dislocation that extends to a crystal surface as proposed by Frank<sup>13</sup> and which has been observed to cause one-dimensional growth of PbS and ZnO nanostructures.<sup>11,12</sup> In the growth model developed by Bögels and coworkers, nucleation of a new atomic layer occurs preferentially either on a {100} facet or the substep where a {100} and {111} facets meet.<sup>22</sup> Once the growth of a new layer has occurred on the {100} surface it will continue to grow on the adjoining {111} surface. Thus, preferential nucleation on the {100} facet combined with the substep due to the twin defect enhances the growth rate of the adjoining {111} facet.

For a hexagonal prismatic crystal where the top {111} face has three-fold rotational symmetry it is possible to have two types of side-facet structures that alternate on the six sides of the hexagon. As shown in **Figure 2.8c**, the presence of two twin planes (or any even number of twin planes) leads to identical structures for the side facets on opposite sides of the hexagonal prismatic crystal. In this case, the growth rate of all sides will be similar leading to hexagonal prisms with six sides of near equal length. The structures in **Figure 2.8b** and **d** show that the presence of an odd number of twin planes creates different surfaces on opposite sides of the crystal. The different growth rates of the two side-facet structures will produce truncated triangular prisms (i.e. hexagons with three sides shorter than the other three).<sup>22</sup> The distribution in the relative edge length of the two side facets for the platelet nanocrystals shown in **Figure 2.1e** (Br:I = 11:5) is provided in **Figure 2.9**. Of the 150 nanocrystals measured, 56% possessed edges with less than a 15% difference in length suggesting that a high percentage of nanocrystals contain multiple parallel twin defects.

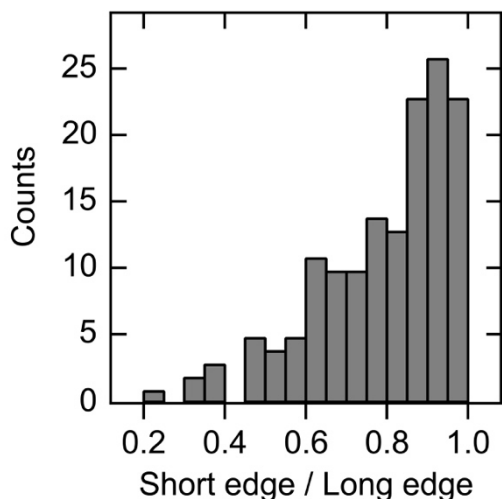


**Figure 2.9.** Histogram of the ratio of short edge length to long edge length for hexagonal platelet  $\text{AgBr}_{1-x}\text{I}_x$  nanocrystals synthesized with a Br:I ratio of 11:5. Of the 150 nanocrystals measured, 56% possessed edge lengths with less than a 15% difference. A SEM image of this sample is shown in **Figure 2.1e**.

In several models for anisotropic growth of AgBr tabular crystals the  $\{100\}$  side facets are assumed to have a faster growth rate than the  $\{111\}$  facets.<sup>21-23</sup> In the rock salt structure each ion exposed on a  $\{100\}$  surface is missing one coordination site, while on a  $\{111\}$  surface each ion is missing three coordination sites. Consequently, the barrier for two-dimensional nucleation of a new layer is lower on a  $\{100\}$  surface. As shown in **Figure 2.8b**, a single twin defect creates two types of side-facet structures where either two  $\{100\}$  or two  $\{111\}$  facets meet at the twin boundary. In this case, the sides bounded by  $\{100\}$  facets will grow faster than those bound by  $\{111\}$  facets leading to a crystal only bound by  $\{111\}$  facets. Once the crystal is completely composed of  $\{111\}$  surfaces then growth will slow down.<sup>22</sup> During the long crystallization times used to grow microscale and milliscale AgBr crystals (ranging from several days to a month) crystals with a single twin defect are believed to dissolve through Ostwald ripening at the expense of faster growing crystals.<sup>22</sup> Consequently, several studies that examined the number of twin planes in tabular AgBr microcrystals found predominantly two parallel twin planes per crystal with a minority fraction of the crystals possessing three parallel twin planes.<sup>20-22</sup>



Previous studies of twin defect formation leading to hexagonal platelet crystals were conducted on pure AgBr.<sup>19-23</sup> In these cases, excess bromide in the growth solution relative to the silver ion concentration was shown to produce tabular microcrystals by stabilizing the {111} surface facets and introducing twin defects in AgBr.<sup>21-23,26</sup> We used a slight excess of AgNO<sub>3</sub> (0.35 mmol) relative to the total concentration of potassium halide (0.34 mmol) to ensure all the halide ions were consumed. In one recent report, AgBr nanoplates were synthesized by nearly identical conditions to the AgBr nanocubes shown in **Figure 2.1a**, with the only differences being that an excess of sodium bromide was used, and the temperature was raised from 60° to 160°C during the reaction.<sup>37</sup> The growth of these AgBr hexagonal nanoplates was attributed to selective binding of PVP to the polar {111} surface facets. However, the use of excess bromide to achieve the platelet shape along with the observation by us and others that the same amount of PVP will produce cubic crystals when the Ag<sup>+</sup>:Br<sup>-</sup> ratio is close to 1:1 suggest that twin defects may play a role in producing the nanoplate shape.<sup>31</sup>

### **2.3.4 Density Functional Theory (DFT) Calculations of the Ternary AgBr<sub>1-x</sub>I<sub>x</sub> System**

The pure AgBr nanocrystals we synthesized are completely bound by {100} surfaces, indicating they are free of twin defects. The experimentally observed cubic shape for pure AgBr is in good agreement with the lower energy of the (100) surface compared to the Br-terminated (111) surface obtained using density functional theory (DFT) calculations (Results are given in the original paper).<sup>59</sup> The addition of low concentrations of I<sup>-</sup> caused truncation of the corners of the nanocubes by {111} facets (**Figure 2.1b, c**) and at higher concentrations induced twin defects during nucleation of the AgBr<sub>1-x</sub>I<sub>x</sub> nanocrystals (**Figure 2.1e, f**). To understand the effect

of  $I^-$  substitution on the crystal growth, we have calculated the formation energy of a single  $I_{Br}$  substitutional defect on both (100) and (111) surfaces. The representative relaxed structures of AgBr slabs with (100) and (111) surfaces having a single  $I_{Br}$  substitutional defect at the surface are shown in **Figure 2.10a**. We have also calculated the formation energy of  $I_{Br}$  as a function of its distance from both of these surfaces. We observe that the formation energy increases upon moving away from the surface and towards the bulk of the crystal (see **Figure 2.10b**).  $I^-$  ions (2.2 Å) have a larger ionic radius than  $Br^-$  ions (1.96 Å). The lower formation energy of  $I_{Br}$  at the surface, where it has more space compared to the bulk, can likely be attributed to the lowering of strain energy. To test this hypothesis, we have calculated the formation energy of  $I_{Br}$  in bulk AgBr by increasing its volume isotropically. We find that the formation energy decreases monotonically on increasing the volume of AgBr as shown in **Figure 2.10c**, which confirms that it is indeed the strain energy that favors  $I_{Br}$  substitution at the surface. However, we observe that the formation energy for  $I_{Br}$  on the Br-terminated (111) surface is significantly lower (-0.54 eV) than on the (100) surface (0.38 eV). At both the (100) surface and the Br-terminated (111) surface,  $I_{Br}$  is coordinated with three neighboring Ag atoms, while in the bulk crystal  $I_{Br}$  is coordinated with six neighboring Ag atoms. The average Ag-I bond length for  $I_{Br}$  on the Br-terminated (111) surface (2.82 Å) compared to that on the (100) surface (2.76 Å) is closer to the Ag-I bond length within bulk AgI (2.87 Å), which lowers the strain energy around the  $I_{Br}$  substitution and thus stabilizes the defect on the (111) surface. The negative formation energy for the (111) surface indicates that  $I_{Br}$  defects form spontaneously on the (111) surface lowering its surface energy. These results strongly suggest that iodide substitution stabilizes the {111} facets over the {100} facets and are consistent with our experimental observations.

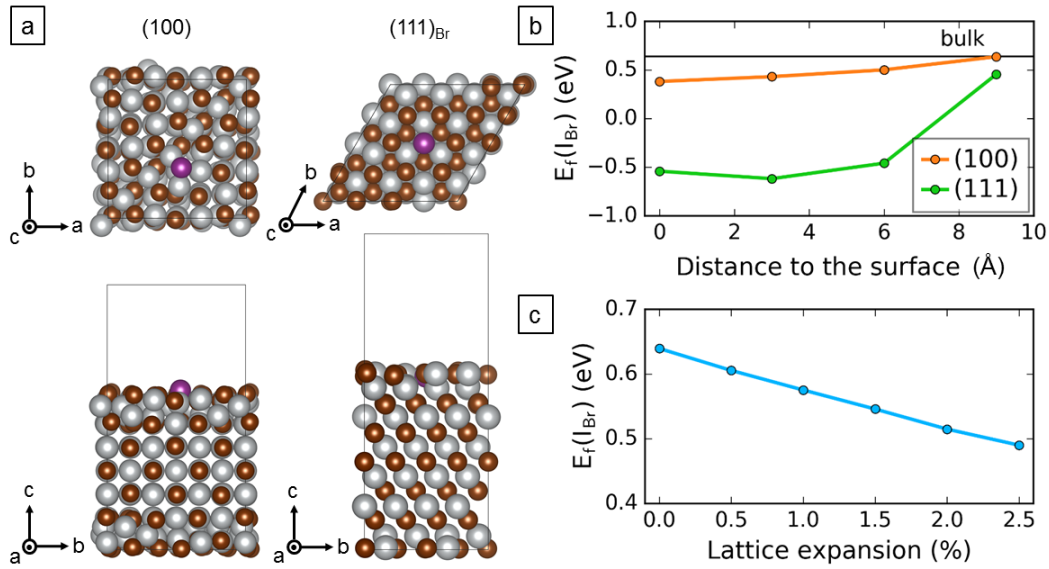


**Figure 2.10** (a) Slab models with a single iodide substitutional defect,  $I_{Br}$ , at the (100) surface and Br-terminated (111) surface of AgBr. The silver ions are colored grey. Bromide ions are colored reddish brown, and substitutional iodide ions are colored purple. (b) Calculated formation energy of  $I_{Br}$  substitutional defect at (100) and (111) surfaces as a function of its distance from the surface. (c) Formation energy of an  $I_{Br}$  substitutional defect within bulk AgBr as a function of increasing lattice constant.

As the probability for twin defect formation is proportional to number of  $\{111\}$  surfaces in the crystal, the presence of these  $\{111\}$  facets during the early stages of nucleation and growth increases the likelihood of twin defect formation.<sup>23</sup> Our calculations show that (111)[111](60°) twin boundaries possess a small formation energy of  $1.19 \times 10^{-3} \text{ eV}/\text{\AA}^2$  and can therefore form easily. In addition, formation of  $I_{Br}$  substitutional defects within the twin boundaries remains similar to their formation energy of 0.63 eV in bulk AgBr (Calculation results are not shown here).<sup>59</sup> Taken together, the experiments and the calculations are consistent with a mechanism in which stabilization of  $\{111\}$  surface facets in the  $\text{AgBr}_{1-x}\text{I}_x$  nanocrystals by preferential iodide segregation in combination with the low formation energy of twin defects parallel to these  $\{111\}$  surfaces changes the growth of the nanocrystal from isotropic (i.e. cubic) to anisotropic (i.e.

hexagonal prismatic). More details of the way the DFT calculations were conducted can be found in our original paper.<sup>59</sup>

The presence of planar defects, including twin planes and stacking faults, alter the electronic structure and photophysical properties of semiconductor nanostructures.<sup>10,60-64</sup> Twin planes in AgBr act as preferential locations for photochemical reduction of  $\text{Ag}^+$  leading to  $\text{Ag}^0$  grains that are the active sites in silver halide photography and photocatalysis.<sup>50,60</sup> Phase-pure, wurtzite CdSe nanowires exhibit significantly narrower photoluminescent line widths relative to nanowires that possess stacking faults and wurtzite–zinc blend polytypism.<sup>64</sup> Currently, there are a few examples in the literature where the cation or anion composition in ternary semiconductor nanostructures has been used to engineer such two-dimensional defects.<sup>10,61,62</sup> For example, impurity-induced twinning has been observed during the vapor–liquid–solid (VLS) growth of InP nanowires.<sup>10</sup> When InP nanowires were doped with a sufficient concentration of Zn, a superlattice of twin planes formed perpendicular to the nanowire growth direction. We suggest that tuning the composition in ternary semiconductors may provide a general method to control the defect structure and resulting properties of nanoplates, nanowires, and other nanostructures.

## 2.4 Conclusions

The morphology of ternary  $\text{AgBr}_{1-x}\text{I}_x$  nanocrystals was observed to evolve from cubic to hexagonal prismatic, as the anion composition became increasingly iodide rich. Consistent with the experimental observation that the relative surface area of  $\{111\}$  facets increases with iodide content, our DFT calculations indicate that iodide preferentially segregates to the surface of these crystals and stabilizes  $\{111\}$  surfaces. In our model, the nucleation of twin planes parallel to these  $\{111\}$  surfaces occurs due to their low formation energy and produces the change in morphology. The termination of a twin boundary at the crystal surface provides a self-perpetuating substep, enhancing lateral growth of the crystal. The ability to systematically tune the composition and morphology of  $\text{AgBr}_{1-x}\text{I}_x$  nanocrystals may be used to further develop structure–activity relationships and understand how different surface facets affect the stability and photocatalytic activity of this material system.

## 2.5 Acknowledgements

I would like to thank Professor William Buhro for letting me use his lab and equipment to conduct the synthesis of nanocrystals. I also want to thank Dr. Xing Huang and Professor Rohan Mishra to help conduct the DFT calculations. Dr. Fudong Wang, Dr. Linjia Mu and Dr. Yang Zhou gave me a lot of help in synthesis and characterization of nanocrystals. Thank Professor William Buhro and Professor Richard Loomis for useful discussions of this work. Also our technician, Dr. Huafang Li, assist me with TEM imaging.

## 2.6 References

1. Jaramillo, T. F.; Jorgensen, K. P.; Bonde, J.; Nielsen, J. H.; Horch, S.; Chorkendorff, I. Identification of the Active Edge Sites for Electrochemical H<sub>2</sub> Evolution from MoS<sub>2</sub> Nanocatalysts *Science* **2007**, *317*, 100-102.
2. Liu, G.; Sun, C.; Yang, H. G.; Smith, S. C.; Wang, L.; Lu, G. Q.; Cheng, H.-M. Nanosized Anatase TiO<sub>2</sub> Single Crystals for Enhanced Photocatalytic Activity *Chem. Commun.* **2010**, *46*, 755-757.
3. Wang, D.; Jiang, H.; Zong, X.; Xu, Q.; Ma, Y.; Li, G.; Li, C. Crystal Facet Dependence of Water Oxidation on BiVO<sub>4</sub> Sheets under Visible Light Irradiation *Chem. Euro. J.* **2011**, *17*, 1275-1282.
4. Xie, Y. P.; Liu, G.; Yin, L.; Cheng, H.-M. Crystal Facet-Dependent Photocatalytic Oxidation and Reduction Activity of Monoclinic WO<sub>3</sub> for Solar Energy Conversion *J. Mater. Chem.* **2012**, *22*, 6746-6751.
5. Zhang, Y.; Deng, B.; Zhang, T.; Gao, D.; Xu, A.-W. Shape Effects of Cu<sub>2</sub>O Polyhedral Microcrystals on Photocatalytic Activity *J. Phys. Chem. C* **2010**, *114*, 5073-5079.
6. Martin, D. J.; Umezawa, N.; Chen, X.; Ye, J.; Tang, J. Facet Engineered Ag<sub>3</sub>PO<sub>4</sub> for Efficient Water Photooxidation *Energy Environ. Sci.* **2013**, *6*, 3380-3386.
7. Zhu, W.; Michalsky, R.; Metin, Ö.; Lv, H.; Guo, S.; Wright, C. J.; Sun, X.; Peterson, A. A.; Sun, S. Monodisperse Au Nanoparticles for Selective Electrocatalytic Reduction of CO<sub>2</sub> to CO *J. Am. Chem. Soc.* **2013**, *135*, 16833-16836.

8. Yin, Y.; Alivisatos, A. P. Colloidal Nanocrystal Synthesis at the Organic-Inorganic Interface *Nature* **2005**, *437*, 664-670.
9. Choi, K.-S. Shape Control of Inorganic Materials via Electrodeposition *Dalton Trans.* **2008**, 5432-5438.
10. Algra, R. E.; Verheijen, M. A.; Borgstrom, M. T.; Feiner, L.-F.; Immink, G.; van Enkevort, W. J. P.; Vlieg, E.; Bakkers, E. P. A. M. Twinning Superlattices in Indium Phosphide Nanowires *Nature* **2008**, *456*, 369-372.
11. Bierman, M. J.; Lau, Y. K. A.; Kvit, A. V.; Schmitt, A. L.; Jin, S. Dislocation-Driven Nanowire Growth and Eshelby Twist *Science* **2008**, *320*, 1060-1063.
12. Morin, S. A.; Jin, S. Screw Dislocation-Driven Epitaxial Solution Growth of ZnO Nanowires Seeded by Dislocations in GaN Substrates *Nano Lett.* **2010**, *10*, 3459-3463.
13. Frank, F. C. The Influence of Dislocations on Crystal Growth *Discuss. Faraday Soc.* **1949**, *5*, 48-54.
14. Ming, N.-B.; Sunagawa, I. Twin Lamellae as Possible Self-Perpetuating Step Sources *J. Cryst. Growth* **1988**, *87*, 13-17.
15. Sunkara, M.; Angus, J. C.; Hayman, C. C.; Buck, F. A. Nucleation of Diamond Crystals *Carbon* **1990**, *28*, 745-746.
16. Ming, N.-B.; Li, H. Twin Lamella Mechanism of FCC Crystal Growth: The Monte-Carlo Simulation Approach *J. Cryst. Growth* **1991**, *115*, 199-202.

17. Tan, M. X.; Laibinis, P. E.; Nguyen, S. T.; Kesselman, J. M.; Stanton, C. E.; Lewis, N. S. Principles and Applications of Semiconductor Photoelectrochemistry *Prog. Inorg. Chem.* **1994**, *41*, 21-144.
18. Choi, K.-S. Shape Effect and Shape Control of Polycrystalline Semiconductor Electrodes for Use in Photoelectrochemical Cells *J. Phys. Chem. Lett.* **2010**, *1*, 2244-2250.
19. Berriman, R. W.; Herz, R. H. Twinning and the Tabular Growth of Silver Bromide Crystals *Nature* **1957**, *180*, 293-294.
20. Hamilton, J. F.; Brady, L. E. Twinning and Growth of Silver Bromide Microcrystals *J. Appl. Phys.* **1964**, *35*, 414-421.
21. Jagannathan, R.; Mehta, R. V.; Timmons, J. A.; Black, D. L. Anisotropic Growth of Twinned Cubic Crystals *Phys. Rev. B* **1993**, *48*, 13261-13265.
22. Bögels, G.; Pot, T. M.; Meekes, H.; Bennema, P.; Bollen, D. Side-Face Structure and Growth Mechanism of Tabular Silver Bromide Crystals *Acta Crystallogr., Sect. A* **1997**, *53*, 84-94.
23. Ohzeki, K.; Hosoya, Y. A Study on the Probability of Twin Plane Formation During the Nucleation of AgBr and AgCl Crystals in the Aqueous Gelatin Solution *J. Cryst. Growth* **2007**, *305*, 192-200.
24. Bögels, G.; Buijnsters, J. G.; Verhaegen, S. A. C.; Meekes, H.; Bennema, P.; Bollen, D. Morphology and Growth Mechanism of Multiply Twinned AgBr and AgCl Needle Crystals *J. Cryst. Growth* **1999**, *203*, 554-563.



25. Millan, A.; Bennema, P.; Verbeeck, A.; Bollen, D. In Situ Observations of Silver Bromide Tabular Crystal Growth *J. Chem. Soc., Faraday Trans.* **1998**, *94*, 2195-2198.
26. Millan, A. New Method for the Production of Silver Halide Tabular Crystals *J. Cryst. Growth* **2000**, *208*, 592-598.
27. Oleshko, V. P.; Van Daele, A.; Gijbels, R. H.; Jacob, W. A. Structural and Analytical Characterization of Ag(Br,I) Nanocrystals by Cryo-AEM Techniques *Nanostruct. Mater.* **1998**, *10*, 1225-1246.
28. Guo, Y.-G.; Lee, J.-S.; Maier, J. Preparation and Characterization of AgI Nanoparticles with Controlled Size, Morphology and Crystal Structure *Solid State Ion.* **2006**, *177*, 2467-2471.
29. Nikolenko, D. Y.; Brichkin, S. B.; Razumov, V. F. Synthesis of Mixed Silver Halide Nanocrystals in Reversed Micelles *High Energy Chem.* **2008**, *42*, 305-310.
30. Peng, S.; Sun, Y. Ripening of Bimodally Distributed AgCl Nanoparticles *J. Mater. Chem.* **2011**, *21*, 11644-11650.
31. Li, Z.; Okasinski, J. S.; Gosztola, D. J.; Ren, Y.; Sun, Y. Silver Chlorobromide Nanocubes with Significantly Improved Uniformity: Synthesis and Assembly into Photonic Crystals *J. Mater. Chem. C* **2015**, *3*, 58-65.
32. Cai, B.; Wang, J.; Han, D.; Gan, S.; Zhang, Q.; Wu, Z.; Niu, L. Ternary Alloyed AgCl<sub>x</sub>Br<sub>1-x</sub> Nanocrystals: Facile Modulation of Electronic Structures toward Advanced Photocatalytic Performance *Nanoscale* **2013**, *5*, 10989-10995.

33. An, C.; Peng, S.; Sun, Y. Facile Synthesis of Sunlight-Driven AgCl:Ag Plasmonic Nanophotocatalyst *Adv. Mater.* **2010**, *22*, 2570-2574.
34. Zhu, M.; Chen, P.; Liu, M. Sunlight-Driven Plasmonic Photocatalysts Based on Ag/AgCl Nanostructures Synthesized Via an Oil-in-Water Medium: Enhanced Catalytic Performance by Morphology Selection *J. Mater. Chem.* **2011**, *21*, 16413-16419.
35. Lou, Z.; Huang, B.; Qin, X.; Zhang, X.; Cheng, H.; Liu, Y.; Wang, S.; Wang, J.; Dai, Y. One-Step Synthesis of AgCl Concave Cubes by Preferential Overgrowth Along  $\langle 111 \rangle$  and  $\langle 110 \rangle$  Directions *Chem. Commun.* **2012**, *48*, 3488-3490.
36. Wang, H.; Lang, X.; Gao, J.; Liu, W.; Wu, D.; Wu, Y.; Guo, L.; Li, J. Polyhedral AgBr Microcrystals with an Increased Percentage of Exposed  $\{111\}$  Facets as a Highly Efficient Visible-Light Photocatalyst *Chem. Euro. J.* **2012**, *18*, 4620-4626.
37. Wang, H.; Gao, J.; Guo, T.; Wang, R.; Guo, L.; Liu, Y.; Li, J. Facile Synthesis of AgBr Nanoplates with Exposed  $\{111\}$  Facets and Enhanced Photocatalytic Properties *Chem. Commun.* **2012**, *48*, 275-277.
38. Wang, H.; Yang, J.; Li, X.; Zhang, H.; Li, J.; Guo, L. Facet-Dependent Photocatalytic Properties of AgBr Nanocrystals *Small* **2012**, *8*, 2802-2806.
39. Li, B.; Wang, H.; Zhang, B.; Hu, P.; Chen, C.; Guo, L. Facile Synthesis of One Dimensional AgBr@Ag Nanostructures and Their Visible Light Photocatalytic Properties *ACS Appl. Mater. Interfaces* **2013**, *5*, 12283-12287.

40. An, C.; Wang, J.; Jiang, W.; Zhang, M.; Ming, X.; Wang, S.; Zhang, Q. Strongly Visible-Light Responsive Plasmonic Shaped AgX:Ag (X = Cl, Br) Nanoparticles for Reduction of CO<sub>2</sub> to Methanol *Nanoscale* **2012**, *4*, 5646-5650.
41. Feng, S.; Xu, H.; Liu, L.; Song, Y.; Li, H.; Xu, Y.; Xia, J.; Yin, S.; Yan, J. Controllable Synthesis of Hexagon-Shaped  $\beta$ -AgI Nanoplates in Reactable Ionic Liquid and Their Photocatalytic Activity *Colloids Surf., A* **2012**, *410*, 23-30.
42. Jiang, W.; An, C.; Liu, J.; Wang, S.; Zhao, L.; Guo, W.; Liu, J. Facile Aqueous Synthesis of  $\beta$ -AgI Nanoplates as Efficient Visible-Light-Responsive Photocatalyst *Dalton Trans.* **2014**, *43*, 300-305.
43. An, C.; Liu, J.; Wang, S.; Zhang, J.; Wang, Z.; Long, R.; Sun, Y. Concaving AgI Sub-Microparticles for Enhanced Photocatalysis *Nano Energy* **2014**, *9*, 204-211.
44. Wang, P.; Huang, B.; Qin, X.; Zhang, X.; Dai, Y.; Wei, J.; Whangbo, M.-H. Ag@AgCl: A Highly Efficient and Stable Photocatalyst Active under Visible Light *Angew. Chem. Int. Ed.* **2008**, *47*, 7931-7933.
45. Wang, P.; Huang, B.; Zhang, Q.; Zhang, X.; Qin, X.; Dai, Y.; Zhan, J.; Yu, J.; Liu, H.; Lou, Z. Highly Efficient Visible Light Plasmonic Photocatalyst Ag@Ag(Br,I) *Chem. Euro. J.* **2010**, *16*, 10042-10047.
46. An, C.; Wang, J.; Qin, C.; Jiang, W.; Wang, S.; Li, Y.; Zhang, Q. Synthesis of Ag@AgBr/AgCl Heterostructured Nanocashews with Enhanced Photocatalytic Performance via Anion Exchange *J. Mater. Chem.* **2012**, *22*, 13153-13158.

47. Hu, H.; Jiao, Z.; Lu, G.; Ye, J.; Bi, Y. Enhanced Photocatalytic Properties of Biomimetic Ag/AgCl Heterostructures *RSC Adv.* **2014**, *4*, 31795-31798.
48. Dong, Q.; Jiao, Z.; Yu, H.; Ye, J.; Bi, Y. Facile Synthesis of Hollow Ag@AgBr Heterostructures with Highly Efficient Visible-Light Photocatalytic Properties *CrystEngComm* **2014**, *16*, 8317-8321.
49. An, C.; Wang, J.; Liu, J.; Wang, S.; Zhang, Q.-H. Plasmonic Enhancement of Photocatalysis over Ag Incorporated AgI Hollow Nanostructures *RSC Adv.* **2014**, *4*, 2409-2413.
50. An, C.; Wang, S.; Sun, Y.; Zhang, Q.; Zhang, J.; Wang, C.; Fang, J. Plasmonic Silver Incorporated Silver Halides for Efficient Photocatalysis *J. Mater. Chem. A* **2016**, *4*, 4336-4352.
51. Ma, X.; Dai, Y.; Lu, J.; Guo, M.; Huang, B. Tuning of the Surface-Exposing and Photocatalytic Activity for AgX (X = Cl and Br): A Theoretical Study *J. Phys. Chem. C* **2012**, *116*, 19372-19378.
52. Waddington, T. C. Lattice Energies and their Significance in Inorganic Chemistry *Adv. Inorg. Chem. Radiochem.* **1959**, *1*, 157-221.
53. Burley, G. Structure of Hexagonal Silver Iodide *J. Chem. Phys.* **1963**, *38*, 2807-2812.
54. Hull, S.; Keen, D. A.; Berastegui, P. Structural and Superionic Properties of Ag<sup>+</sup>-Rich Ternary Phases within the AgI-MI<sub>2</sub> Systems *J. Phys.: Condens. Matter* **2002**, *14*, 13579-13596.

55. Groznetskii, V. V.; Zhuravlev, V. D.; Kitaev, G. A.; Zhukova, L. V. Thermal Analysis of the AgCl–AgI and AgBr–AgI Systems *Russ. J. Inorg. Chem.* **1988**, *33*, 399-401.
56. Takahashi, H.; Tamaki, S.; Harada, S. Phase Equilibria of AgI–AgBr System *Solid State Ion.* **1984**, *14*, 107-112.
57. Adams, L. H.; Davis, B. L. Rapidly Running Transitions at High Pressure *Proc. Natl. Acad. Sci. U.S.A.* **1962**, *48*, 982-990.
58. Mellander, B. -E.; Bowling, J. E.; Baranowski, B. Phase Diagram of Silver Iodide in the Pressure Range 2.5–10 kbar and the Temperature Range 4–330° C *Phys. Scr.* **1980**, *22*, 541-544.
59. Yin, B.; Huang, X.; Mishra, R.; Sadtler, B. Compositionally Induced Twin Defects Control the Shape of Ternary Silver Halide Nanocrystals *Chem. Mater.* **2017**, *29*, 1014-1021.
60. Baetzold, R. C. Computations of Properties of Twin Planes in Silver Halide *J. Phys. Chem. Solids* **1996**, *57*, 627-634.
61. Yin, L. W.; Lee, S. T. Wurtzite-Twinning-Induced Growth of Three-Dimensional II–VI Ternary Alloyed Nanoarchitectures and their Tunable Band Gap Energy Properties *Nano Lett.* **2009**, *9*, 957-963.
62. Conesa-Boj, S.; Kriegner, D.; Han, X.-L.; Plissard, S.; Wallart, X.; Stangl, J.; Fontcubertai Morral, A.; Caroff, P. Gold-Free Ternary III–V Antimonide Nanowire Arrays on Silicon: Twin-Free Down to the First Bilayer *Nano Lett.* **2014**, *14*, 326-332.

63. Wang, F.; Buhro, W. E. Crystal-Phase Control by Solution–Solid–Solid Growth of II–VI Quantum Wires *Nano Lett.* **2016**, *16*, 889-894.
64. Wang, F.; Loomis, R. A.; Buhro, W. E. Spectroscopic Properties of Phase-Pure and Polytypic Colloidal Semiconductor Quantum Wires *ACS Nano* **2016**, *10*, 9745-9754.

## **Chapter 3**

# **Conversion of Lead Iodide Microcrystals to CH<sub>3</sub>NH<sub>3</sub>PbI<sub>3</sub> with Methylammonium Iodide Both in Solution and as Plasma**

## 3.1 Introduction

The crystallization of solution-processed, semiconductor films plays a critical role in controlling their optoelectronic quality.<sup>1-12</sup> For example, polycrystalline films of lead halides ( $\text{PbX}_2$  with  $\text{X} = \text{Cl}, \text{Br}, \text{or I}$ ) transform into the corresponding methylammonium lead halide ( $\text{CH}_3\text{NH}_3\text{PbX}_3$ ) perovskite semiconductor through the intercalation of  $\text{CH}_3\text{NH}_3^+$  and  $\text{X}^-$  ions into the  $\text{PbX}_2$  film.<sup>8-14</sup> This solid-state reaction occurs spontaneously when  $\text{PbX}_2$  films are exposed to either a solution or vapor containing  $\text{CH}_3\text{NH}_3\text{X}$ , which has been used to fabricate photovoltaics and light-emitting diodes with high quantum yields.<sup>11-17</sup> The performance of these devices is highly dependent on the composition and mesoscale morphology of the films.<sup>11-25</sup>

In this chapter, we synthesized lead iodide ( $\text{PbI}_2$ ) microcrystals and converted them to  $\text{CH}_3\text{NH}_3\text{PbI}_3$  perovskite with both methylammonium iodide (MAI) solution and a MAI plasma. High electric potential creates very small and uniform MAI plasma droplets during the process of acceleration. Therefore uniform transformation from  $\text{PbI}_2$  microcrystals to  $\text{CH}_3\text{NH}_3\text{PbI}_3$  perovskite can be achieved. The transformation reaction mechanisms in MAI solution and MAI plasma may be also different. These two methods may produce  $\text{CH}_3\text{NH}_3\text{PbI}_3$  with different morphologies which are crucial to the performance of optoelectronic device. Since the orientations of the crystal also affect the performance of the material, we want to determine the crystallographic relationship between parental  $\text{PbI}_2$  crystal and the converted  $\text{CH}_3\text{NH}_3\text{PbI}_3$  in both solution and plasma reaction conditions.

Several studies have used electron microscopy, x-ray diffraction, and optical spectroscopy to correlate the morphology and optical properties of  $\text{CH}_3\text{NH}_3\text{PbX}_3$  films with growth conditions, such the reaction temperature, growth time, and the  $\text{CH}_3\text{NH}_3\text{X}$  concentration.<sup>4-12</sup> However, solution-processed, semiconductor films often possess heterogeneity in composition,



crystallinity, defect concentration, and grain size. Thus, techniques that can spatially and temporally map properties such as fluorescence brightness, excited charge carrier lifetimes, photocurrent collection, and open-circuit potential are critical to gain further insight into how local structure and composition affect performance in optoelectronic devices. These techniques include photocurrent microscopy,<sup>25</sup> transient absorption microscopy,<sup>26-28</sup> and fluorescence microscopy.<sup>29-41</sup>

Fluorescence microscopy provides the ability to spatially map charge carrier dynamics in both polycrystalline films and nanoscale crystals of  $\text{CH}_3\text{NH}_3\text{PbX}_3$ .<sup>29-41</sup> The emission intensity and wavelength in  $\text{CH}_3\text{NH}_3\text{PbX}_3$  crystals are optical signatures that can be linked with variations in composition, crystallinity, defect concentration, and the degree of quantum confinement. For instance, the fluorescence brightness in polycrystalline films of  $\text{CH}_3\text{NH}_3\text{PbI}_3$  is weaker at grain boundaries,<sup>30</sup> and the emission wavelength red-shifts with halide composition going from  $\text{X} = \text{Cl}$  to  $\text{Br}$  to  $\text{I}$ .<sup>31,39</sup> Fluorescence microscopy has also been used to observe solid-state transformations in lead-halide perovskite microcrystals in situ by monitoring changes in either the fluorescence intensity or the emission wavelength.<sup>9,39</sup> For example, Tachikawa and coworkers used the shift in emission wavelength to watch ion exchange between a  $\text{CH}_3\text{NH}_3\text{PbBr}_3$  microcrystal ( $\sim 8 \mu\text{m}$ ) and  $\text{CH}_3\text{NH}_3\text{I}$  in solution.<sup>39</sup> In this chapter fluorescence microscopy was used to observe the transformation of micrometer-sized  $\text{PbI}_2$  single crystals to  $\text{CH}_3\text{NH}_3\text{PbI}_3$  perovskite in situ in order to gain insights into this important solid-state reaction.

## 3.2 Experimental Details

### 3.2.1 Materials and Chemical Synthesis

*Material:* ethylene glycol ( $\geq 99\%$ ), potassium iodide (KI,  $\geq 99\%$ ), 1,4-butanediol (99%), lead (II) nitrate ( $\geq 99\%$ ), 2-propanol (IPA, 99.5%), methylamine solution ( $\text{CH}_3\text{NH}_2$ , 33 wt. % in absolute ethanol), lead (II) acetate trihydrate ( $\text{Pb}(\text{CH}_3\text{CO}_2)_2 \cdot 3\text{H}_2\text{O}$ , ACS  $\geq 99\%$ ), acetic acid (ACS  $\geq 99.7\%$ ), polyvinylpyrrolidone (PVP, average molecular weight 40,000) and lead iodide ( $\text{PbI}_2$ ,  $\geq 99\%$ ) were purchased from Sigma-Aldrich Inc. hydriodic acid (57% weight percentage in aqueous solution with stabilizer) was purchased from VWR International Inc. All chemicals were used as received.

*Synthesis of methylammonium iodide ( $\text{CH}_3\text{NH}_3\text{I}$ ):* Methylammonium iodide (MAI) was synthesized following a previously reported procedure.<sup>42</sup> First, 24 mL of a  $\text{CH}_3\text{NH}_2$  solution (33 wt. % in ethanol) was reacted with 10 mL of HI (57%) in 100 mL ethanol. After the reaction, a rotary evaporator was used to remove ethanol and isolate the resulting MAI powder. The white MAI powder was collected and further dried in a vacuum oven at 60 °C overnight. The MAI powder was stored in a glovebox for future use.

*Synthesis of lead iodide ( $\text{PbI}_2$ ) microcrystals:* 0.012 g (about 0.07 mmol) of potassium iodide was dissolved into 2.5 mL ethylene glycol. 0.023 g (about 0.07 mmol) of lead nitrate was dissolved to 2.5 mL of 1,4-butanediol. Then the ethylene glycol solution was mixed with the 1,4-butanediol solution under vigorous stirring at room temperature to obtain the  $\text{PbI}_2$  microcrystal precipitate.

*Growing single lead iodide microcrystal on coverslips:* To grow single lead iodide microcrystal on glass coverslips, we followed a previous report.<sup>9</sup> In a typical reaction, 0.5 g of  $\text{PbI}_2$  was

dissolved into pure water. The water was heated to about 90 °C in oil bath to dissolve PbI<sub>2</sub> with stirring. After PbI<sub>2</sub> was dissolved, the pH value of solution was adjusted to a value under 4.0 using acetic acid. Coverslips was cleaned by sonicating in acetone for 15 min and dried by N<sub>2</sub> gas flow. Then the coverslips were submerged into the PbI<sub>2</sub> solution and heated together to 90 °C. After the temperature was stable, the PbI<sub>2</sub> solution was taken out of oil bath and cooled to room temperature in air. With the temperature of the solution decreasing, over-saturated PbI<sub>2</sub> would precipitate from solution, and nucleation and growth of PbI<sub>2</sub> occurs on the surface of coverslips. After the solution cooled to room temperature (about 1 hour), the coverslips were taken out of the solution and washed with 2-propanol and dried with N<sub>2</sub> gas.

*Synthesis of lead iodide nanocrystals:* The procedures for synthesizing PbI<sub>2</sub> nanocrystals were adapted from a previous report.<sup>43</sup> In a typical reaction for the lead precursor, 3 mmol of lead acetate trihydrate was added and dissolved into 9 mL of pure water (18.2 MΩ·cm) and 1 mL acetic acid with stirring. Then approximately 0.06 g of PVP (40,000 MW) was dissolved into the solution. For the iodide precursor, 2.5 mmol of KI was dissolved into 5 mL pure water. The iodide precursor was then dropped into lead precursor under vigorous stirring. (At this point, PbI<sub>2</sub> crystals were produced, and the color of the solution turned to yellow.) About 15 mL pure water was added to the mixture and strong stirring was continued for 10 more minutes. Then the pH value of the mixture was monitored using a pH meter, and acetic acid was used to adjust the pH value to about 3. After that, the mixture solution was transferred to an autoclave and the autoclave was heated at 100 °C for 8 hours. The autoclave was cooled to room temperature in a fume hood before opening it.

*Washing procedure for PbI<sub>2</sub> nanocrystals:* To wash the nanocrystals, both pure water and ethanol were used. After reaction for 8 hours in the autoclave, PbI<sub>2</sub> nanocrystals were

precipitated to the bottom of the container. First, all the supernatant was removed from the container and the  $\text{PbI}_2$  precipitate on the bottom was transferred to 2 centrifuge tubes. Then pure water was added to each of the tubes and mixed uniformly. Both tubes were centrifuged at 8,000 rpm for 5 min, and all the supernatant was removed from the tubes. This finished the washing cycle with pure water. Then a washing cycle with ethanol was done. For this, ethanol was added to each centrifuge tube and sonicated until the yellow precipitate was suspending in solution. Then tubes were centrifuged at 8,000 rpm for 5 min and all the supernatant was removed. This concluded the ethanol washing cycle. After the ethanol washing cycle one more water washing cycle was performed before storing the  $\text{PbI}_2$  nanocrystals in ethanol for future use.

### **3.2.2 Details of Conversion from $\text{PbI}_2$ Microcrystals to $\text{CH}_3\text{NH}_3\text{PbI}_3$**

*Conversion from  $\text{PbI}_2$  microcrystal to lead perovskite:* The conversion from  $\text{PbI}_2$  microcrystal to lead perovskite was performed on indium doped tin oxide (ITO) substrates so that SEM could be used to image perovskite crystal after reaction.  $\text{PbI}_2$  microcrystals were drop casted onto a ITO substrate. Then the ITO substrate was immersed into various concentration of methylammonium iodide solution in 2-propanol (5 mg/mL, 8 mg/mL, 10 mg/mL, 12 mg/mL and 20 mg/mL) for different period of times (5 min, 10 min or 20 min).

*Conversion of  $\text{PbI}_2$  microcrystal to lead perovskite with high voltage electrospray of plasma methylammonium iodide:* Plasma methylammonium iodide (MAI) was achieved by applying a high potential between the nozzle, where MAI solution flowed, and the grounded substrate, where the sample stayed. A high potential was achieved by a Keithley DC power supply.

Charged droplets of MAI under potential would gain momentum and accelerate toward the ground substrate where it would react with the  $\text{PbI}_2$  microcrystals. Under the high applied potential, the drops of MAI solution would form a cone shape rather than sphere as shown in **Figure 3.3**. In a typical reaction,  $\text{PbI}_2$  microcrystals were spin coated onto an ITO substrate (3000 rpm for 20s). The concentration of MAI solution in 2-propanol was 12 mg/mL. The injection rate through the nozzle was 1  $\mu\text{L}/\text{min}$ . After the ITO substrate was grounded to start electro spray, about 6 kV potential was applied between the nozzle and the ITO substrate. After the electro spray, the ITO substrate was annealed at 100 °C for 5 min.

### 3.2.3 Details of Characterization

Scanning electron microscopy (SEM) images were recorded with a JEOL 7001LVF field-emission scanning electron microscope operated at an acceleration voltage of 10 keV.  $\text{PbI}_2$  microcrystals were drop cast onto ITO substrates in order to image under SEM. Conversion of  $\text{PbI}_2$  microcrystals to lead perovskite crystal was also done on an ITO substrate. Therefore, SEM can be done directly after the conversion.

To prepare samples for x-ray diffraction (XRD), several drops of the washed nanocrystals (dispersed in ethanol) were drop-cast onto a zero-background, silicon diffraction plate (MTI Corporation). The solution was allowed to dry on the diffraction plate in air. For the XRD measurement after conversion from  $\text{PbI}_2$  to perovskite, the diffraction plate with  $\text{PbI}_2$  microcrystals was immersed in various concentration of MAI solution in 2-propanol for different period of time before taken out and rinsed with 2-propanol. XRD patterns were then collected

using a Bruker D8 Advance X-ray Diffractometer (Cu K $\alpha$  = 0.15418 nm). The step size for the XRD measurements was 0.02° in 2 $\theta$ , and the scan rate was 0.5 s per step.

Transmission electron microscopy (TEM) was performed using a JEOL 2000FX transmission electron microscope with an acceleration voltage of 200 kV using a LaB6 filament as the electron source. After washing, a drop of the nanocrystal solution was drop-cast onto a TEM grid (Ted Pella, Inc #01811). Then the TEM grid was under gold sputtering for 120s. Electron diffraction patterns were obtained using an aperture to select individual single PbI<sub>2</sub> nanocrystal. The camera length was 150 cm. For imaging lead perovskite nanocrystal after conversion reaction, the TEM grid with PbI<sub>2</sub> nanocrystals was immersed into MAI solution with various concentrations for 10 min before taken out and rinsed with 2-propanol.

*Monitoring single microcrystal conversion with fluorescence microscopy:* Fluorescence imaging was carried out using a Nikon N-STORM microscopy system consisting of a Nikon TiE motorized inverted optical microscope and a Nikon CFI-6-APO TIRF 100 $\times$  oil-immersion objective lens with a numerical aperture of 1.49 and a working distance of 210  $\mu$ m. The microscope also contains optics for imaging using differential interference contrast (DIC), which was used for focusing of PbI<sub>2</sub> microcrystals on the coverslip. The Nikon Perfect Focus 3 system was used to maintain focal stability during imaging. As shown in **Figure 3.5**, the PbI<sub>2</sub> microcrystals on the coverslip were photoexcited through the objective using filtered light from a white light-emitting diode (LED). A filter cube was used (Chroma, set #TRF49910) with an excitation filter that had 90% transmission for green light of wavelengths between 550 and 570 nm. The emission filter had 90% transmission between 570 and 750 nm. An Andor iXon 897 electron-multiplying CCD with single photon sensitivity (512  $\times$  512, 16  $\mu$ m pixels, 90% quantum efficiency) was used to detect the fluorescent signals. The time resolution of the

EMCCD camera is 0.02 s, which means the camera will take 50 measurements in 1 s. Images were collected with an exposure time of 2 ms.

## 3.3 Results and Discussion

### 3.3.1 Synthesis of $\text{PbI}_2$ Microcrystals and Their Conversion to $\text{CH}_3\text{NH}_3\text{PbI}_3$

Lead iodide microcrystals were synthesized using a procedure adapted from our previous synthesis method of ternary silver halide nanocrystals.<sup>1</sup> Different from previous synthesis procedure, PVP surfactant was not used in the synthesis of microcrystals. Therefore size of  $\text{PbI}_2$  crystals was allowed to grow bigger. (More details of this  $\text{PbI}_2$  microcrystal synthesis are given in **Experimental Details 3.2.1**.) **Figure 3.1 a** shows a SEM image of  $\text{PbI}_2$  microcrystals on an ITO substrate.  $\text{PbI}_2$  single crystals can be achieved using this synthesis method, and the typical size of a single  $\text{PbI}_2$  microcrystal is about 5 to 10  $\mu\text{m}$  in diameter. The XRD measurement of the as-synthesized microcrystals is shown in **Figure 3.2** (bottom blue pattern). Comparing with the standard PDF card of  $\text{PbI}_2$  (00-007-0235), it confirmed that the as-synthesized microcrystals were indeed lead iodide.

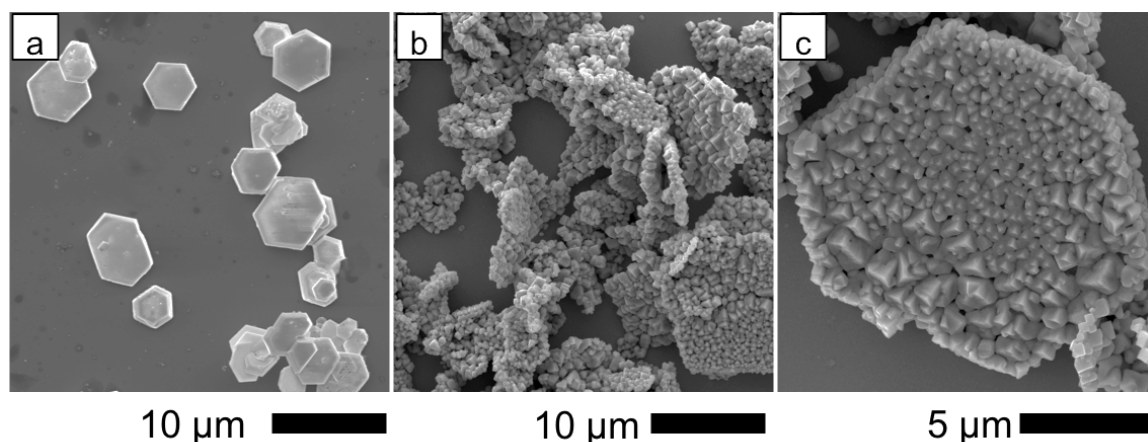


**Figure 3.1** (a) SEM images of  $\text{PbI}_2$  microcrystals and (b) images after  $\text{PbI}_2$  microcrystals after reaction with methylammonium iodide in 2-propanol (5 mg/mL) for 5 min. (c) shows a higher magnification of a single microcrystal after conversion.

The conversion from  $\text{PbI}_2$  microcrystals to  $\text{CH}_3\text{NH}_3\text{PbI}_3$  was performed on ITO substrates. In a typical reaction, the ITO substrate with  $\text{PbI}_2$  microcrystal was submerged into a methylammonium iodide (MAI) solution in 2-propanol with various concentrations for different times. **Figure 3.1 b** shows a SEM image of  $\text{PbI}_2$  microcrystals after reacting with 5 mg/mL MAI solution for 5 min. A higher magnification of a single microcrystal after the conversion is given in **Figure 3.1 c**. Comparing the images in **Figure 3.1 a** with **b** and **c**, the morphology of  $\text{PbI}_2$  microcrystals changed after reacting with MAI in solution. Clearly there are multiple new crystalline domains formed after the conversion, indicating the single  $\text{PbI}_2$  microcrystal became polycrystalline. XRD measurements were done after the conversion reaction. The results are shown in **Figure 3.2** (red and black patterns). **Figure 3.2** shows that a new crystal structure appears after the conversion reaction and it matched the calculated XRD pattern of  $\text{CH}_3\text{NH}_3\text{PbI}_3$  shown as black lines on the top.<sup>44</sup> Comparing the three XRD patterns in **Figure 3.2**, the peak intensities of  $\text{PbI}_2$  decreases with increasing MAI concentration for the same reaction time. The  $\text{PbI}_2$  peaks disappear eventually (20 mg/mL MAI for 10 min) which suggests that  $\text{PbI}_2$  microcrystals are completely transformed to  $\text{CH}_3\text{NH}_3\text{PbI}_3$ .



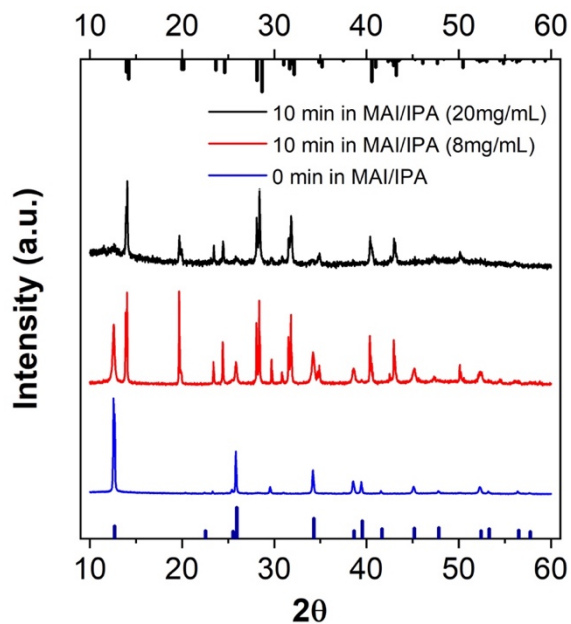


**Figure 3.2** XRD of  $\text{PbI}_2$  microcrystals and 10 min reaction in both 8 mg/mL and 20 mg/mL of methylammonium iodide in a 2-propanol solution. Standard PDF card of  $\text{PbI}_2$  is given at the bottom (00-007-0235). Calculated tetragonal  $\text{CH}_3\text{NH}_3\text{PbI}_3$  powder XRD pattern based on published experimental data is given at the top (black lines).<sup>44</sup>

Shown in **Figure 3.1 c**, the newly formed crystal domains have certain crystalline relationship with their parental crystal,  $\text{PbI}_2$ , because the newly formed domains orient themselves in a topotactic manner relative to the crystal orientation of  $\text{PbI}_2$  microcrystal. Cahen and Hodes studied the structural relationship for the conversion of single crystalline  $\text{PbI}_2$  microcrystals to  $\text{CH}_3\text{NH}_3\text{PbI}_3$  in solution.<sup>9</sup> In their study, they used SEM to measure the angle between the edges of the newly formed  $\text{CH}_3\text{NH}_3\text{PbI}_3$  grains and the (001) facet of the original  $\text{PbI}_2$  microcrystal. Through the characteristic angle of  $54.8^\circ$  between (002) and (202) crystal facets of  $\text{CH}_3\text{NH}_3\text{PbI}_3$  and with the help of change in peak intensity of XRD, they confirmed that (202) planes of  $\text{CH}_3\text{NH}_3\text{PbI}_3$  perovskite are formed parallel to the (001) planes of the hexagonal  $\text{PbI}_2$ , and  $\langle 100 \rangle$  is the growth direction of the newly formed  $\text{CH}_3\text{NH}_3\text{PbI}_3$ .<sup>9</sup> These findings are consistent with our observations.

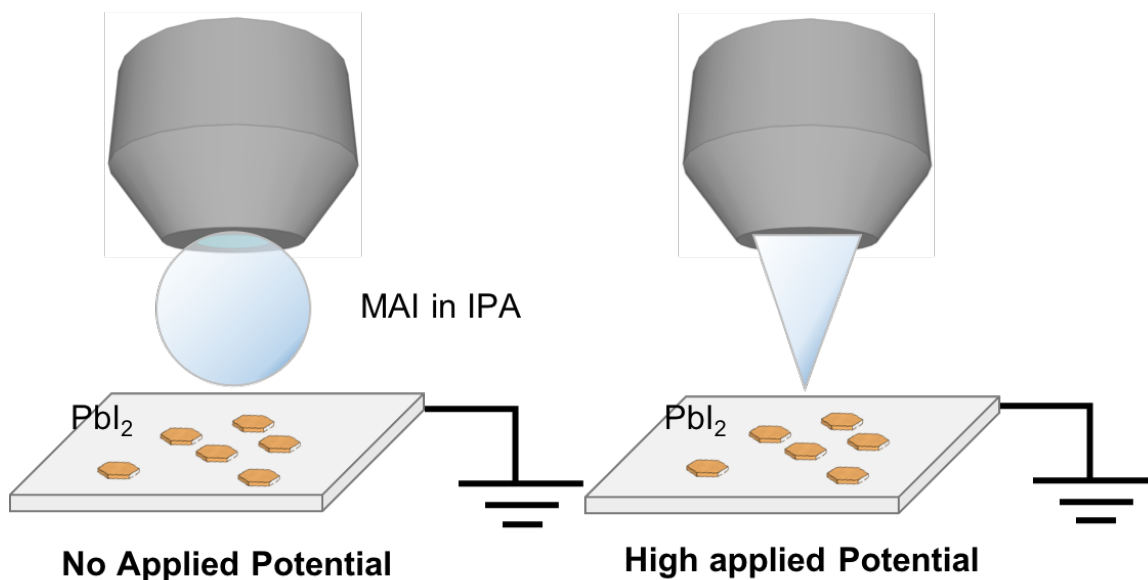


**Figure 3.3** Schematic showing the electro spray configuration used to transform  $\text{PbI}_2$  microcrystals to  $\text{CH}_3\text{NH}_3\text{PbI}_3$ . MAI droplet (several millimeter in diameter) without applied electric potential is shown on the left. On the right shows the situation with a high applied potential.  $\text{PbI}_2$  microcrystals are deposited on the grounded ITO substrate.

### Conversion of $\text{PbI}_2$ microcrystals to $\text{CH}_3\text{NH}_3\text{PbI}_3$ with MAI plasma.

The schematic of the experiment is given in **Figure 3.3**. The idea of the experiment is to ionize MAI droplets and under high electric potential drive the charged MAI droplets to strike and react with  $\text{PbI}_2$  microcrystal on the grounded ITO substrate. (More details of experiment can be found in **Experimental Details 3.2.2**.) **Figure 3.4 a** and **b** show the SEM images of  $\text{PbI}_2$  microcrystals after the electro spray for 15 min. Compare **Figure 3.1 b** and **Figure 3.4 a**, there are no clear crystalline domains after conversion by electro spray, although the surface of microcrystal became a lot rougher after electro spray indicating the successful conversion. However, when the  $\text{PbI}_2$  microcrystals react with MAI solution in 2-propanol, clear crystalline domains of  $\text{CH}_3\text{NH}_3\text{PbI}_3$  were formed on the surface. Similar morphology was also observed by Cahen and Hodes.<sup>9</sup> In their study, a surface covered with irregularly shaped grains was observed

after the  $\text{PbI}_2$  microcrystals reacted with MAI vapor instead of a MAI solution. Similar to the reaction with MAI in solution, single  $\text{PbI}_2$  microcrystals also become polycrystalline after electro spray conversion with MAI plasma based on SEM observation and XRD measurement. XRD confirms that with prolonged time (typically, more than 30 min)  $\text{PbI}_2$  microcrystals can be completely transformed to  $\text{CH}_3\text{NH}_3\text{PbI}_3$ . (XRD results are not shown here.) However, as shown in **Figure 3.4 b**, excess MAI can be observed on the surface of microcrystal after conversion. XRD measurements also confirms the exist of excess MAI on the substrate.

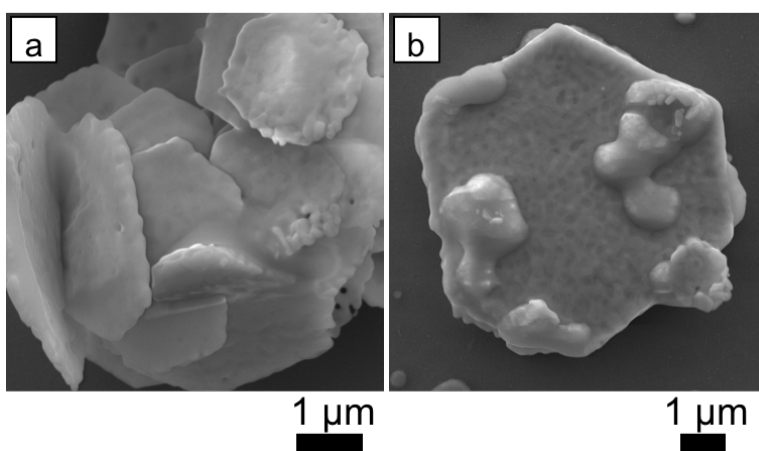


**Figure 3.4** SEM images of  $\text{PbI}_2$  microcrystals after methylammonium iodide plasma electro spray for 15 min

### 3.3.2 In situ Observation of the Conversion from Single $\text{PbI}_2$ Microcrystals to $\text{CH}_3\text{NH}_3\text{PbI}_3$ with Fluorescence Microscopy

In addition to the ex situ studies mentioned above, we also performed the in situ observation of the conversion from single  $\text{PbI}_2$  microcrystals to  $\text{CH}_3\text{NH}_3\text{PbI}_3$  with fluorescence microscopy. Being able to observe the transformation as it happens offers more insights into the transformation, such as where and when the transformation starts and how it progresses, that are otherwise lost in the ex situ measurements. **Figure 3.5** shows the experimental configuration

used to observe the transformation of single  $\text{PbI}_2$  microcrystals to  $\text{CH}_3\text{NH}_3\text{PbI}_3$ . The bandgap of  $\text{PbI}_2$  microcrystal is about 2.5 eV which is about 500 nm in wavelength.<sup>45</sup> Therefore, excitation with green light (550 nm to 570 nm) cannot excite electrons in  $\text{PbI}_2$  microcrystals from the valence band to the conduction band. However, after reaction with MAI, the bandgap of the  $\text{CH}_3\text{NH}_3\text{PbI}_3$  narrows to 1.5 eV (830 nm in wavelength), which can be excited by the green light.<sup>4-9,35,46</sup> Therefore, using fluorescence microscopy, in situ observation of the conversion from a single  $\text{PbI}_2$  microcrystal to  $\text{CH}_3\text{NH}_3\text{PbI}_3$  can be achieved.

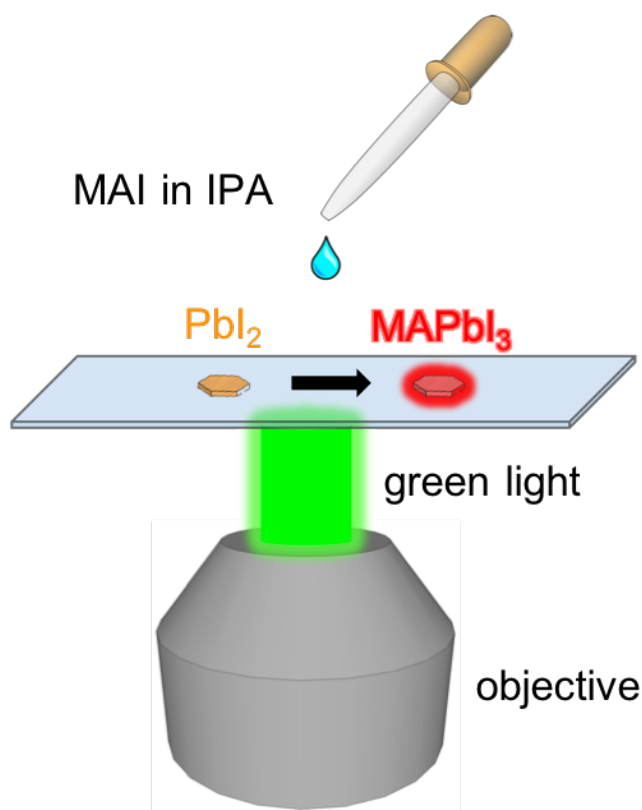


**Figure 3.5** Schematic showing the experimental configuration used to observe the transformation of single  $\text{PbI}_2$  microcrystals to  $\text{CH}_3\text{NH}_3\text{PbI}_3$ . Upon excitation with green light, the initial  $\text{PbI}_2$  microcrystals are non-fluorescent while the product  $\text{CH}_3\text{NH}_3\text{PbI}_3$  is highly fluorescent.

**Figure 3.6 b-e** shows several selected frames from the videos recorded from the fluorescence microscopy observations. The red color of the bright spot is artificial, not the actual color of the fluorescence emission. During the observation, it was hard to determine exactly when the MAI solution came to contact with  $\text{PbI}_2$  microcrystals. Thus, we used the recording time when the first fluorescent event was observed as the starting time, 0.0 s. **Figure 3.6 a** and **f** are optical microscope images of the same location before and after the conversion reaction.

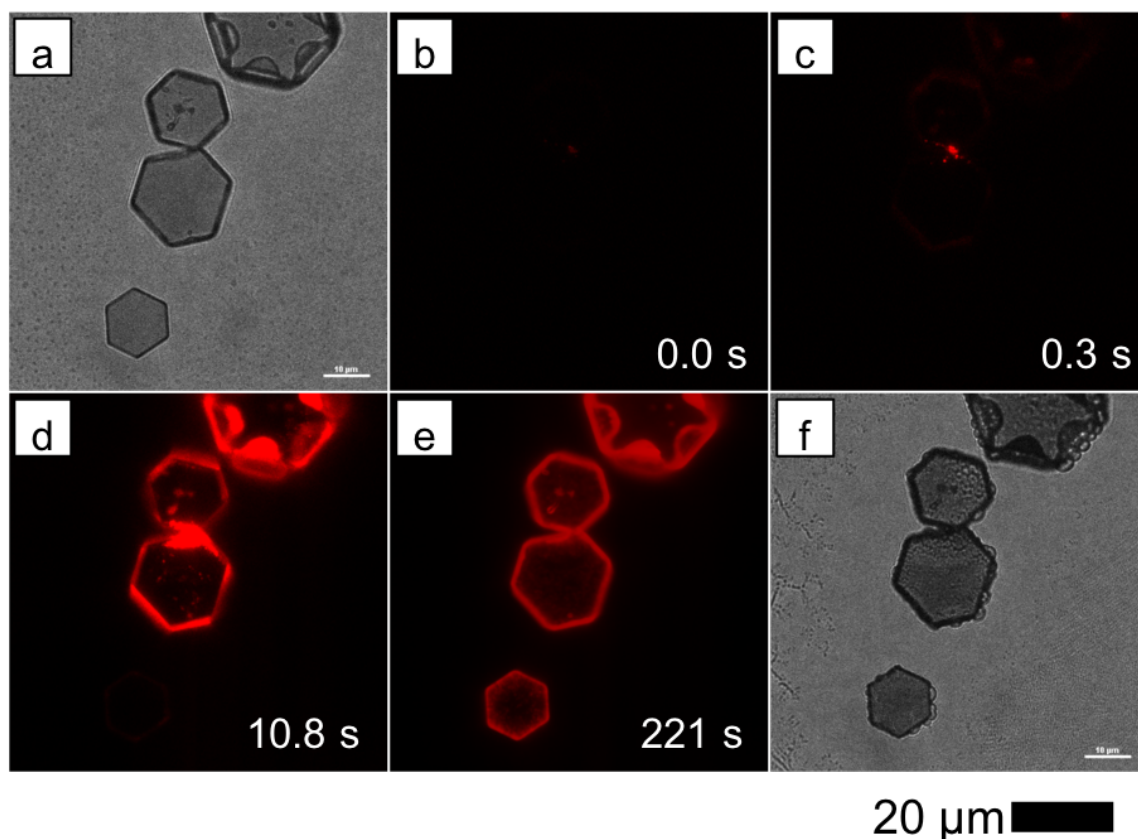


**Figure 3.6** Imaging the conversion of  $\text{PbI}_2$  microcrystals into  $\text{CH}_3\text{NH}_3\text{PbI}_3$ . **(a)** optical microscope image of the exact location before the conversion. **(b-e)** Selected frames from a video recording of the fluorescence intensity under excitation with green light. The first frame (0.0 sec) corresponds to when the first fluorescent spot appears. **(f)** image of the same  $\text{PbI}_2$  microcrystals after the conversion. The 20  $\mu\text{m}$  scale bar applies to all images, **(a** through **f)**.

From **Figure 3.6** there are several things that can be gathered from the in situ study of this transformation. First of all, it shows that the first locations of the transformation were locations of surface defects, such as step edges from the missing or extra layers of material on surface, and the edges of the single  $\text{PbI}_2$  microcrystals, comparing **Figure 3.6 c** and **e**. Secondly, different  $\text{PbI}_2$  microcrystals started the conversion at different time. Comparing **Figure 3.6 c** and **d**, it shows that it took much longer time for the single  $\text{PbI}_2$  microcrystal on the bottom left corner to start transformation than the rest of the microcrystals. We believe this observation relates to the defects on the surface of  $\text{PbI}_2$  microcrystals, such as dislocations, vacancies and step edges created by missing or extra layers of material on surfaces which can act as preferential reaction sites. Also, the locations of these defects vary from one microcrystal to another. These defects may have different effects on starting this solid-state conversion. Therefore, this observation implies that certain defects would trigger and facilitate the conversion.

Thirdly, it took a relatively long time to convert  $\text{PbI}_2$  crystals with micrometer dimensions to  $\text{CH}_3\text{NH}_3\text{PbI}_3$ . We observed that the conversion reaction took more than 5 min using fluorescence microscopy. At the time that we stopped the recording, the conversion reaction was still going. The XRD measurement of **Figure 3.2** suggests that the transformation is still not complete at this point. This long conversion time is also observed by other studies of conversion of  $\text{PbI}_2$  with micrometer scale.<sup>4-5</sup>

Lastly, comparing **Figure 3.6 a** and **f** optical images, the surface roughness of  $\text{PbI}_2$  microcrystals increased dramatically after the conversion reaction. This observation is also consistent with the SEM images shown in **Figure 3.1**. Since the  $\text{PbI}_2$  was micrometer in size, there are multiple nucleation sites during the conversion as evidenced by both the in situ observation with fluorescence microscopy and ex situ SEM. However, the observed

transformation of microcrystals is the results of many nucleation and growth events occurring simultaneously. As a result, information related to transformation kinetics of each individual nuclei is lost or blocked during the averaging process. If we can confine the observation of the transformation to one nucleation event at a time, it would simplify the studied system and more fundamentals of this reaction could be shown. Therefore, in order to gain more insights to this transformation reaction, nanoscale  $\text{PbI}_2$  crystals are needed, and it is desirable to study single-crystal to single-crystal transformation.

### 3.3.3 Synthesis of $\text{PbI}_2$ Nanocrystals and Conversion to $\text{CH}_3\text{NH}_3\text{PbI}_3$

Based on the previous observations and discussion, nanoscale  $\text{PbI}_2$  crystals are desirable, which becomes the focus of the next study. A hydrothermal method was used to synthesize  $\text{PbI}_2$  nanocrystals. (More details of synthesis and following washing procedure can be found in **Experimental Details 3.2.1.**) **Figure 3.7** shows a TEM image of a single  $\text{PbI}_2$  nanocrystal after gold sputtering to stabilize the nanocrystal under the electron beam. Compared with the microscale crystal in **Figure 3.1**, the size of  $\text{PbI}_2$  using hydrothermal synthesis method was reduced to several hundred nanometers. Even though the thickness of the  $\text{PbI}_2$  nanocrystal cannot be determined by TEM, it is believed to be well below 50 nm as the electron beam can penetrate the particle. An electron diffraction pattern of this single  $\text{PbI}_2$  nanocrystal was measured (inset figure of **Figure 3.7**), which indicated that this nanocrystal was  $\text{PbI}_2$  and also the top and bottom planes of the prism were the (001) facets of  $\text{PbI}_2$ .

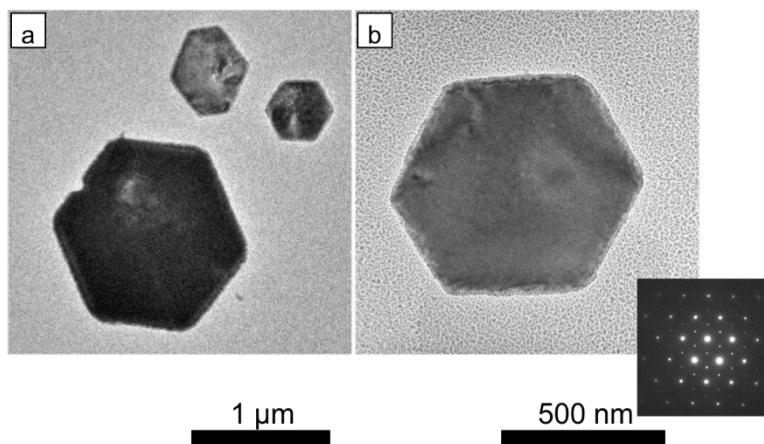


**Figure 3.7** TEM images of single  $\text{PbI}_2$  nanocrystals. **(b)** is a single  $\text{PbI}_2$  nanocrystal with gold sputtering and its corresponding single crystal electron diffraction pattern (inset).

TEM images of  $\text{PbI}_2$  nanocrystals after reaction with different concentration of MAI in 2-propanol are shown in **Figure 3.8**. (Details of preparation of TEM samples were given in **Experimental Details 3.2.3**.) From both TEM images it shows that there is partial dissolution of  $\text{PbI}_2$  nanocrystal during the conversion reaction, which was also observed in previous studies.<sup>4-8</sup> **Figure 3.8 a** is a TEM image after the reaction with 6 mg/mL MAI for 10 min and it shows that the locations of dissolution of  $\text{PbI}_2$  nanocrystal seem to be random. It could happen at both the edges and the middle of the  $\text{PbI}_2$  nanocrystal. However, **Figure 3.8 b** shows reaction with 20 mg/mL MAI for 10 min and  $\text{PbI}_2$  nanocrystals shows a hollowed ring around the circumference after the conversion to  $\text{CH}_3\text{NH}_3\text{PbI}_3$ . Comparing **Figure 3.8 a** and **b**, it seems that this difference of morphology after conversion related to the concentration of MAI solution used in the reaction. For future studies, MAI solution with much lower concentrations can be tried. This could prove whether high concentration MAI is responsible for the partial dissolution of  $\text{PbI}_2$  during conversion. Though I am concerned that it would take a long time for complete



conversion at lower MAI concentrations. Also more conversion reactions at 6 mg/mL and 20 mg/mL are needed to make sure the results are repeatable and consistent.

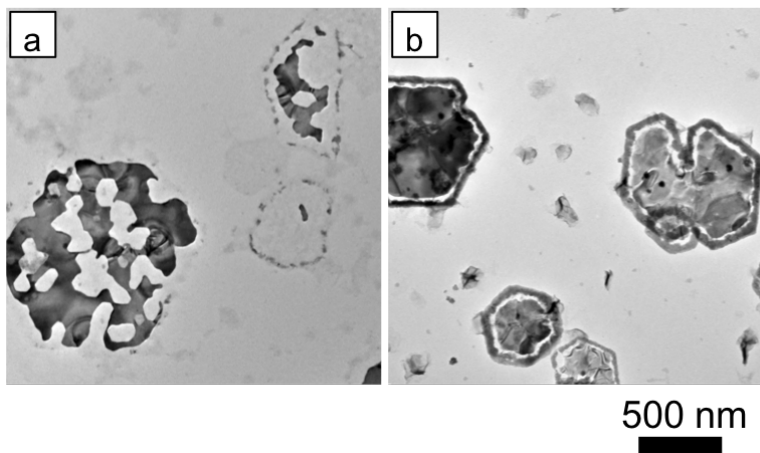


**Figure 3.8** TEM images of  $\text{PbI}_2$  nanocrystals after reaction with different concentration of methylammonium iodide in 2-propanol **(a)** 6 mg/mL and **(b)** 20 mg/mL for 10 min. The 500 nm scale bar is shared by both **(a)** and **(b)**.

### 3.4 Conclusions

Single  $\text{PbI}_2$  crystals with both micrometer and nanometer scales are successfully synthesized and their conversion to  $\text{CH}_3\text{NH}_3\text{PbI}_3$  perovskite are studied using both ex situ and in situ methods. For  $\text{PbI}_2$  microcrystals, multiple crystalline  $\text{CH}_3\text{NH}_3\text{PbI}_3$  domains are formed on the surface of  $\text{PbI}_2$  when reacted with MAI solution. The (202) planes of  $\text{CH}_3\text{NH}_3\text{PbI}_3$  perovskite are formed parallel to the (001) planes of the hexagonal  $\text{PbI}_2$  microcrystal.<sup>9</sup> However, when reacted with a MAI plasma formed by electrospray, no clear domains of crystalline  $\text{CH}_3\text{NH}_3\text{PbI}_3$  are observed on the surface of  $\text{PbI}_2$  microcrystals. So, there is no clear crystallography relation between  $\text{PbI}_2$  and  $\text{CH}_3\text{NH}_3\text{PbI}_3$ . Also, we observe single  $\text{PbI}_2$  microcrystals transform to  $\text{CH}_3\text{NH}_3\text{PbI}_3$  perovskite in situ with fluorescence microscopy. It shows that the conversion starts

at the edges of  $\text{PbI}_2$  microcrystals and defects such as locations of missing or extra layers of crystal on surfaces. This information is lost in the ex situ measurement of this conversion. For  $\text{PbI}_2$  nanocrystals, the lateral size of  $\text{PbI}_2$  is reduced to several hundred nanometers. Partial dissolution of  $\text{PbI}_2$  nanocrystal is observed after the conversion to  $\text{CH}_3\text{NH}_3\text{PbI}_3$  perovskite. The morphologies of the  $\text{CH}_3\text{NH}_3\text{PbI}_3$  after conversion are different and it seems to relate to MAI concentrations used in the reaction.

Unfortunately, even though  $\text{PbI}_2$  nanocrystals with the size of several hundred nanometers are achieved, it is still too large of a crystal to achieve single crystal to single crystal transformation which could reveal more fundamentals of the reaction that are otherwise lost when multiple nucleation and growth events occur simultaneously. By studying the reactivity and photophysics of single nanocrystals, one can observe behavior that is obscured in the ensemble average.<sup>36,47-55</sup> Therefore, in the next chapter we further reduced the size of the lead halide nanocrystals and studied the transformation from single nanocrystal to single nanocrystal.

### **3.5 Acknowledgements**

I would like to give special thanks to Dr. Pratim Biswas and Dr. Shaline Kavadiya here for allowing me use their high electric potential plasma set ups to make the conversion reaction. Dr. Shaline Kavadiya also gave a lot of assistance during the experiments. I would also like to thank Craig Laing who was my undergraduate mentee in our lab and he helped me in synthesis of  $\text{PbI}_2$  microcrystal. Our technicians, Dr. Huafnag Li and Dr. Tyrone Daulton, also assisted me with the TEM imaging.

## 3.6 References

1. Baikie, T.; Fang, Y.; Kadro, J. M.; Schreyer, M.; Wei, F.; Mhaisalkar, S. G.; Graetzel, M.; White, T. J., Synthesis and crystal chemistry of the hybrid perovskite (CH<sub>3</sub>NH<sub>3</sub>)PbI<sub>3</sub> for solid-state sensitised solar cell applications, *J. Mater. Chem. A* **2013**, *1*, 5628-5641.
2. Stoumpos, C. C.; Malliakas, C. D.; Kanatzidis, M. G., Semiconducting tin and lead iodide perovskites with organic cations: phase transitions, high mobilities, and near-infrared photoluminescent properties, *Inorg. Chem.* **2013**, *52*, 9019-9038.
3. Choi, J. J.; Yang, X.; Norman, Z. M.; Billinge, S. J. L.; Owen, J. S., Structure of methylammonium lead iodide within mesoporous titanium dioxide: active material in high-performance perovskite solar cells, *Nano Lett.* **2014**, *14*, 127-133.
4. Tidhar, Y.; Edri, E.; Weissman, H.; Zohar, D.; Hodes, G.; Cahen, D.; Rybtchinski, B.; Kirmayer, S., Crystallization of methyl ammonium lead halide perovskites: implications for photovoltaic applications, *J. Am. Chem. Soc.* **2014**, *136*, 13249-13256.
5. Grancini, G.; Marras, S.; Prato, M.; Giannini, C.; Quarti, C.; De Angelis, F.; De Bastiani, M.; Eperon, G. E.; Snaith, H. J.; Manna, L.; Petrozza, A., The impact of the crystallization processes on the structural and optical properties of hybrid perovskite films for photovoltaics, *J. Phys. Chem. Lett.* **2014**, *5*, 3836-3842.
6. Zhou, Y.; Game, O. S.; Pang, S.; Padture, N. P., Microstructures of organometal trihalide perovskites for solar cells: their evolution from solutions and characterization, *J. Phys. Chem. Lett.* **2015**, *6*, 4827-4839.

7. Morrell, M. V.; He, X.; Luo, G.; Thind, A. S.; White, T. A.; Hachtel, J. A.; Borisevich, A. Y.; Idrobo, J.-C.; Mishra, R.; Xing, Y., Significantly enhanced emission stability of CsPbBr<sub>3</sub> nanocrystals via chemically induced fusion growth for optoelectronic devices, *ACS Appl. Nano Mater.* **2018**, *1*, 6091-6098.
8. Yang, S.; Zheng, Y. C.; Hou, Y.; Chen, X.; Chen, Y.; Wang, Y.; Zhao, H.; Yang, H. G., Formation mechanism of freestanding CH<sub>3</sub>NH<sub>3</sub>PbI<sub>3</sub> functional crystals: in situ transformation vs dissolution–crystallization, *Chem. Mater.* **2014**, *26*, 6705-6710.
9. Brenner, T. M.; Rakita, Y.; Orr, Y.; Klein, E.; Feldman, I.; Elbaum, M.; Cahen, D.; Hodes, G., Conversion of single crystalline PbI<sub>2</sub> to CH<sub>3</sub>NH<sub>3</sub>PbI<sub>3</sub>: structural relations and transformation dynamics, *Chem. Mater.* **2016**, *28*, 6501-6510.
10. Ko, H.; Sin, D. H.; Kim, M.; Cho, K., Predicting the morphology of perovskite thin films produced by sequential deposition method: a crystal growth dynamics study, *Chem. Mater.* **2017**, *29*, 1165-1174.
11. Chen, Q.; Zhou, H.; Hong, Z.; Luo, S.; Duan, H.-S.; Wang, H.-H.; Liu, Y.; Li, G.; Yang, Y., Planar heterojunction perovskite solar cells via vapor-assisted solution process, *J. Am. Chem. Soc.* **2014**, *136*, 622-625.
12. Fu, Y.; Meng, F.; Rowley, M. B.; Thompson, B. J.; Shearer, M. J.; Ma, D.; Hamers, R. J.; Wright, J. C.; Jin, S., Solution growth of single crystal methylammonium lead halide perovskite nanostructures for optoelectronic and photovoltaic applications, *J. Am. Chem. Soc.* **2015**, *137*, 5810-5818.

13. Burschka, J.; Pellet, N.; Moon, S.-J.; Humphry-Baker, R.; Gao, P.; Nazeeruddin, M. K.; Grätzel, M., Sequential deposition as a route to high-performance perovskite-sensitized solar cells, *Nature* **2013**, *499*, 316-319.
14. Lee, J.-W.; Park, N.-G., Two-step deposition method for high-efficiency perovskite solar cells, *MRS Bull.* **2015**, *40*, 654-659.
15. Snaith, H. J., Perovskites: the emergence of a new era for low-cost, high-efficiency solar cells, *J. Phys. Chem. Lett.* **2013**, *4*, 3623-3630.
16. Zuo, L.; Dong, S.; De Marco, N.; Hsieh, Y.-T.; Bae, S.-H.; Sun, P.; Yang, Y., Morphology evolution of high efficiency perovskite solar cells via vapor induced intermediate phases, *J. Am. Chem. Soc.* **2016**, *138*, 15710-15716.
17. Meng, L.; Yao, E.-P.; Hong, Z.; Chen, H.; Sun, P.; Yang, Z.; Li, G.; Yang, Y., Pure formamidinium-based perovskite light-emitting diodes with high efficiency and low driving voltage, *Adv. Mater.* **2017**, *29*, 1603826.
18. Lee, M. M.; Teuscher, J.; Miyasaka, T.; Murakami, T. N.; Snaith, H. J., Efficient hybrid solar cells based on meso-superstructured organometal halide perovskites, *Science* **2012**, *338*, 643-647.
19. Liu, M.; Johnston, M. B.; Snaith, H. J., Efficient planar heterojunction perovskite solar cells by vapour deposition, *Nature* **2013**, *501*, 395-398.
20. Edri, E.; Kirmayer, S.; Cahen, D.; Hodes, G., High open-circuit voltage solar cells based on organic–inorganic lead bromide perovskite, *J. Phys. Chem. Lett.* **2013**, *4*, 897-902.

21. Saliba, M.; Tan, K. W.; Sai, H.; Moore, D. T.; Scott, T.; Zhang, W.; Estroff, L. A.; Wiesner, U.; Snaith, H. J., Influence of thermal processing protocol upon the crystallization and photovoltaic performance of organic–inorganic lead trihalide perovskites, *J. Phys. Chem. C* **2014**, *118*, 17171-17177.
22. Jeon, N. J.; Noh, J. H.; Kim, Y. C.; Yang, W. S.; Ryu, S.; Seok, S. I., Solvent engineering for high-performance inorganic–organic hybrid perovskite solar cells, *Nat. Mater.* **2014**, *13*, 897-903.
23. Jeon, N. J.; Noh, J. H.; Yang, W. S.; Kim, Y. C.; Ryu, S.; Seo, J.; Seok, S. I., Compositional engineering of perovskite materials for high-performance solar cells, *Nature* **2015**, *517*, 476-480.
24. Zhao, L.; Yeh, Y.-W.; Tran, N. L.; Wu, F.; Xiao, Z.; Kerner, R. A.; Lin, Y. L.; Scholes, G. D.; Yao, N.; Rand, B. P., In situ preparation of metal halide perovskite nanocrystal thin films for improved light-emitting devices, *ACS Nano* **2017**, *11*, 3957-3964.
25. Leblebici, S. Y.; Leppert, L.; Li, Y.; Reyes-Lillo, S. E.; Wickenburg, S.; Wong, E.; Lee, J.; Melli, M.; Ziegler, D.; Angell, D. K.; Ogletree, D. F.; Ashby, Paul D.; Toma, F. M.; Neaton, J. B.; Sharp, I. D.; Weber-Bargioni, A., Facet-dependent photovoltaic efficiency variations in single grains of hybrid halide perovskite, *Nat. Energy* **2016**, *1*, 16093.
26. Simpson, M. J.; Doughty, B.; Yang, B.; Xiao, K.; Ma, Y. Z., Imaging electronic trap states in perovskite thin films with combined fluorescence and femtosecond transient absorption microscopy, *J. Phys. Chem. Lett.* **2016**, *7*, 1725-1731.

27. Guo, Z.; Wan, Y.; Yang, M.; Snaider, J.; Zhu, K.; Huang, L., Long-range hot-carrier transport in hybrid perovskites visualized by ultrafast microscopy, *Science* **2017**, *356*, 59-62.
28. Nah, S.; Spokoyny, B.; Stoumpos, C.; Soe, C. M. M.; Kanatzidis, M.; Harel, E., Spatially segregated free-carrier and exciton populations in individual lead halide perovskite grains, *Nat. Photon.* **2017**, *11*, 285-288.
29. Ahmad, S.; Kanaujia, P. K.; Niu, W.; Baumberg, J. J.; Vijaya Prakash, G., In situ intercalation dynamics in inorganic–organic layered perovskite thin films, *ACS Appl. Mater. Interfaces* **2014**, *6*, 10238-10247.
30. de Quilettes, D. W.; Vorpahl, S. M.; Stranks, S. D.; Nagaoka, H.; Eperon, G. E.; Ziffer, M. E.; Snaith, H. J.; Ginger, D. S., Impact of microstructure on local carrier lifetime in perovskite solar cells, *Science* **2015**, *348*, 683-686.
31. Pellet, N.; Teuscher, J.; Maier, J.; Grätzel, M., Transforming hybrid organic inorganic perovskites by rapid halide exchange, *Chem. Mater.* **2015**, *27*, 2181-2188.
32. Wen, X.; Sheng, R.; Ho-Baillie, A. W. Y.; Benda, A.; Woo, S.; Ma, Q.; Huang, S.; Green, M. A., Morphology and carrier extraction study of organic–inorganic metal halide perovskite by one- and two-photon fluorescence microscopy, *J. Phys. Chem. Lett.* **2014**, *5*, 3849-3853.
33. Wen, X.; Ho-Baillie, A.; Huang, S.; Sheng, R.; Chen, S.; Ko, H.-c.; Green, M. A., Mobile charge-induced fluorescence intermittency in methylammonium lead bromide perovskite, *Nano Lett.* **2015**, *15*, 4644-4649.

34. Chen, S.; Wen, X.; Yun, J. S.; Huang, S.; Green, M.; Jeon, N. J.; Yang, W. S.; Noh, J. H.; Seo, J.; Seok, S. I.; Ho-Baillie, A., Spatial distribution of lead iodide and local passivation on organo-lead halide perovskite, *ACS Appl. Mater. Interfaces* **2017**, *9*, 6072-6078.
35. Zhu, F.; Men, L.; Guo, Y.; Zhu, Q.; Bhattacharjee, U.; Goodwin, P. M.; Petrich, J. W.; Smith, E. A.; Vela, J., Shape evolution and single particle luminescence of organometal halide perovskite nanocrystals, *ACS Nano* **2015**, *9*, 2948-2959.
36. Tachikawa, T.; Karimata, I.; Kobori, Y., Surface charge trapping in organolead halide perovskites explored by single-particle photoluminescence imaging, *J. Phys. Chem. Lett.* **2015**, *6*, 3195-3201.
37. Tian, Y.; Merdasa, A.; Peter, M.; Abdellah, M.; Zheng, K.; Ponseca, C. S.; Pullerits, T.; Yartsev, A.; Sundström, V.; Scheblykin, I. G., Giant photoluminescence blinking of perovskite nanocrystals reveals single-trap control of luminescence, *Nano Lett.* **2015**, *15*, 1603-1608.
38. Täuber, D.; Dobrovolsky, A.; Camacho, R.; Scheblykin, I. G., Exploring the electronic band structure of organometal halide perovskite via photoluminescence anisotropy of individual nanocrystals, *Nano Lett.* **2016**, *16*, 5087-5094.
39. Karimata, I.; Kobori, Y.; Tachikawa, T., Direct observation of charge collection at nanometer-scale iodide-rich perovskites during halide exchange reaction on  $\text{CH}_3\text{NH}_3\text{PbBr}_3$ , *J. Phys. Chem. Lett.* **2017**, *8*, 1724-1728.



40. deQuilettes, D. W.; Jariwala, S.; Burke, S.; Ziffer, M. E.; Wang, J. T. W.; Snaith, H. J.; Ginger, D. S., Tracking photoexcited carriers in hybrid perovskite semiconductors: trap-dominated spatial heterogeneity and diffusion, *ACS Nano* **2017**, *11*, 11488-11496.
41. Rosales, B. A.; Hanrahan, M. P.; Boote, B. W.; Rossini, A. J.; Smith, E. A.; Vela, J., Lead halide perovskites: challenges and opportunities in advanced synthesis and spectroscopy, *ACS Energy Lett.* **2017**, *2*, 906-914.
42. Lee, M. M.; Teuscher, J.; Miyasaka, T.; Murakami, T. N.; Snaith, H. J., Efficient hybrid solar cells based on meso-superstructured organometal halide perovskites, *Science* **2012**, *338*, 643-647.
43. Zhu, G.; Liu, P.; Hojamberdiev, M.; Zhou, J.; Huang, X.; Feng, B.; Yang, R., Controllable synthesis of PbI<sub>2</sub> nanocrystals via a surfactant-assisted hydrothermal route, *Appl. Phys. A* **2010**, *98*, 299-304.
44. Kawamura, Y.; Mashiyama, H.; Hasebe, K., Structural study on cubic-tetragonal transition of CH<sub>3</sub>NH<sub>3</sub>PbI<sub>3</sub>, *J. Phys. Soc. Jpn.* **2002**, *71*, 1694-1697.
45. Ahuja, R.; Arwin, H.; Ferreira da Silva, A.; Persson, C.; Osorio-Guillen, J. M.; Souza de Almeida, J.; Moyses Araujo, C.; Veje, E.; Veissid, N.; An, C. Y.; Pepe, I.; Johansson, B., Electronic and optical properties of lead iodide, *J. Appl. Phys.* **2002**, *92*, 7219-7224.
46. Kim, H. S.; Lee, C. R.; Im, J. H.; Lee, K. B.; Moehl, T.; Marchioro, A.; Moon, S. J.; Humphry-Baker, R.; Yum, J. H.; Moser, J. E.; Grätzel, M.; Park, N. G., Lead iodide perovskite sensitized all-solid-state submicron thin film mesoscopic solar cell with efficiency exceeding 9%, *Sci. Rep.* **2012**, *2*, 591

47. Routzahn, A. L.; Jain, P. K., Single-nanocrystal reaction trajectories reveal sharp cooperative transitions, *Nano Lett.* **2014**, *14*, 987-992.
48. Routzahn, A. L.; Jain, P. K., Luminescence blinking of a reacting quantum dot, *Nano Lett.* **2015**, *15*, 2504-2509.
49. Empedocles, S. A.; Norris, D. J.; Bawendi, M. G., Photoluminescence spectroscopy of single CdSe nanocrystallite quantum dots, *Phys. Rev. Lett.* **1996**, *77*, 3873-3876.
50. Empedocles, S. A.; Neuhauser, R.; Bawendi, M. G., Three-dimensional orientation measurements of symmetric single chromophores using polarization microscopy, *Nature* **1999**, *399*, 126-130.
51. Xu, W.; Kong, J. S.; Yeh, Y.-T. E.; Chen, P., Single-molecule nanocatalysis reveals heterogeneous reaction pathways and catalytic dynamics, *Nat. Mater.* **2008**, *7*, 992-996.
52. Zhou, X.; Andoy, N. M.; Liu, G.; Choudhary, E.; Han, K.-S.; Shen, H.; Chen, P., Quantitative super-resolution imaging uncovers reactivity patterns on single nanocatalysts, *Nat. Nanotechnol.* **2012**, *7*, 237-241.
53. Galland, C.; Ghosh, Y.; Steinbrück, A.; Sykora, M.; Hollingsworth, J. A.; Klimov, V. I.; Htoon, H., Two types of luminescence blinking revealed by spectroelectrochemistry of single quantum dots, *Nature* **2011**, *479*, 203-207.
54. Orfield, N. J.; McBride, J. R.; Keene, J. D.; Davis, L. M.; Rosenthal, S. J., Correlation of atomic structure and photoluminescence of the same quantum dot: pinpointing surface and internal defects that inhibit photoluminescence, *ACS Nano* **2015**, *9*, 831-839.

55. Orfield, N. J.; Majumder, S.; McBride, J. R.; Yik-Ching Koh, F.; Singh, A.; Bouquin, S. J.; Casson, J. L.; Johnson, A. D.; Sun, L.; Li, X.; Shih, C.-K.; Rosenthal, S. J.; Hollingsworth, J. A.; Htoon, H., Photophysics of thermally-assisted photobleaching in “Giant” quantum dots revealed in single nanocrystals, *ACS Nano* **2018**, *12*, 4206-4217.

## **Chapter 4**

# **Fluorescence Microscopy of Single Lead Bromide Nanocrystals Reveals Sharp Transitions during Their Transformation to Methylammonium Lead Bromide**

Adapted from (Yin, B.; Cavin, J.; Wang, D.; Khan, D.; Shen, M.; Laing, C.; Mishra, R. and Sadtler, B., Fluorescence microscopy of single lead bromide nanocrystals reveals sharp transitions during their transformation to methylammonium lead bromide, *J. Mater. Chem. C* **2019**, Advance Article) with permission from the Royal Society of Chemistry.

## 4.1 Introduction

In **Chapter 3** fluorescence microscopy was used to observe in situ the transformation from  $\text{PbI}_2$  microcrystals ( $\sim 10 \mu\text{m}$  in size) to  $\text{CH}_3\text{NH}_3\text{PbI}_3$  perovskite. It offers insights, like the preference of locations where the conversion starts, that is lost during the ex situ characterization of this reaction. However, the observed rates of solid-state transformations in microscale crystals described in **Chapter 3** are the result of many nucleation and growth events occurring simultaneously.<sup>1-3</sup> Furthermore, the solid-state diffusion of ions can be the rate-determining step for polycrystalline films with thicknesses greater than 100 nm. For example, the interfacial reaction between  $\text{CH}_3\text{NH}_3\text{I}$  and  $\text{PbI}_2$  at the top surface of a  $\text{PbI}_2$  film blocks diffusion of  $\text{CH}_3\text{NH}_3^+$  and  $\text{I}^-$  ions further into the film.<sup>1</sup> On the other hand, a nanoscale crystal can transform via a single nucleation event when its size is comparable to the critical nuclei needed for the new phase to form. The high surface-to-volume ratio of nanoscale crystals also facilitates rapid diffusion of ions in and out of the crystal.<sup>4-14</sup> By studying the reactivity and photophysics of single nanocrystals, one can observe behavior that is obscured in the ensemble average.<sup>15, 13-22</sup> For example, a related solid-state transformation to the one studied in this report is cation exchange in semiconductor chalcogenide nanocrystals where cations in solution replace the cations within the nanocrystal lattice.<sup>6-14</sup> Using fluorescence microscopy, Routzhan and Jain observed that the conversion of individual CdSe nanocrystals to  $\text{Ag}_2\text{Se}$  via cation exchange is much faster than the time it takes for the ensemble of nanocrystals to transform.<sup>13</sup> Thus, the

ensemble reaction rate is dictated by a population of nanocrystals that transform abruptly at different times rather than the simultaneous conversion of the entire population through multiple intermediate states.

In this chapter, we used fluorescence microscopy to image the conversion of single  $\text{PbBr}_2$  nanocrystals to  $\text{CH}_3\text{NH}_3\text{PbBr}_3$  via ion intercalation. The change in fluorescence intensity provides a signature for this reaction. While this reaction has been previously monitored in both polycrystalline films and microscale crystals,<sup>1,23</sup> we obtain new insights by isolating individual nucleation and growth events among nanoscale crystallites. We observe significant differences in the reaction time and concentration dependence of individual particles compared to their ensemble average. Applying statistical analysis to these reaction trajectories, we develop a model for how the phase transformation of individual nanocrystals leads to the observed ensemble behavior.

## 4.2 Experimental Details

### 4.2.1 Materials and Chemical Synthesis

*Materials:* Lead(II) oxide ( $\text{PbO}$ ,  $\geq 99.9\%$ ), tetrabutylammonium bromide (TBAB,  $\geq 98\%$ ), oleylamine (OLA, 70%), methylamine solution ( $\text{CH}_3\text{NH}_2$ , 33 wt. % in absolute ethanol), oleic acid (90%), 2-propanol (IPA, anhydrous, 99.5%), tert-butanol (anhydrous,  $\geq 99.5\%$ ) and toluene (anhydrous, 99.8%) were purchased from Sigma-Aldrich Inc. 1-octadecene (ODE, tech. 90%) and hydrobromic acid (HBr, ACS 47.0 – 49 %) were purchased from Alfa Aesar. All chemicals were used as received.

*Synthesis of lead bromide (PbBr<sub>2</sub>) nanocrystals:* The procedure for synthesizing PbBr<sub>2</sub> nanocrystals was adapted from a previous report.<sup>24</sup> In a typical reaction, a two-flask method was used in which Flask (I) contained the bromide precursor and Flask (II) contained the lead precursor. A Schlenk line system was used in the synthesis to evacuate each flask and put it under an environment of N<sub>2</sub>. In Flask (I), 2 mmol of TBAB was used as the bromide precursor and mixed with OLA (5 mL) and ODE (5 mL). Note that TBAB does not dissolve in this solvent system until after heating. Flask (I) was evacuated using a Schlenk line to a pressure below 150 milliTorr, heated to 120°C, and held at this temperature while stirring for 90 min to remove water and oxygen. Subsequently, Flask (I) was switched from vacuum to a N<sub>2</sub> environment and heated to 200°C for 60 min. At this point the solution in Flask (I) turned clear indicating that the TBAB had dissolved. The heating source was then removed to allow Flask (I) to cool. Once the temperature of Flask (I) reached 50°C, it was kept at this temperature to avoid solidification. In Flask (II), 1 mmol of PbO used as the lead precursor, 1 mL (3 mmol) of oleic acid, and 15 mL of ODE were mixed together with stirring. Similar to Flask (I), Flask (II) was put under vacuum and heated to 100°C for 90 min with stirring to remove water and oxygen. Then Flask (II) was allowed to cool to 80°C under a N<sub>2</sub> environment, where it was kept at this temperature for 60 min. At this point, the mixture in Flask (II) turned clear and colorless. While still under a N<sub>2</sub> environment, the temperature of Flask (II) was then raised to 200°C. After the temperature of Flask (II) stabilized at 200°C, the solution from Flask (I) was injected into to Flask (II) with vigorous stirring. After mixing the contents of the two flasks, the reaction was kept at 200°C for 15 min and then removed the heating source. The solution in Flask (II) was clear and colorless at this point. Next, 10 mL of anhydrous toluene was injected into Flask (II) to cool the reaction solution. After Flask (II) cooled to room temperature, the product solution was stored in an argon-filled glovebox for future use. Over a 24-hour period, a white precipitate formed in Flask

(II). This precipitate was determined to be Pb(OH)Br by x-ray diffraction, while the clear supernatant contained only PbBr<sub>2</sub> nanocrystals as determined by x-ray diffraction, electron diffraction, and x-ray photoelectron spectroscopy.

*Washing procedure for PbBr<sub>2</sub> nanocrystals:* We found that solutions of PbBr<sub>2</sub> nanocrystals remained stable for longer periods of time (up to 6 months) by keeping the nanocrystals in the original reaction solution. Therefore, individual aliquots were washed prior to characterization. In a typical washing procedure, 1 mL of anhydrous 2-propanol was added to 0.2 mL of the clear supernatant of the PbBr<sub>2</sub> reaction solution in a glovebox. After thoroughly mixing the solution, the nanocrystals began to precipitate as a white powder. The solution was transferred to a centrifuge tube, taken out of the glovebox, and centrifuged at 5,000 rpm for 5 min. The centrifuge tube was then brought back into the glovebox, and the supernatant was removed. Next, 6 mL of anhydrous toluene were added to the white precipitate. After mixing, the white precipitate dispersed back to form a clear colloidal solution. This solution could be used to characterize the nanocrystals by TEM, UV-Visible absorption, and photoluminescence spectroscopy. For characterization by x-ray diffraction and x-ray photoelectron spectroscopy, the sample was washed twice using the procedure described above and dispersed in isopropanol rather than toluene.

*Synthesis of methylammonium bromide (CH<sub>3</sub>NH<sub>3</sub>Br):* Methylammonium bromide (CH<sub>3</sub>NH<sub>3</sub>Br) was synthesized following a previously reported procedure for making CH<sub>3</sub>NH<sub>3</sub>I (except HBr was used instead of HI).<sup>25</sup> First, 24 mL of a CH<sub>3</sub>NH<sub>2</sub> solution (33 wt. % in ethanol) was reacted with 10 mL of HBr (47-49%) in 100 mL ethanol. After the reaction, a rotary evaporator was used to remove ethanol and isolate the resulting CH<sub>3</sub>NH<sub>3</sub>Br powder. The white CH<sub>3</sub>NH<sub>3</sub>Br



powder was collected and further dried in a vacuum oven at 60°C overnight. The CH<sub>3</sub>NH<sub>3</sub>Br powder was stored in a glovebox for future use.

#### 4.2.2 Details of Characterization

To prepare samples for x-ray diffraction (XRD), several drops of the washed nanocrystals (dispersed in anhydrous 2-propanol) were drop-cast onto a zero-background, silicon diffraction plate (MTI Corporation). The solution was allowed to dry on the diffraction plate in a glovebox. XRD patterns were then collected using a Bruker D8 Advance X-ray Diffractometer (Cu K $\alpha$  = 0.15418 nm). The step size for the XRD measurements was 0.02° in 2 $\theta$ , and the scan rate was 0.5 s per step.

X-ray photoelectron spectroscopy (XPS) was performed using a Physical Electronics 5000 VersaProbe II Scanning ESCA (XPS) Microprobe system with a base pressure below 1  $\times$  10<sup>-9</sup> Torr. XPS data were acquired using the 1486.6 eV line from a monochromated Al K $\alpha$  source at 150 W with a multichannel detector set to a pass energy of 23.5 eV for the high-resolution scans. The expected peak positions and chemical shifts were obtained from the National Institute of Standards and Technology (NIST) X-ray Photoelectron Spectroscopy Database.<sup>26</sup>

To obtain ensemble optical spectra of the PbBr<sub>2</sub> nanocrystals after different amounts of CH<sub>3</sub>NH<sub>3</sub>Br were added to the solution (see **Figure 4.5**), the nanocrystals were prepared in the following manner. An aliquot of the PbBr<sub>2</sub> nanocrystals after washing as described above was further diluted by approximately 2.5 times. For example, 10 mL of the washed solution was diluted to 25 mL solution with anhydrous toluene. For each titration, 3 mL of the diluted solution was added to a quartz cuvette. Next, the following amounts of a CH<sub>3</sub>NH<sub>3</sub>Br solution

(0.55 mg/mL in anhydrous IPA) were added to each cuvette: 10  $\mu$ L, 20  $\mu$ L, 30  $\mu$ L, 60  $\mu$ L, 90  $\mu$ L, and 180  $\mu$ L. The UV-Vis absorption and photoluminescence spectra were measured immediately after addition of the  $\text{CH}_3\text{NH}_3\text{Br}$  solution. When 180  $\mu$ L of the solution was added, no obvious changes in the absorption edge of the nanocrystals was observed compared to when 90  $\mu$ L was added. Thus, we considered the nanocrystals to be completely transformed to  $\text{CH}_3\text{NH}_3\text{PbBr}_3$  using the 90  $\mu$ L aliquot.

UV-Vis absorption spectra were measured using a Perkin-Elmer Lambda 950 spectrometer equipped with a 150-mm, integrating sphere, a PMT detector, a tungsten halogen lamp for the visible region (350–800 nm), and a deuterium lamp for the ultraviolet region (250–350 nm). Each cuvette was placed at the front entrance of the integrating sphere to measure the transmitted light. The scan rate for the measurement was 266.75 nm/min, and the step size was 1.0 nm.

Photoluminescence spectra were recorded using a Cary Eclipse fluorescence spectrophotometer. The excitation wavelength was set at 400 nm, and photoluminescence spectra were collected from 450 nm to 600 nm. The scan rate for each spectrum was 600 nm/min, and the step size was 1 nm.

Transmission electron microscopy (TEM) was performed using a JEOL 2000FX transmission electron microscope with an acceleration voltage of 200 kV using a LaB6 filament as the electron source. After washing, a drop of the nanocrystal solution was drop-cast onto a TEM grid (Ted Pella, Inc #01811). Electron diffraction patterns were obtained using a more concentrated solution of nanocrystals. The camera length was 150 cm.

### 4.2.3 Flow Cell Preparation

Home-made flow cells were used for all fluorescence microscopy experiments. The preparation followed a procedure described by Chen and coworkers with some modifications.<sup>13</sup> The flow cells consisted of a top glass slide (25 × 75 mm, 1.0 mm thick) and a bottom coverslip (24 × 50 mm, #1.5). For the top glass slide, two holes (1 mm in diameter with a 25-mm separation) were drilled to allow for liquid to flow in and out of the flow cell. The holes were drilled by immersing the slide in water and using a 1 mm, diamond-coated drill bit at speed of about 25 kRPM using a dremel (DREMEL 4000). Before use, the drilled glass slides were cleaned by sonicating in acetone for 30 min and dried using N<sub>2</sub> gas.

The PbBr<sub>2</sub> nanocrystals were first spin-coated onto the bottom coverslip before assembling the flow cell. In order to achieve a uniform dispersion of single nanocrystals on the coverslips, we found that the solution of PbBr<sub>2</sub> nanocrystals needed to be diluted by a factor of approximately 3200 compared to the as-synthesized sample in solution. Anhydrous toluene was originally used to dilute the PbBr<sub>2</sub> solution. However, toluene has a relatively large contact angle on the glass coverslips, which often led to a non-uniform dispersion of nanocrystals. To improve the dispersion, a mixture of anhydrous toluene and anhydrous IPA was used to lower the contact angle. When the volume ratio between toluene and IPA was 3:1, a uniform dispersion of PbBr<sub>2</sub> nanocrystals on the coverslips was achieved.

To assemble a flow cell, two polytetrafluoroethylene (PTFE) tubes (Cole-Parmer, 1/32 ID × 1/16 OD) were first attached to the holes of the top glass slide. Epoxy (Gorilla 5 min epoxy) was used to seal around the tubes, and the epoxy was allowed to cure for at least 180 min. After curing, double-sided tape (3M) was placed on the top glass slide to form a rectangular shaped flow channel surrounding the two drilled holes. The bottom coverslip was then adhered to the

tape with the nanocrystals facing in between the two slides. The height of the flow channel was defined by the thickness of the double-sided tape, which was about 60  $\mu\text{m}$ . The volume of the channel was approximately 6  $\mu\text{L}$ . Then epoxy was applied around the double-sided tape to create a liquid tight seal. The epoxy was allowed to dry and solidify under vacuum for at least 60 min before conducting the microscopy experiments described in **Section 4.2.4**.

#### **4.2.4 Monitoring Single Nanocrystal Conversion with Fluorescence Microscopy**

Single-nanocrystal fluorescence imaging was carried out using a Nikon N-STORM microscopy system consisting of a Nikon TiE motorized inverted optical microscope and a Nikon CFI-6-APO TIRF 100 $\times$  oil-immersion objective lens with a numerical aperture of 1.49 and a working distance of 210  $\mu\text{m}$ . The microscope also contains optics for imaging using differential interference contrast (DIC), which was used for rough focusing of the top of the coverslip. The microscope was then switched to fluorescence mode with a long exposure time (1 s) to bring the coverslip into fine focus. The Nikon Perfect Focus 3 system was used to maintain focal stability during imaging. As shown in **Figure 4.6**, the nanocrystals on the bottom coverslip of the flow cell were photoexcited through the objective using filtered light from a white light-emitting diode (LED) with an irradiance of 155  $\mu\text{W}/\text{cm}^2$  near the focal plane. A filter cube was used (Chroma, set #49002) with an excitation filter that had 90% transmission for blue light of wavelengths between 450 and 480 nm. The emission filter had 90% transmission between 500 and 540 nm, while the photoluminescence maximum for a solution of the  $\text{CH}_3\text{NH}_3\text{PbBr}_3$  nanocrystals was  $\sim 510$  nm. A dichroic mirror in the filter cube with a cutoff wavelength of 500 nm was used to separate the excitation and emission. An Andor iXon 897 electron-multiplying

CCD with single photon sensitivity ( $512 \times 512$ ,  $16 \mu\text{m}$  pixels, 90% quantum efficiency) was used to detect the fluorescent signals. The time resolution of the EMCCD camera is 0.02 s, which means the camera will take 50 measurements in 1 s. Images were collected with an exposure time of 2 ms.

During a typical experiment, the entrance tube of the flow cell was connected to one end of a three-way tee connection (Cole-Parmer, tube OD 1 to 4 mm). The other two ends of the three-way tee were each connected to a syringe pump. One syringe pump was used to inject 1-octadecene while the other syringe pump was used to introduce the  $\text{CH}_3\text{NH}_3\text{Br}$  solution.  $\text{CH}_3\text{NH}_3\text{Br}$  at different concentrations was dissolved in a mixture of tert-butanol and 1-octadecene with a volume ratio of 2:3. Before imaging the transformation of the nanocrystals, pure 1-octadecene was injected into the flow cell at a typical injection rate of 7.5 mL/h. The focus of the microscope was then readjusted to the top surface of coverslip where the nanocrystals were located. After focusing, the addition of pure 1-octadecene was stopped, and the  $\text{CH}_3\text{NH}_3\text{Br}$  reactant solution was injected at a rate of 5 mL/h. Switching between the two syringe pumps would create a small air bubble in the PTFE tube, which was used as a marker for the flow of the  $\text{CH}_3\text{NH}_3\text{Br}$  solution. Recording of the fluorescence video began when the air bubble was close to entering the flow cell.

#### **4.2.5 Data Analysis**

All fluorescence microscopy videos (time-stacks of images) were recorded using Nikon Elements Software (Advanced Research 4.50). Nikon Elements is equipped with basic analysis functions. For example, the intensity trajectory for the entire field-of-view (wide-field intensity

in **Figure 4.7e**) could be directly measured using this software. Single nanocrystals were identified manually from stack of image frames. Regions of Interest (ROIs) were defined around single emitting nanocrystals where no intensity from nearby nanocrystals was present. Intensity trajectories from these ROIs were then measured using the Elements software, and the data was exported into an Excel spreadsheet. The following data processing was then performed using Matlab.

*Waiting time analysis:* For each single-nanocrystal trajectory, the waiting time was determined when the intensity of the trajectory reached a threshold intensity. The threshold intensity value,  $V$ , is given by the following equation:

$$V = m + 6 \times \sigma \quad (4.1)$$

where  $m$  is the mean value of the intensity before the reaction started, and  $\sigma$  is the standard deviation of a Gaussian fit to the noise. For a given ROI, the  $m$  and  $\sigma$  values were determined using 2 s of the video (100 recorded points in the video) at the time point before the nanocrystal started to “turn on” (i.e., before the fluorescence intensity began to increase). Gaussian fitting of the distributions of waiting times were performed in Origin. For each experiment, the video recording started when the air bubble formed after switching solutions entered the flow cell. As the region observed in the flow cell varied for each recording, the time at which the first nanocrystal was observed to turn on after the recording started could vary by a few seconds even when the same concentration of  $\text{CH}_3\text{NH}_3\text{Br}$  was used. When multiple videos were recorded at a single concentration, the Gaussian fits were aligned based on the mean value of the fit. After aligning the histograms, the first nanocrystal to transform was given a relative waiting time of 0 s. Thus, the waiting times were measured relative to the time when the first nanocrystal was observed to transform.

*Switching time,  $\tau$ , analysis:* For each individual nanocrystal, the switching time,  $\tau$ , was determined by fitting a segment of its intensity trajectory  $I(t)$  to a sigmoidal function:

$$I(t) = I_{initial} + \frac{(I_{final} - I_{initial})}{1 + \exp\{(b - t)/\tau\}} \quad (4.2)$$

where  $I_{initial}$  is the mean intensity value of the base line at the start of the trajectory (i.e. the value of  $m$  in equation 1),  $I_{final}$  is the mean intensity value at the end of the fitted segment when the intensity value was stable, and  $b$  and  $\tau$  are parameters that were fit using Matlab. All scripts used in Matlab to analyze the data can be found in the **Appendix** of this dissertation.

#### 4.2.6 Monte Carlo Simulations

We used five different physical models that describe how intercalation events are affected by ions that have already been intercalated. For all our models, we assume that the energetic cost for the first intercalation is the same.

*Diffusion-Limited:* This model can be considered to be the control case. In it, ion intercalation is purely diffusion-limited such that previous intercalations bear no consequence for future intercalations. In this case the energy required for ions to intercalate is constant.

*Positive Cooperativity:* Routzahn and Jain previously studied cation exchange in CdSe nanocrystals using single-nanocrystal fluorescence.<sup>52</sup> As in our system, individual fluorescence trajectories in CdSe nanocrystals exhibited much shorter switching times than the ensemble. They proposed positive cooperativity as an explanation for this phenomenon. In positive

cooperativity, each additional ion exchanged/intercalated reduces the energy of the next event by a constant amount.

*Continuous Nucleation:* This model is an adaptation of the classical nucleation model where the growth of a new phase is determined by a radius ( $r$ )-dependent change in free energy. The competition between volume and surface area of newly form phase creates a critical radius,  $r_c$ , at the maximum in free energy after which increasing the size/radius of the nuclei is favorable and spontaneous.

*Sudden Nucleation:* This model is similar to the continuous nucleation case except that we use diffusion-limited growth before the new phase reaches a critical radius,  $r_c$ . After reaching the critical radius, there is a sudden drop in the formation energy of the new phase.

*Phase Transformation and Nucleation:* The structure of  $\text{PbBr}_2$  and  $\text{CH}_3\text{NH}_3\text{PbBr}_3$  are not related by symmetry operations, that is they lack group-subgroup relations. Therefore, the transformation must proceed through reconstructive transitions. In this model, intercalation is assumed to be diffusion-limited until a critical point after which a perovskite phase is adopted. At this point, the presence of many  $\text{CH}_3\text{NH}_3^+$  and  $\text{Br}^-$  vacancy sites in the perovskite structure is expected to favor additional ion intercalation. Hence, we have used a continuous nucleation model to simulate the further growth of  $\text{CH}_3\text{NH}_3\text{PbBr}_3$  within the perovskite structure.



## 4.3 Results and Discussion

### 4.3.1 Synthesis of PbBr<sub>2</sub> Nanocrystals and Their Conversion to CH<sub>3</sub>NH<sub>3</sub>PbBr<sub>3</sub>.

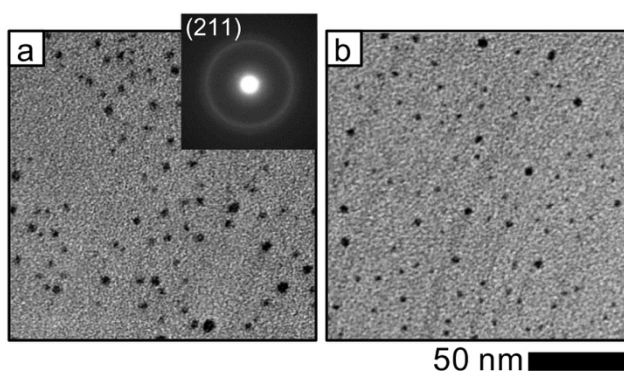


**Figure 4.1.** TEM images of (a) the initial PbBr<sub>2</sub> nanocrystals and (b) resulting CH<sub>3</sub>NH<sub>3</sub>PbBr<sub>3</sub> nanocrystals after reaction with CH<sub>3</sub>NH<sub>3</sub>Br. The inset (a) shows an electron diffraction pattern for a cluster of PbBr<sub>2</sub> nanocrystals. The bright ring corresponds to the d-spacing for the (211) plane of PbBr<sub>2</sub>. The scale bar of 50 nm applies to both images.

Lead bromide nanocrystals were synthesized using a procedure reported by Scholes and coworkers (see the **Experimental Detail 4.2.1** for the synthetic procedure).<sup>24</sup> **Figure 4.1a** shows a transmission electron microscopy (TEM) image of the initial PbBr<sub>2</sub> nanocrystals. The average diameter for these PbBr<sub>2</sub> nanocrystals was  $3.9 \pm 0.8$  nm (average  $\pm$  1<sup>st</sup> standard deviation) as shown in **Figure 4.2** for a histogram of nanocrystal diameters. An electron diffraction pattern measured for a cluster of nanocrystals shows a ring matching the d-spacing for the (211) planes of PbBr<sub>2</sub>. While peaks in the x-ray diffraction pattern were broad, the most intense peak also matched the (211) d-spacing of PbBr<sub>2</sub> (see **Figure 4.3**).

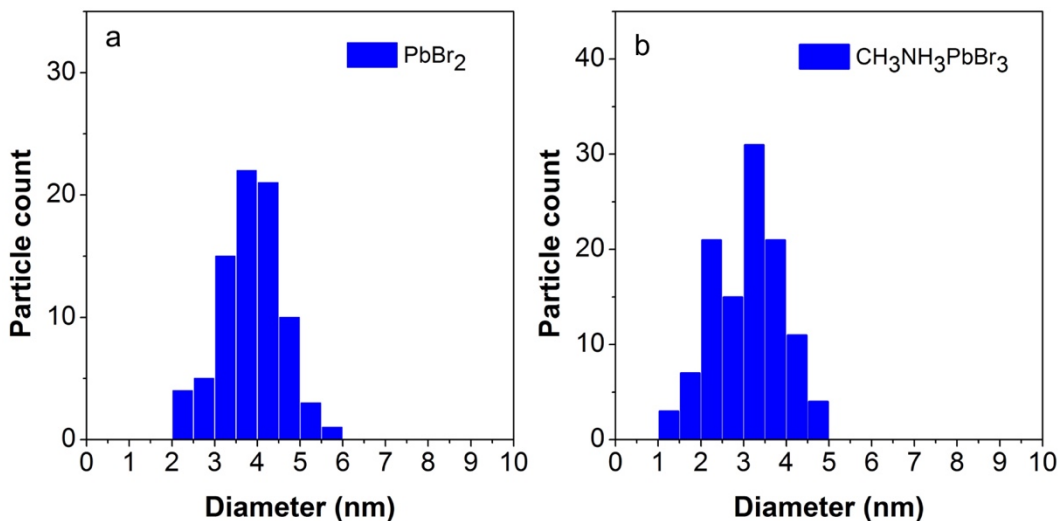


**Figure 4.2.** Histograms showing the size distribution of (a)  $\text{PbBr}_2$  and (b)  $\text{CH}_3\text{NH}_3\text{PbBr}_3$  nanocrystals measured using TEM images for the same samples shown in **Figure 4.1**

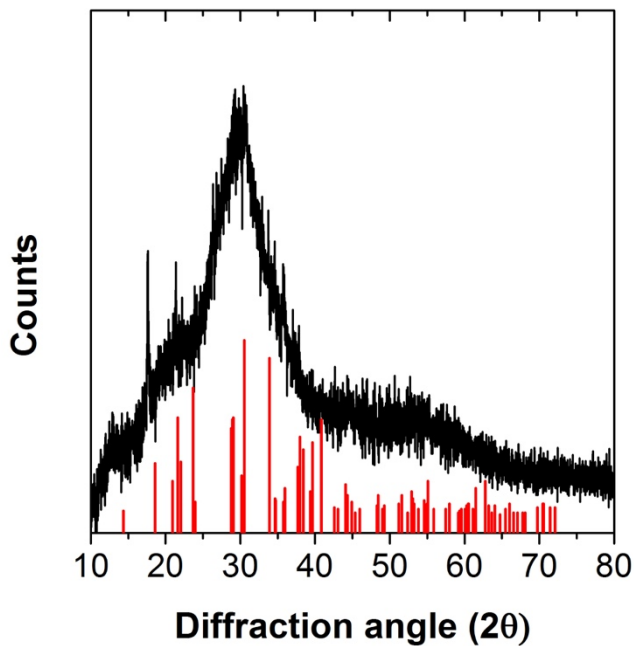


**Figure 4.3.** XRD pattern of the as-synthesized nanocrystals. The pattern obtained from a bare Si diffraction plate was subtracted from the sample pattern. The red lines correspond to the reflections for a standard XRD powder pattern of  $\text{PbBr}_2$  (PDF card # 031-0679).

X-ray photoelectron spectroscopy performed on dried films of the nanocrystals indicated the presence of Pb in the +2 oxidation state and Br in the -1 oxidation state as expected for PbBr<sub>2</sub>.

**Figure 4.4a, b** shows x-ray photoelectron spectra in the binding energy regions for Pb 4f and Br 3d electrons, respectively. After baseline subtraction, the binding energy of the Pb 4f<sub>7/2</sub> peak (lower binding energy peak in **Figure 4.4a**) is 139.0 eV, and the binding energy of the Br 3d peak is 68.8 eV. The binding energy ranges provided in the National Institute of Standards and Technology (NIST) X-ray Photoelectron Spectroscopy Database are 138.5 eV to 139.0 eV for Pb<sup>2+</sup> in a lead halide and 68.5 eV to 69.0 eV for Br<sup>-</sup> in PbBr<sub>2</sub>.<sup>26</sup> Therefore, the spectra obtained for the nanocrystals match the expected photoelectron spectra for PbBr<sub>2</sub>.

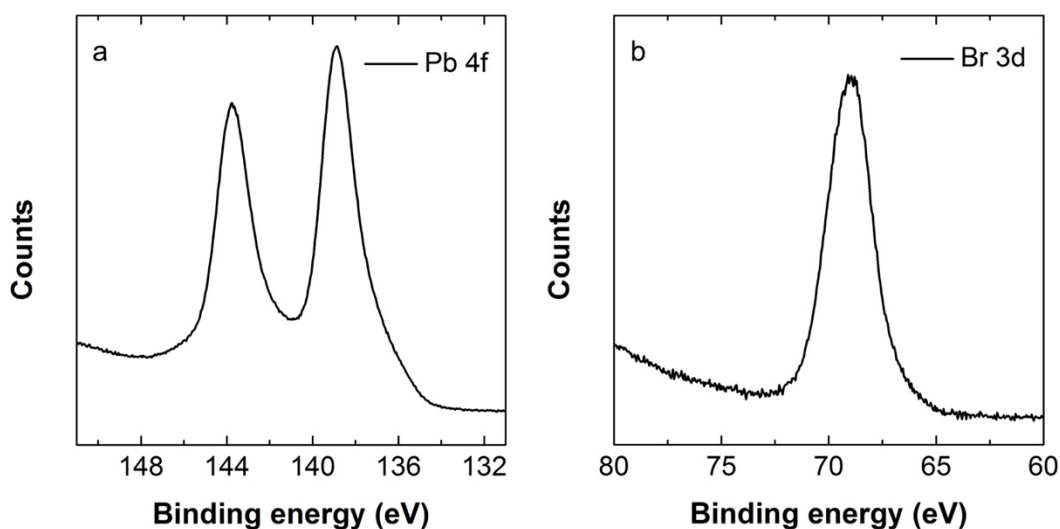


**Figure 4.4.** X-ray photoelectron spectra of the as-synthesized PbBr<sub>2</sub> nanocrystals showing the binding energy regions for (a) Pb 4f electrons in and (b) Br 3d electrons.

A TEM image of the product after the addition of CH<sub>3</sub>NH<sub>3</sub>Br to a solution of PbBr<sub>2</sub> nanocrystals is shown in **Figure 4.1b**. The average diameter for the final nanocrystals was 3.1 ± 0.8 nm (average ± 1<sup>st</sup> standard deviation, see **Figure 4.2**). Considering the larger lattice volume of CH<sub>3</sub>NH<sub>3</sub>PbBr<sub>3</sub> compared to PbBr<sub>2</sub>, the smaller size suggests etching of the nanocrystals

during the transformation. Partial dissolution of the lead halide has been previously observed when this reaction is performed on microscale crystals and in thin films.<sup>23, 27</sup>

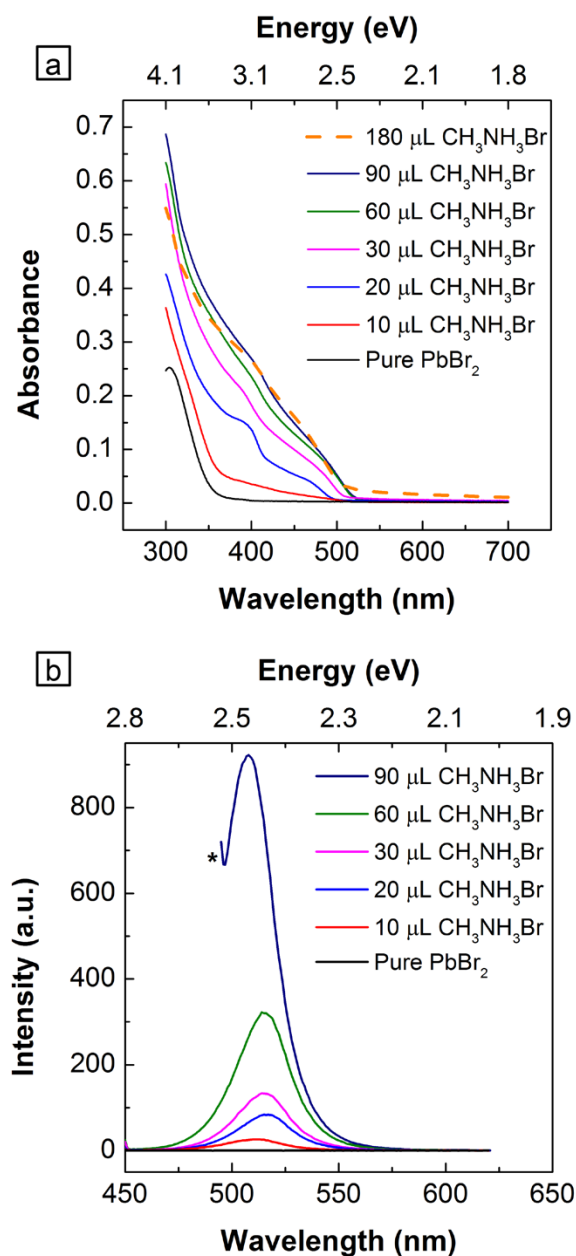


**Figure 4.5.** Optical spectra showing the conversion of PbBr<sub>2</sub> nanocrystals to CH<sub>3</sub>NH<sub>3</sub>PbBr<sub>3</sub>. (a) Absorption spectra of the nanocrystals after the addition of increasing amounts of CH<sub>3</sub>NH<sub>3</sub>Br. (b) Photoluminescence spectra of the nanocrystals after the addition of increasing amounts of CH<sub>3</sub>NH<sub>3</sub>Br. The excitation wavelength was 400 nm for all samples except for the 90 μL aliquot in which the excitation wavelength was increased to 475 nm to reduce the emission intensity.

We next monitored this transformation *ex situ* by adding varying amounts of  $\text{CH}_3\text{NH}_3\text{Br}$  (0.55 mg/mL in anhydrous isopropanol) to solutions of  $\text{PbBr}_2$  nanocrystals and recording the resulting absorption and photoluminescence spectra (**Figure 4.5**). The absorption spectra showed a progressive increase in visible absorption at wavelengths from 300 to 510 nm when increasing amounts of  $\text{CH}_3\text{NH}_3\text{Br}$  were added (**Figure 4.5a**). After the addition of 90  $\mu\text{L}$  of the  $\text{CH}_3\text{NH}_3\text{Br}$  solution, the absorption onset was 510 nm. When larger amounts of the  $\text{CH}_3\text{NH}_3\text{Br}$  solution were added, the absorption onset remained the same. However, the nanocrystals began to precipitate, which led to scattering in the absorption spectra (see dashed, orange trace for 180  $\mu\text{L}$   $\text{CH}_3\text{NH}_3\text{Br}$  in **Figure 4.5a**). The initial  $\text{PbBr}_2$  nanocrystals were non-fluorescent, but became highly fluorescent when increasing amounts of  $\text{CH}_3\text{NH}_3\text{Br}$  were added. For different amounts of  $\text{CH}_3\text{NH}_3\text{Br}$ , the maxima in the fluorescence spectra varied between 510 and 516 nm. Both the absorption onset and fluorescence maximum of the nanocrystals are blue-shifted compared to the bulk electronic band gap of 2.3 eV ( $\sim 540$  nm) for  $\text{CH}_3\text{NH}_3\text{PbBr}_3$ .<sup>28</sup> Size-dependent blue-shifts have been previously observed for  $\text{CH}_3\text{NH}_3\text{PbBr}_3$  and  $\text{CH}_3\text{NH}_3\text{PbI}_3$  nanocrystals with dimensions smaller than  $\sim 5$  nm and have been attributed to both quantum-confinement as well as structural distortions in the crystals.<sup>24, 29-31, 32</sup> The progressive blue shift in the fluorescence maxima when larger amounts of  $\text{CH}_3\text{NH}_3\text{Br}$  were added (ranging from 20 to 90  $\mu\text{L}$  of the  $\text{CH}_3\text{NH}_3\text{Br}$  solution) is likely due to etching of the nanocrystals as observed by TEM. In the measurements described below, we use the dramatic changes in fluorescence intensity for single nanocrystals when  $\text{CH}_3\text{NH}_3\text{Br}$  is added to monitor this reaction rather than the spectral shift of the emission band.

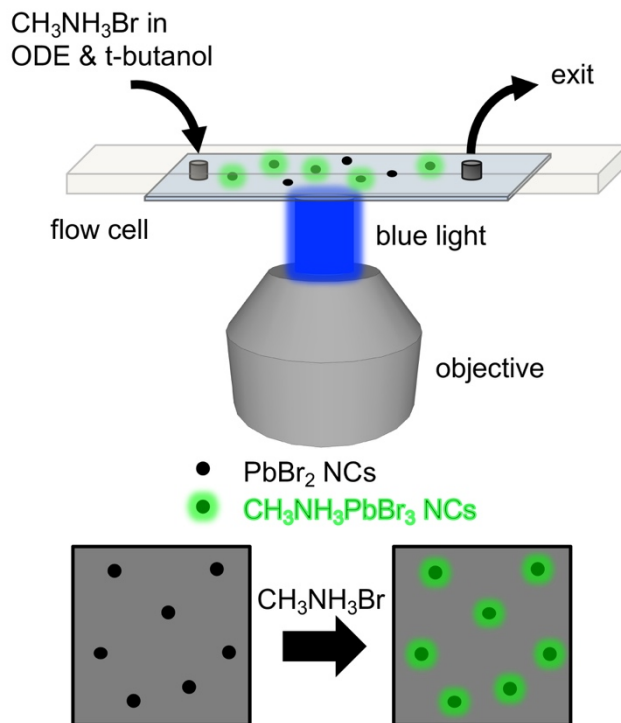


**Figure 4.6.** Experimental configuration used to observe the transformation of single PbBr<sub>2</sub> nanocrystals to CH<sub>3</sub>NH<sub>3</sub>PbBr<sub>3</sub>. Upon excitation with blue light (450 to 480 nm), the initial PbBr<sub>2</sub> nanocrystals are non-fluorescent while the product CH<sub>3</sub>NH<sub>3</sub>PbBr<sub>3</sub> nanocrystals are highly fluorescent. A schematic of the microscope field-of-view is shown at the bottom. Black dots represent PbBr<sub>2</sub> nanocrystals, and green dots represent CH<sub>3</sub>NH<sub>3</sub>PbBr<sub>3</sub> nanocrystals after the transformation. ODE = 1-octadecene.

### 4.3.2 Single-Particle Fluorescence Trajectories

**Figure 4.5** shows how the optical properties of the initial PbBr<sub>2</sub> nanocrystals changed after varying amounts of CH<sub>3</sub>NH<sub>3</sub>Br were added. However, these ensemble averages of optical signatures can mask important information about the reaction, such as whether individual nanocrystals reach the same stage of conversion when a given amount of reactant is added. We next used fluorescence microscopy to image the transformation of individual nanocrystals in situ. The experimental set-up is shown in **Figure 4.6** and is described further in the **Experimental Details 4.2.4**. Our set-up is similar to that used in previous studies by Routzahn and Jain, who

monitored cation exchange between CdSe and Ag<sub>2</sub>Se nanocrystals.<sup>13-14</sup> PbBr<sub>2</sub> nanocrystals are spin-coated onto a microscope coverslip, which formed the bottom half of a flow cell. The flow cell is placed over the objective of an inverted optical microscope. The flow cell is initially filled with 1-octadecene (ODE), and a syringe pump is used to introduce a solution of CH<sub>3</sub>NH<sub>3</sub>Br at different concentrations in ODE and tert-butanol (volume ratio of 3:2) into the flow cell. Under excitation with blue light (450 to 480 nm) from a light-emitting diode sent through the objective, the initial field-of-view is dark as the PbBr<sub>2</sub> nanocrystals are transparent at these wavelengths (bottom left in **Figure 4.6**). On the other hand, the CH<sub>3</sub>NH<sub>3</sub>PbBr<sub>3</sub> nanocrystals are highly emissive when irradiated with wavelengths below 500 nm. (bottom right in **Figure 4.6**). After the introduction of CH<sub>3</sub>NH<sub>3</sub>Br, the conversion of individual nanocrystals is marked by the appearance of bright spots in the microscope field-of-view.

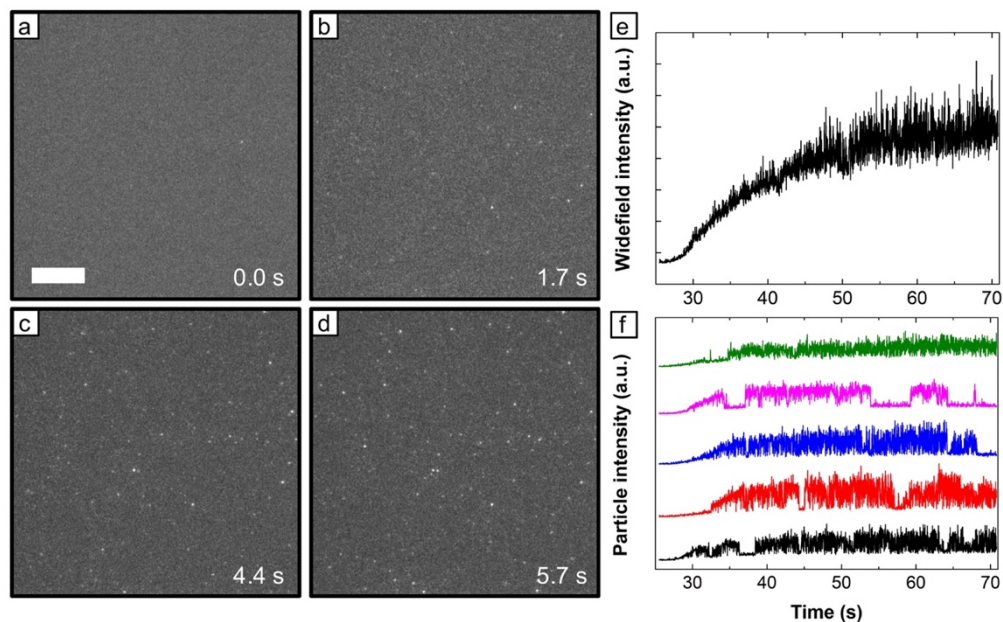


**Figure 4.7.** Imaging the transformation of single PbBr<sub>2</sub> nanocrystals to CH<sub>3</sub>NH<sub>3</sub>PbBr<sub>3</sub>. (a-d) Selected frames from a video recording of the fluorescence intensity under excitation with blue light and using a CH<sub>3</sub>NH<sub>3</sub>Br concentration of 0.4 mg/mL. The first frame (0.0 sec) corresponds to the time when the first fluorescent spot appeared. The scale bar shown in (a) is 5 μm and applies to all four images. (e) The integrated intensity versus time over the entire field-of-view for the same recording. (f) Intensity trajectories for individual nanocrystals from the same recording.

By imaging this transformation in situ, we observed that single nanocrystals turn on (i.e., become bright) on a shorter time scale compared to intensity rise for the ensemble of particles (i.e., all particles within the field-of-view). Shortly after injecting the  $\text{CH}_3\text{NH}_3\text{Br}$  solution, fluorescent spots begin to appear stochastically within the microscope field-of-view (**Figure 4.7a-d**). Based on the fluorescence spectra shown in **Figure 4.5**, we attribute the appearance of these bright spots to the formation of  $\text{CH}_3\text{NH}_3\text{PbBr}_3$  nanocrystals. As seen in **Figure 4.7e**, the integrated intensity for all nanocrystals within field-of-view increased over a period of tens of seconds. The integrated intensity rise for the ensemble became sharper when the concentration of  $\text{CH}_3\text{NH}_3\text{Br}$  was increased (see **Figure 4.8**). **Figure 4.7f** shows intensity trajectories for several representative particles from the same video recording. Qualitatively, the intensity rises for these individual nanocrystals occur over a few seconds. However, once the solution of  $\text{CH}_3\text{NH}_3\text{Br}$  was introduced, the time it took for each nanocrystal to turn on varied. These two features of the single-nanocrystal trajectories are analyzed in more detail below. Furthermore, we used a low irradiance ( $\sim 155 \mu\text{W}\cdot\text{cm}^{-2}$  near the focal plane) to avoid photodamage to the nanocrystals, and our observations did not change when a higher light intensity was used (data not shown here). The combination of abrupt switching in the fluorescence intensity for individual nanocrystals with a wide distribution of waiting times before they start to become bright leads to the slow rise in the integrated intensity over the entire field-of-view.



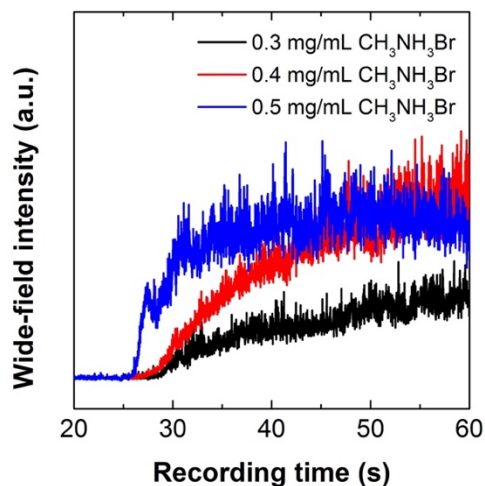


**Figure 4.8.** The integrated fluorescence intensity versus time over the entire field-of-view recorded after injecting CH<sub>3</sub>NH<sub>3</sub>Br into flow cells containing PbBr<sub>2</sub> nanocrystals. The concentration dependence for the transformation averaged over the entire the field-of-view is seen by the sharper rise in fluorescence intensity for higher concentrations of CH<sub>3</sub>NH<sub>3</sub>Br.

### 4.3.3 Statistical Analysis of Single-Particle Fluorescence Trajectory

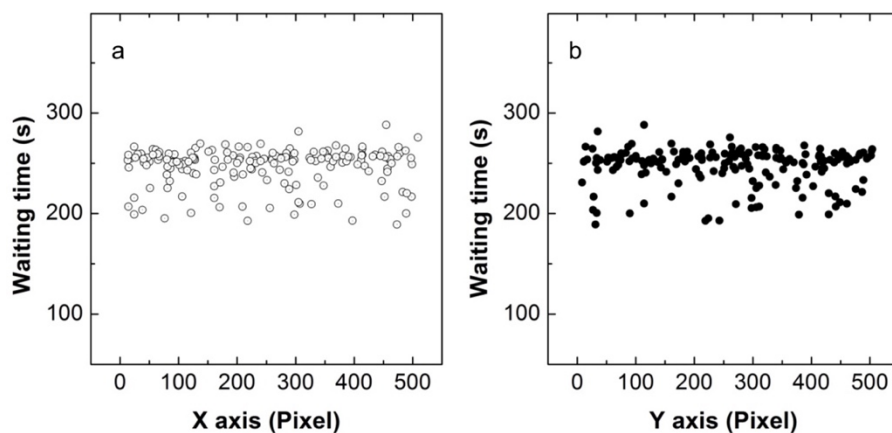


**Figure 4.9.** The waiting times for different nanocrystals within the same field-of-view plotted vs. their location. The abscissa in (a) and (b) correspond to the pixel position of the CCD camera along the x- and y-direction, respectively.

In order to study the reaction kinetics of this conversion reaction, first we have to minimize the effect of reactant diffusion on the statistics of the time points at which a nanocrystal becomes bright. In another words, the time point at which a nanocrystal becomes bright should not

depend on location of the nanocrystal in the field-of-view. **Figure 4.9** shows the relation between the position of different individual nanocrystals within the same field-of-view and their measured waiting time. The locations of the nanocrystals are represented by the pixel positions of the CCD camera along the x- (**Figure 4.9a**) and y-direction (**Figure 4.9b**), respectively. The injection rate was 5 mL/h, which was the typical injection rate used throughout the experiments. As shown in these plots, there is no obvious correlation between the waiting times of individual nanocrystals and their locations. Therefore, we exclude the diffusion of  $\text{CH}_3\text{NH}_3\text{Br}$  across the field-of-view as being responsible for the distribution of waiting times observed in our experiments.

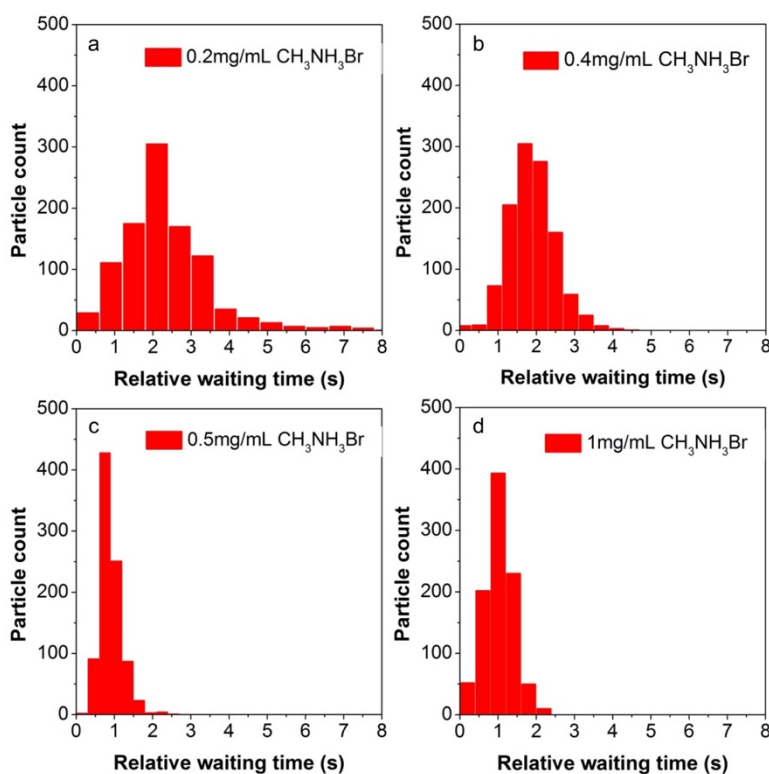


**Figure 4.10.** Histograms of the relative waiting times for  $\text{PbBr}_2$  nanocrystals to transform into  $\text{CH}_3\text{NH}_3\text{PbBr}_3$  when the concentration of  $\text{CH}_3\text{NH}_3\text{Br}$  was (a) 0.2 mg/mL, (b) 0.4 mg/mL, (c) 0.5 mg/mL, and (d) 1.0 mg/mL  $\text{CH}_3\text{NH}_3\text{Br}$ . For each histogram, a relative waiting time of 0 seconds corresponds to the first nanocrystal to transform among the population. The **Experimental Details 4.2.5** describes how histograms were aligned when multiple videos were recorded at the same concentration.

To quantify differences in behavior of individual nanocrystals, we define the waiting time as the time it takes for the intensity of a single nanocrystals to reach a value above a threshold intensity once the  $\text{CH}_3\text{NH}_3\text{Br}$  solution has been added (see **Experimental Details 4.2.5** for further details). Since it is experimentally difficult to know when the  $\text{CH}_3\text{NH}_3\text{Br}$  solution reaches the field-of-view, the waiting time for each nanocrystal was measured relative to the time the first nanocrystal was observed to turn on. The relative waiting times for hundreds of nanocrystals at different concentrations of  $\text{CH}_3\text{NH}_3\text{Br}$  ranging from 0.2 to 1.0 mg/mL in ODE/tert-butanol are plotted in **Figure 4.10**. When the concentration of  $\text{CH}_3\text{NH}_3\text{Br}$  was lower than 0.2 mg/mL, we did not observe transformation of the nanocrystals.  $\text{CH}_3\text{NH}_3\text{Br}$  was not soluble in the ODE/tert-butanol solution at concentrations greater than 1.0 mg/mL. These histograms show that the distributions of waiting times become narrower as the concentration of  $\text{CH}_3\text{NH}_3\text{Br}$  increases. Furthermore, at higher concentrations of  $\text{CH}_3\text{NH}_3\text{Br}$ , the distributions shift towards shorter waiting times, reflecting faster ensemble kinetics. Gaussian fits to the histograms are shown in **Figure 4.11**.

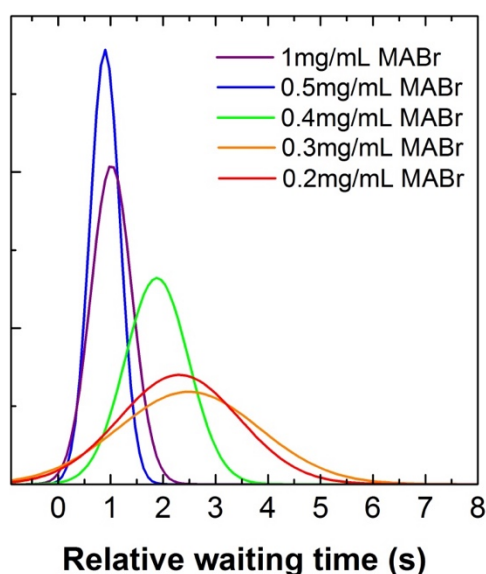


**Figure 4.11.** Fittings of distributions of waiting times shown in **Figure 4.10** at different concentrations of  $\text{CH}_3\text{NH}_3\text{Br}$  to Gaussian distributions.

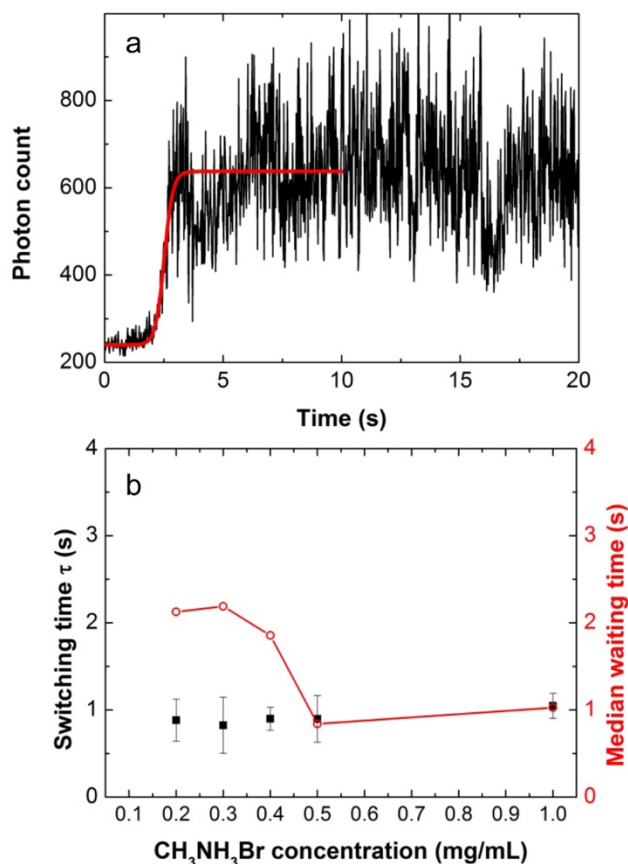


**Figure 4.12.** (a) Representative intensity trajectory (black trace) for a single nanocrystal and the fitting (red line) of the intensity rise to a sigmoidal function. This fitting was used to determine the switching time,  $\tau$ . (b) The average switching time (black squares) and the median relative waiting time (red circles) for the conversion of  $\text{PbBr}_2$  nanocrystals using different  $\text{CH}_3\text{NH}_3\text{Br}$  concentrations. The error bars for the average switching times correspond to one standard deviation.

We next characterized the sharpness of the intensity rise for individual nanocrystals and its dependence on the  $\text{CH}_3\text{NH}_3\text{Br}$  concentration. The increase in intensity for each nanocrystal was fit to a sigmoidal function, and a switching time,  $\tau$ , was extracted from this fit (see **Figure 4.12a**). A sharper rise in intensity will lead to a smaller value of  $\tau$  (see the **Experimental Details 4.2.5** for further details). The average switching times are plotted as a function of  $\text{CH}_3\text{NH}_3\text{Br}$  concentration in **Figure 4.12b** along with the median relative waiting times at the

same concentrations. The average switching times are insensitive to the  $\text{CH}_3\text{NH}_3\text{Br}$  concentration (**Figure 4.12b**), while the distributions of waiting times become narrower and shifts towards shorter waiting times for higher concentrations of  $\text{CH}_3\text{NH}_3\text{Br}$  (see **Figure 4.10** and **Figure 4.11**). Thus, the median waiting time decreases with increasing  $\text{CH}_3\text{NH}_3\text{Br}$  concentration until it becomes dominated by the switching time. The short time scale of the switching time for individual nanocrystals relative to the ensemble intensity rise and its independence from reactant concentration appear to be characteristic features for this solid-state reaction.

#### 4.3.4 Phase Transformation Model for Conversion via Monte Carlo Simulations

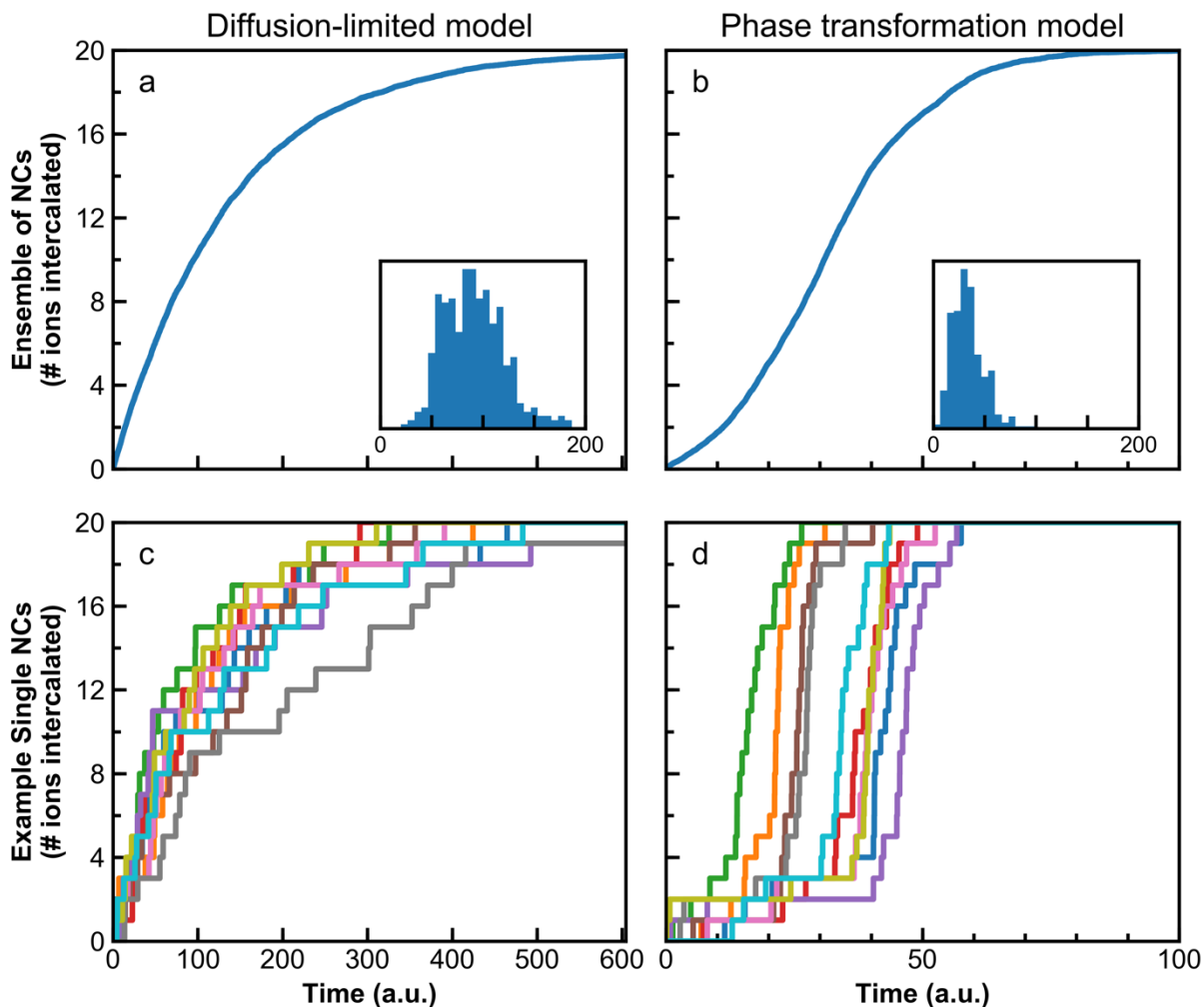


**Figure 4.13.** Monte Carlo simulations of ion intercalation in PbBr<sub>2</sub> nanocrystals. Ensemble reaction trajectories for the (a) diffusion-limited and (b) phase-transformation models described in the text. The insets show histograms of the waiting times for individual trajectories using these models. Representative single-particle trajectories for the (c) diffusion-limited and (d) phase-transformation models.

We used Monte Carlo methods to simulate the kinetics of ion intercalation (i.e., CH<sub>3</sub>NH<sub>3</sub><sup>+</sup> and Br<sup>-</sup>) into PbBr<sub>2</sub> nanocrystals and their transformation to CH<sub>3</sub>NH<sub>3</sub>PbBr<sub>3</sub>. These simulations

involve the discrete time evolution of an ensemble of nanocrystals in the presence of a reservoir of external ions. At each time step, the probability for successful intercalation in a randomly chosen particle depends upon the free energy change,  $\Delta G_i$ , associated with the  $i^{\text{th}}$  intercalation event for that particle. The dependence of the free energy and corresponding probability on the number of previous intercalation events that have taken place in the particle are varied to simulate different models for the transformation of the nanocrystal. The results for two of these models are shown in **Figure 4.13**, which include the ensemble-averaged and representative single-particle trajectories for ion intercalation along with insets showing the distributions of simulated waiting times. In the diffusion-limited model,  $\Delta G_i$  for each intercalation event is assumed to be governed by solid-state diffusion and is constant throughout the simulation (**Figure 4.13a, c**). This model produces switching times for single nanocrystals that occur on the same time scale as the corresponding ensemble trajectory, which is not observed experimentally. Additionally, all of the trajectories in the diffusion-limited simulations show a negative curvature at all times whereas the experimental trajectories start with a positive curvature before reaching a knee curve.

The model shown in **Figure 4.13b, d** incorporates the reconstructive transitions that are necessary due to the different arrangements of  $\text{Pb}^{2+}$  and  $\text{Br}^-$  ions in the initial and final crystals. The  $\text{Pb}^{2+}$  ions in  $\text{PbBr}_2$  possess a buckled arrangement (similar to phosphorene) when viewed along the  $[010]$  direction. The  $\text{PbBr}_7$  heptahedra in  $\text{PbBr}_2$  are both edge and corner sharing. In  $\text{CH}_3\text{NH}_3\text{PbBr}_3$  the  $\text{PbBr}_6$  octahedra are connected via corner sharing to give a  $\text{Pb}^{2+}$  sublattice with a simple cubic arrangement. To model the conversion between these two crystals, ion intercalation is assumed to be diffusion-limited until a critical point after which the perovskite phase is adopted. After the phase transformation, the presence of many  $\text{CH}_3\text{NH}_3^+$  and  $\text{Br}^-$  vacancy sites in the perovskite structure is expected to favor additional ion intercalation. In our

simulations for this phase-transformation model,  $\Delta G_i$  and the associated probability for each ion intercalation events are initially constant. After a critical number of successful events has occurred for a given particle, the value of  $\Delta G_i$  for further intercalation progressively decreases. The simulations resulting from this phase-transformation model reproduce several features of the experimental fluorescence trajectories. Abrupt changes in the number of ions incorporated lead to switching times for individual trajectories that occur on a shorter time scale than the ensemble trajectory. The simulated trajectories also have the same general curvature profile as the experimental results.

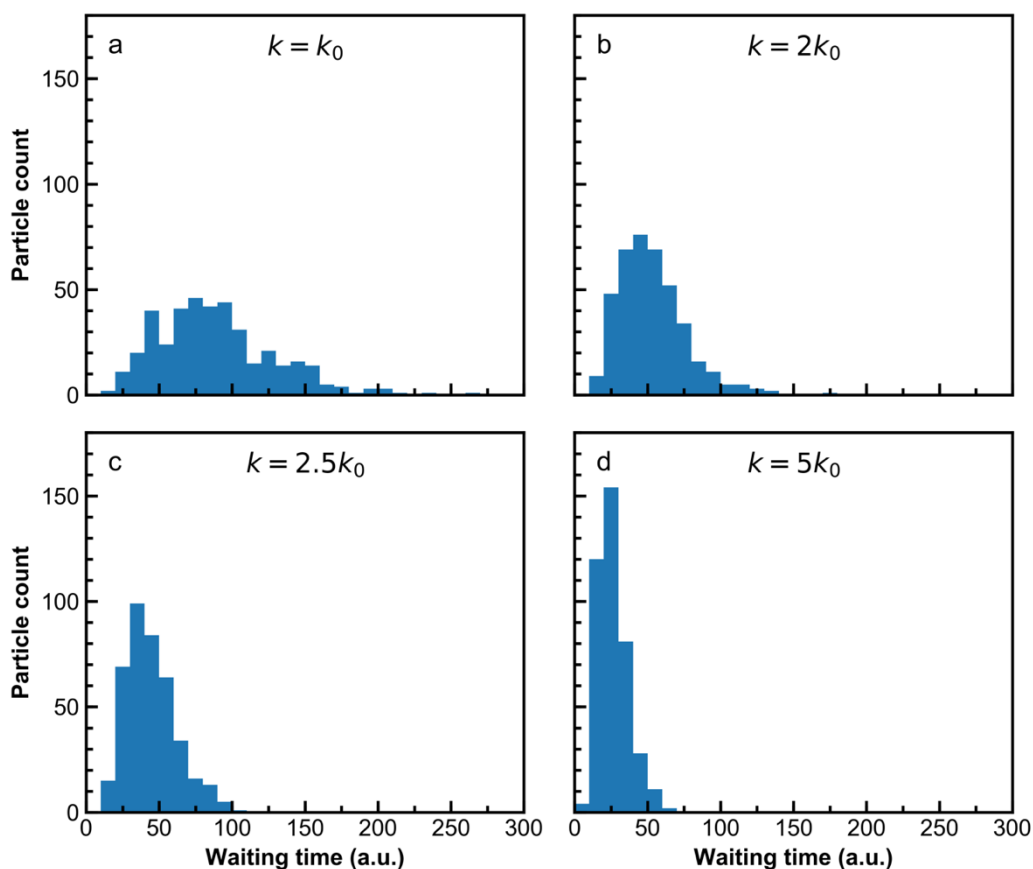


**Figure 4.14.** Histograms of waiting times for various initial equilibrium constants that correspond to varied ion concentrations. The equilibrium constant increases from panels (a) to (d) by the same factors as the  $\text{CH}_3\text{NH}_3\text{Br}$  concentration in the experimental data in **Figure 4.10**. The simulation model used for these plots is the phase transformation model.



**Figure 4.14** shows histograms of the waiting times from simulations with different initial equilibrium constants using the phase-transformation model. Varying the equilibrium constant for ion intercalation in the simulations corresponds to changing the concentration of the  $\text{CH}_3\text{NH}_3\text{Br}$  solution. Comparing the experimental histograms of the waiting times in **Figure 4.10** with the simulated ones in **Figure 4.14**, both show similar decreases in the medians and the widths of the waiting time distributions with increasing reactant concentration.

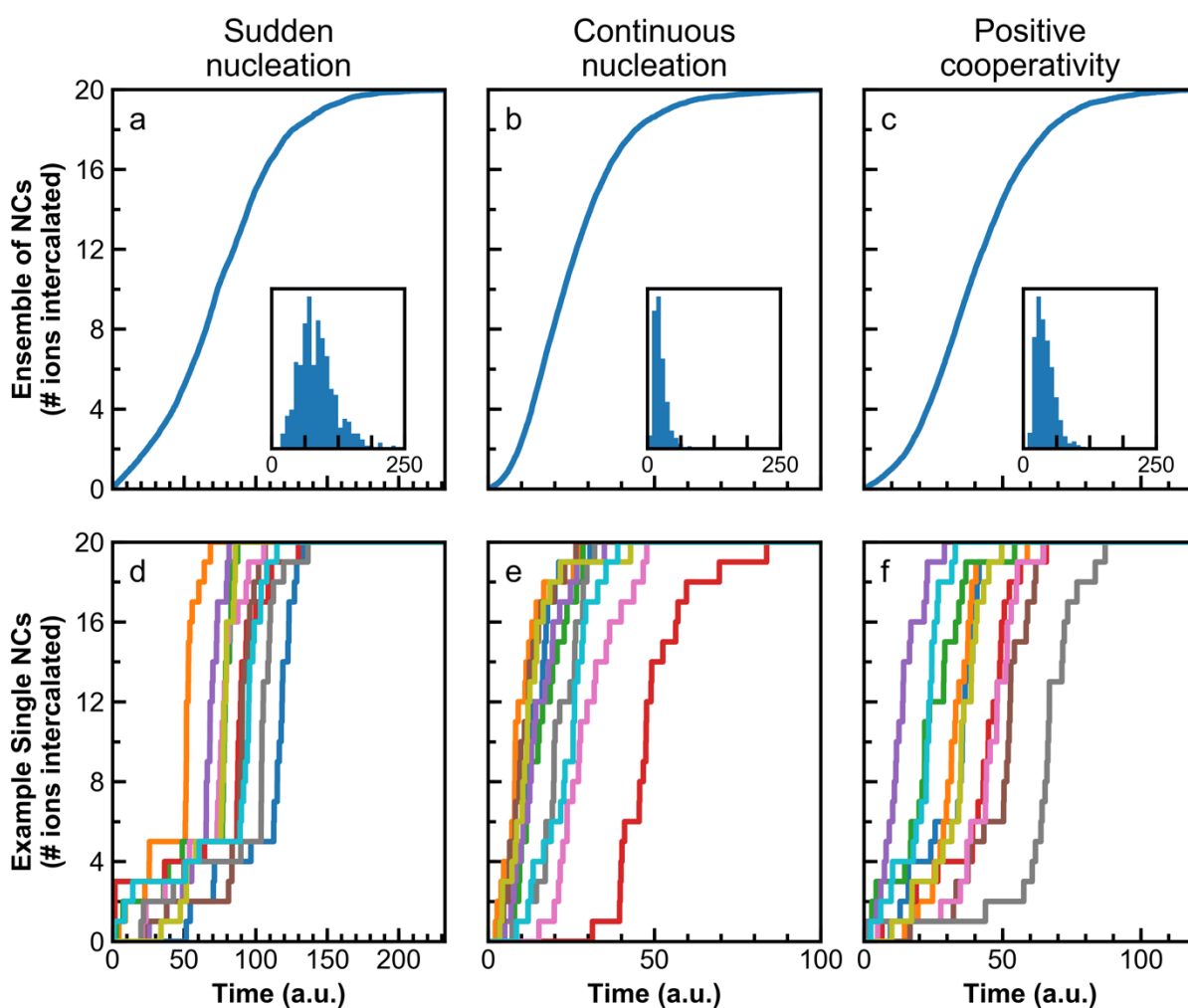


**Figure 4.15.** Ensemble and individual intercalation trajectories for three additional models. (a), (b), and (c) show ensemble trajectories for the labeled models with waiting time histograms inset. (d), (e), and (f) show example individual trajectories for the same three models.

We investigated other models to simulate the abrupt switching times observed for individual nanocrystals. **Figure 4.15** shows the ensemble trajectories, representative single-particle trajectories, and histograms of waiting times for three additional models that exhibit different degrees of cooperativity between intercalation events. The key feature of each of these models is that the probability for successive intercalation events for a particle increases (either continuously or abruptly) over the course of the trajectory (see **Experimental Details 4.2.6** for more information on these models). One of these models was originally proposed by Routzahn and Jain to describe cation exchange in CdSe nanocrystals with  $\text{Ag}^+$ .<sup>13</sup> In this positive-cooperativity model, the activation energy for each exchange event decreases linearly with the number of successful events, such that the probability for exchange increases exponentially during the simulation. All three reaction models exhibit abrupt jumps in the number of ions incorporated for individual particles that simulate the sharp changes in fluorescence intensity observed experimentally. They also show a distribution of waiting times such that the corresponding ensemble trajectory occurs over a longer time scale than the individual trajectories.

### 4.3.5 Comparison of Ion Intercalation and Cation Exchange

Previously, Routzahn and Jain studied the interconversion between CdSe and  $\text{Ag}_2\text{Se}$  nanocrystals via cation exchange using single-nanocrystal fluorescence microscopy (CdSe is fluorescent while  $\text{Ag}_2\text{Se}$  is non-fluorescent under visible excitation).<sup>13-14</sup> Similar to our observations, the distribution of waiting times for fluorescent CdSe nanocrystals to turn off during cation exchange with  $\text{Ag}^+$  narrowed as the concentration of  $\text{AgNO}_3$  was increased. Furthermore, the average switching times were insensitive to  $\text{Ag}^+$  concentration. However, the

average switching times for fluorescence decay in CdSe to Ag<sub>2</sub>Se conversion (determined via similar sigmoidal fitting to that shown in **Figure 4.12a**) were significantly shorter than our switching times (on the order of hundreds of milliseconds). We note that while changes in fluorescence intensity provide a signature for these reactions, there is not a one-to-one correspondence between the start of the reaction and the point at which the fluorescence intensity starts to rise or fall. For example, it has been shown that interstitial Ag<sup>+</sup> ions in CdSe nanocrystals significantly lower the quantum yield of the nanocrystals.<sup>11</sup> Thus, the fluorescence turn-off during cation exchange of a CdSe nanocrystal with Ag<sup>+</sup> may occur at an early time point during the reaction. Consistent with this picture, the switching times for fluorescence turn-on are longer when Ag<sub>2</sub>Se nanocrystals are converted back to CdSe. Similarly, defects reduce the emission intensity in films of CH<sub>3</sub>NH<sub>3</sub>PbI<sub>3</sub>.<sup>33</sup> Thus, during the intercalation of CH<sub>3</sub>NH<sub>3</sub><sup>+</sup> and Br<sup>-</sup> ions into the PbBr<sub>2</sub> lattice, the nanocrystals may not start to emit until structural defects that quench fluorescence have been annealed.

Both cation exchange in chalcogenide nanocrystals and ion intercalation in lead halide nanocrystals can be described by a model in which the successive ion exchange/intercalation events become more favorable as the reaction proceeds. We hypothesize that the reason these two systems exhibit similar behavior arises from the solid-state immiscibility between the initial and final crystals. In cation exchange, the chalcogenide sublattice must also undergo significant rearrangements to accommodate the entering cations. The selenium ions have a hexagonal arrangement in CdSe while they possess an orthorhombic arrangement in Ag<sub>2</sub>Se.<sup>6</sup> The immiscibility between the initial and final crystals requires the new phase to first nucleate within the crystal. In the nanoscale crystals studied here a single nucleation event likely takes place in each crystal.<sup>34</sup> Our simulations support an initially large activation barrier for this nucleation event, followed by a decrease in activation barrier once nucleation has occurred. Furthermore,

this model suggests that solid-state reactions in which there is high miscibility between the initial and final crystals should exhibit different behavior. Routzahn and Jain proposed cation exchange of CdSe nanocrystals with  $\text{Hg}^{2+}$  as one such system that exhibits high miscibility between CdSe and HgSe.<sup>10, 13</sup> Similarly, during anion exchange of lead-halide perovskites, the  $\text{Pb}^{2+}$  cations undergo relatively small rearrangements to accommodate halide ions ( $\text{Cl}^-$ ,  $\text{Br}^-$  or  $\text{I}^-$ ) of different sizes.<sup>4-5, 35</sup> We expect that both the waiting and switching times for anion exchange will depend on halide concentration. We are currently extending our single-nanocrystal fluorescence measurements to study anion exchange in cesium lead halide system. Our preliminary results are shown in **Chapter 5**.

## 4.4 Conclusions

Using fluorescence microscopy, we imaged the conversion of  $\text{PbBr}_2$  nanocrystals to  $\text{CH}_3\text{NH}_3\text{PbBr}_3$  at the single-nanocrystal level. The nanocrystals exhibit a characteristic switching time for this reaction that is insensitive to the reactant concentration. A distribution of waiting times before each nanocrystal becomes bright leads to ensemble kinetics that are concentration dependent and much slower than the abrupt transitions observed for single nanocrystals. To account for these observations, we developed a phase-transformation model that incorporates a discontinuous change in probability for ion intercalation associated with stabilizing the perovskite phase before the reaction becomes favorable. This study shows that by imaging solid-state transformations in individual nanoscale crystallites, one can obtain information that is masked in the ensemble kinetics. Notably, when the overall reaction is 50% complete, the ensemble of nanocrystals consists of two populations; half of the nanocrystals are fully transformed while the other half have not yet reacted. Tracking nanoscale chemistry with

single-particle fluorescence can be applied to other reactions where there is either a change in the brightness or the spectral position of the emission from the nanocrystal, such as oxidation and ligand exchange.<sup>36-37</sup>

## **4.5 Acknowledgements**

I would like to thank Mr. John Cavin and Professor Rohan Mishra to help me do the Monte Carlo simulation of different reaction models. Also I would thank my colleague Mr. Dong Wang for discussion and assistance of this project and Mr. Daniel Khan for help with the data analysis. Thank Dr. Brian Wieliczka and Professor Richard Loomis for use of their absorption spectrometer.

## 4.6 References

1. Ko, H.; Sin, D. H.; Kim, M.; Cho, K., Predicting the morphology of perovskite thin films produced by sequential deposition method: a crystal growth dynamics study, *Chem. Mater.* **2017**, *29*, 1165-1174.
2. Ahmad, S.; Kanaujia, P. K.; Niu, W.; Baumberg, J. J.; Vijaya Prakash, G., In situ intercalation dynamics in inorganic–organic layered perovskite thin films, *ACS Appl. Mater. Interfaces* **2014**, *6*, 10238-10247.
3. Chen, C.-C.; Herhold, A. B.; Johnson, C. S.; Alivisatos, A. P., Size dependence of structural metastability in semiconductor nanocrystals, *Science* **1997**, *276*, 398-401.
4. Nedelcu, G.; Protesescu, L.; Yakunin, S.; Bodnarchuk, M. I.; Grotevent, M. J.; Kovalenko, M. V., Fast anion-exchange in highly luminescent nanocrystals of cesium lead halide perovskites (CsPbX<sub>3</sub>, X = Cl, Br, I), *Nano Lett.* **2015**, *15*, 5635-5640.
5. Jang, D. M.; Park, K.; Kim, D. H.; Park, J.; Shojaei, F.; Kang, H. S.; Ahn, J.-P.; Lee, J. W.; Song, J. K., Reversible halide exchange reaction of organometal trihalide perovskite colloidal nanocrystals for full-range band gap tuning, *Nano Lett.* **2015**, *15*, 5191-5199.
6. Son, D. H.; Hughes, S. M.; Yin, Y.; Paul Alivisatos, A., Cation exchange reactions in ionic nanocrystals, *Science* **2004**, *306*, 1009-1012.
7. Robinson, R. D.; Sadtler, B.; Demchenko, D. O.; Erdonmez, C. K.; Wang, L.-W.; Alivisatos, A. P., Spontaneous superlattice formation in nanorods through partial cation exchange, *Science* **2007**, *317*, 355-358.

8. Chan, E. M.; Marcus, M. A.; Fakra, S.; ElNaggar, M.; Mathies, R. A.; Alivisatos, A. P., Millisecond kinetics of nanocrystal cation exchange using microfluidic X-Ray absorption spectroscopy, *J. Phys. Chem. A* **2007**, *111*, 12210-12215.
9. Sadtler, B.; Demchenko, D. O.; Zheng, H.; Hughes, S. M.; Merkle, M. G.; Dahmen, U.; Wang, L. W.; Alivisatos, A. P., Selective facet reactivity during cation exchange in cadmium sulfide nanorods, *J. Am. Chem. Soc.* **2009**, *131*, 5285-5293.
10. Smith, A. M.; Nie, S., Bright and compact alloyed quantum dots with broadly tunable near-infrared absorption and fluorescence spectra through mercury cation exchange, *J. Am. Chem. Soc.* **2011**, *133*, 24-26.
11. Jain, P. K.; Beberwyck, B. J.; Fong, L.-K.; Polking, M. J.; Alivisatos, A. P., Highly luminescent nanocrystals from removal of impurity atoms residual from ion-exchange synthesis, *Angew. Chem. Int. Ed.* **2012**, *51*, 2387-2390.
12. White, S. L.; Smith, J. G.; Behl, M.; Jain, P. K., Co-operativity in a nanocrystalline solid-state transition, *Nat. Commun.* **2013**, *4*, 2933.
13. Routzahn, A. L.; Jain, P. K., Single-nanocrystal reaction trajectories reveal sharp cooperative transitions, *Nano Lett.* **2014**, *14*, 987-992.
14. Routzahn, A. L.; Jain, P. K., Luminescence blinking of a reacting quantum dot, *Nano Lett.* **2015**, *15*, 2504-2509.
15. Tachikawa, T.; Karimata, I.; Kobori, Y., Surface charge trapping in organolead halide perovskites explored by single-particle photoluminescence imaging, *J. Phys. Chem. Lett.* **2015**, *6*, 3195-3201.

16. Empedocles, S. A.; Norris, D. J.; Bawendi, M. G., Photoluminescence spectroscopy of single CdSe nanocrystallite quantum dots, *Phys. Rev. Lett.* **1996**, *77*, 3873-3876.
17. Empedocles, S. A.; Neuhauser, R.; Bawendi, M. G., Three-dimensional orientation measurements of symmetric single chromophores using polarization microscopy, *Nature* **1999**, *399*, 126-130.
18. Xu, W.; Kong, J. S.; Yeh, Y.-T. E.; Chen, P., Single-Molecule Nanocatalysis reveals heterogeneous reaction pathways and catalytic dynamics, *Nat. Mater.* **2008**, *7*, 992-996.
19. Zhou, X.; Andoy, N. M.; Liu, G.; Choudhary, E.; Han, K.-S.; Shen, H.; Chen, P., quantitative super-resolution imaging uncovers reactivity patterns on single nanocatalysts, *Nat. Nanotechnol.* **2012**, *7*, 237-241.
20. Galland, C.; Ghosh, Y.; Steinbrück, A.; Sykora, M.; Hollingsworth, J. A.; Klimov, V. I.; Htoon, H., Two types of luminescence blinking revealed by spectroelectrochemistry of single quantum dots, *Nature* **2011**, *479*, 203-207.
21. Orfield, N. J.; McBride, J. R.; Keene, J. D.; Davis, L. M.; Rosenthal, S. J., Correlation of atomic structure and photoluminescence of the same quantum dot: pinpointing surface and internal defects that inhibit photoluminescence, *ACS Nano* **2015**, *9*, 831-839.
22. Orfield, N. J.; Majumder, S.; McBride, J. R.; Yik-Ching Koh, F.; Singh, A.; Bouquin, S. J.; Casson, J. L.; Johnson, A. D.; Sun, L.; Li, X.; Shih, C.-K.; Rosenthal, S. J.; Hollingsworth, J. A.; Htoon, H., Photophysics of thermally-assisted photobleaching in “Giant” quantum dots revealed in single nanocrystals, *ACS Nano* **2018**, *12*, 4206-4217.



23. Brenner, T. M.; Rakita, Y.; Orr, Y.; Klein, E.; Feldman, I.; Elbaum, M.; Cahen, D.; Hodes, G., Conversion of single crystalline  $\text{PbI}_2$  to  $\text{CH}_3\text{NH}_3\text{PbI}_3$ : structural relations and transformation dynamics, *Chem. Mater.* **2016**, *28*, 6501-6510.
24. Hassan, Y.; Song, Y.; Pensack, R. D.; Abdelrahman, A. I.; Kobayashi, Y.; Winnik, M. A.; Scholes, G. D., Structure-tuned lead halide perovskite nanocrystals, *Adv. Mater.* **2016**, *28*, 566-573.
25. Lee, M. M.; Teuscher, J.; Miyasaka, T.; Murakami, T. N.; Snaith, H. J., Efficient hybrid solar cells based on meso-superstructured organometal halide perovskites, *Science* **2012**, *338*, 643-647.
26. Naumkin, A. V.; Kraut-Vass, A.; Powell, C. J.; Gaarenstroom, S. W.; National Institute of Standards and Technology, NIST X-Ray Photoelectron Spectroscopy Database, **2012**.
27. Fu, Y.; Meng, F.; Rowley, M. B.; Thompson, B. J.; Shearer, M. J.; Ma, D.; Hamers, R. J.; Wright, J. C.; Jin, S., Solution growth of single crystal methylammonium lead halide perovskite nanostructures for optoelectronic and photovoltaic applications, *J. Am. Chem. Soc.* **2015**, *137*, 5810-5818.
28. Edri, E.; Kirmayer, S.; Cahen, D.; Hodes, G., High open-circuit voltage solar cells based on organic–inorganic lead bromide perovskite, *J. Phys. Chem. Lett.* **2013**, *4*, 897-902.
29. Choi, J. J.; Yang, X.; Norman, Z. M.; Billinge, S. J. L.; Owen, J. S., Structure of methylammonium lead iodide within mesoporous titanium dioxide: active material in high-performance perovskite solar cells, *Nano Lett.* **2014**, *14*, 127-133.

30. Zhu, F.; Men, L.; Guo, Y.; Zhu, Q.; Bhattacharjee, U.; Goodwin, P. M.; Petrich, J. W.; Smith, E. A.; Vela, J., Shape evolution and single particle luminescence of organometal halide perovskite nanocrystals, *ACS Nano* **2015**, *9*, 2948-2959.
31. Karimata, I.; Kobori, Y.; Tachikawa, T., Direct observation of charge collection at nanometer-scale iodide-rich perovskites during halide exchange reaction on  $\text{CH}_3\text{NH}_3\text{PbBr}_3$ , *J. Phys. Chem. Lett.* **2017**, *8*, 1724-1728.
32. Schmidt, L. C.; Pertegás, A.; González-Carrero, S.; Malinkiewicz, O.; Agouram, S.; Mínguez Espallargas, G.; Bolink, H. J.; Galian, R. E.; Pérez-Prieto, J., Nontemplate synthesis of  $\text{CH}_3\text{NH}_3\text{PbBr}_3$  perovskite nanoparticles, *J. Am. Chem. Soc.* **2014**, *136*, 850-853.
33. de Quilettes, D. W.; Vorpahl, S. M.; Stranks, S. D.; Nagaoka, H.; Eperon, G. E.; Ziffer, M. E.; Snaith, H. J.; Ginger, D. S., Impact of microstructure on local carrier lifetime in perovskite solar cells, *Science* **2015**, *348*, 683-686.
34. Jacobs, K.; Zaziski, D.; Scher, E. C.; Herhold, A. B.; Paul Alivisatos, A., Activation volumes for solid-solid transformations in nanocrystals, *Science* **2001**, *293*, 1803-1806.
35. Pellet, N.; Teuscher, J.; Maier, J.; Grätzel, M., Transforming hybrid organic inorganic perovskites by rapid halide exchange, *Chem. Mater.* **2015**, *27*, 2181-2188.
36. Yin, B.; Sadtler, B.; Berezin, M. Y.; Thimsen, E., Quantum dots protected from oxidative attack using alumina shells synthesized by atomic layer deposition, *Chem. Commun.* **2016**, *52*, 11127-11130.
37. deQuilettes, D. W.; Koch, S.; Burke, S.; Paranjli, R. K.; Shropshire, A. J.; Ziffer, M. E.; Ginger, D. S., Photoluminescence lifetimes exceeding 8 ms and quantum yields

exceeding 30% in hybrid perovskite thin films by ligand passivation, *ACS Energy Lett.*  
**2016**, *1*, 438-444.

## **Chapter 5**

### **Conclusions and Future Studies**

## 5.1 Conclusions

In this dissertation, we explored employing defect chemistry by introducing twin defects to control the morphology of ternary silver halide ( $\text{AgBr}_{1-x}\text{I}_x$ ) nanocrystals. We also studied the reaction dynamics of ion intercalation during the solid-state transformation from single lead bromide ( $\text{PbBr}_2$ ) nanocrystals and  $\text{PbI}_2$  microcrystals to methylammonium lead bromide ( $\text{CH}_3\text{NH}_3\text{PbBr}_3$ ) and  $\text{CH}_3\text{NH}_3\text{PbI}_3$  perovskite with fluorescence microscopy.

There are two systems we are focusing in this dissertation, silver halide and lead halide perovskite. Besides the difference of material system, there are several other differences between these two reactions we have studied. Firstly, in ternary silver halide nanocrystals a certain ratio of bromide ion positions are being replaced by iodide ions but not by anion exchange. The rock salt phase of ternary  $\text{AgBr}_{1-x}\text{I}_x$  is the same as  $\text{AgBr}$  crystals. While for the conversion of  $\text{PbBr}_2$  nanocrystals it is an ion intercalation reaction during which a new phase  $\text{CH}_3\text{NH}_3\text{PbBr}_3$  is produced. Secondly, which I think is more important, we directly synthesized the ternary  $\text{AgBr}_{1-x}\text{I}_x$  nanocrystals with the desired bromide to iodide ratio in the precursors. However, the solid-state conversion of  $\text{PbBr}_2$  nanocrystals is a post-synthesis method to make our desirable product.

On the other hand, there are also a lot of similarity between the two reactions. For start, these two systems are both metal halide. The interchangeable feature between different anions and unique dynamics of intercalation are related to halide group, which has a lot of applications and interesting properties. Secondly, which I think is very interesting, in both reactions structural miscibility plays a crucial role. In the case of ternary  $\text{AgBr}_{1-x}\text{I}_x$  nanocrystal, the difference between the crystal structures of  $\text{AgI}$  (hexagonal close-packed) and  $\text{AgBr}$  (face-center-cubic) limits the amounts of bromide ions that can be replaced by iodide ions without

phase segregation. This structural miscibility between AgI and AgBr also induces the twin defects on the {111} crystal facets during nucleation, which eventually leads to the morphology of hexagonal prism. For the conversion of PbBr<sub>2</sub> nanocrystals, it is also the structural miscibility between PbBr<sub>2</sub> and CH<sub>3</sub>NH<sub>3</sub>PbBr<sub>3</sub> that leads to the sudden phase transition from one to the other. This phase transition is related to the sharp change of fluorescence intensity in trajectories of single nanocrystal. This structural miscibility involving halide group offers a lot of interesting properties in semiconductor metal halide nanocrystals.

## 5.2 Preliminary Results of Anion Exchange from Cl<sup>-</sup> to Br<sup>-</sup> in Cesium Lead Halide Nanocrystals

My colleague, Dong Wang, has already tried to image halide anion exchange in the cesium lead halide perovskite system. This demonstrates that this technique of single nanocrystal fluorescence microscopy can be applied to this system. The preliminary results of anion exchange from Cl<sup>-</sup> to Br<sup>-</sup> in cesium lead halide system are given in **Figure 5.1 a**. The average switching time of this anion exchange decreases exponentially with increasing tetrabutylammonium bromide (TBAB, C<sub>16</sub>H<sub>36</sub>BrN) concentrations. **Figure 5.1 b** shows the switching time of conversion from PbBr<sub>2</sub> nanocrystals to CH<sub>3</sub>NH<sub>3</sub>PbBr<sub>3</sub> does not respond to varying TBAB concentrations. (Data is also shown in **Figure 4.12**.) Comparing **Figure 5.1 b** with **Figure 5.1 a**, it shows that the average switching time behaves differently between conversion from PbBr<sub>2</sub> to CH<sub>3</sub>NH<sub>3</sub>PbBr<sub>3</sub> nanocrystals and anion exchange reaction from CsPbCl<sub>3</sub> to CsPbBr<sub>3</sub> nanocrystal. First of all, from the range of TBAB concentration, anion exchange reaction starts at a much lower concentration, even at 1 μg/mL. While the lowest concentration we measured for the conversion from PbBr<sub>2</sub> to CH<sub>3</sub>NH<sub>3</sub>PbBr<sub>3</sub> is 200 μg/mL below

which the intercalation does not happen. Secondly, anion exchange from CsPbCl<sub>3</sub> to CsPbBr<sub>3</sub> is a TBAB concentration dependent reaction. However, in the conversion from PbBr<sub>2</sub> to CH<sub>3</sub>NH<sub>3</sub>PbBr<sub>3</sub> nanocrystals, the average switching time does not respond to changes in CH<sub>3</sub>NH<sub>3</sub>Br concentration.

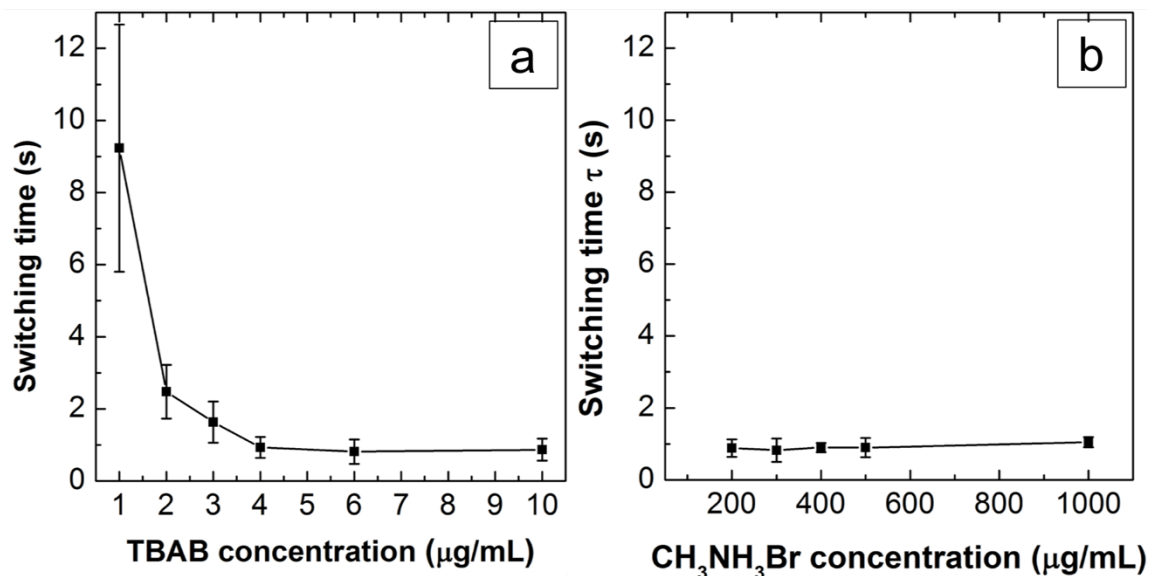


**Figure 5.1** Average switching time of (a) anion exchange from CsPbCl<sub>3</sub> to CsPbBr<sub>3</sub> nanocrystals with different TBAB concentrations and (b) ion intercalation conversion from PbBr<sub>2</sub> nanocrystals to CH<sub>3</sub>NH<sub>3</sub>PbBr<sub>3</sub> with different CH<sub>3</sub>NH<sub>3</sub>Br concentrations. The error bars for the average switching time correspond to one standard deviation.

This observation is consistent with our hypothesis that the sudden change of fluorescence intensity for trajectories of single nanocrystals is indicative of the phase transition due to the structural immiscibility between the initial and final crystals. In both reactions, the final products are bromide perovskite nanocrystals. The orthorhombic structure of PbBr<sub>2</sub> is so different from perovskite structure of CH<sub>3</sub>NH<sub>3</sub>PbBr<sub>3</sub>. In order for the conversion to happen, a phase change must occur at certain point. The time point when the crystal goes through this phase transition does not depend on the CH<sub>3</sub>NH<sub>3</sub>Br concentration in solution. However, the structures between CsPbCl<sub>3</sub> and CsPbBr<sub>3</sub> are very similar. The structure does not go through

significant change during anion exchange. Therefore, this anion exchange reaction involves diffusion of  $\text{Br}^-$  into the crystal lattice and  $\text{Cl}^-$  diffusion out. Diffusion is a concentration dependent process. The preliminary study on anion exchange in cesium lead halide system supports our hypothesis that structural immiscibility between the initial and final crystal is a key factor that affects the transformation behavior of metal halide nanocrystals.

## 5.3 Future Studies

### 5.3.1 Study the Photocatalytic Activity of Different Crystal Facets with $\text{AgBr}_{1-x}\text{I}_x$ Nanocrystals

**Chapter 2** is focusing more on studying the growth mechanism and control of morphology of ternary  $\text{AgBr}_{1-x}\text{I}_x$  nanocrystals. Now two different morphologies, truncated cube and hexagonal prism, have been achieved. We can go ahead and study the difference in photocatalytic activity of ternary  $\text{AgBr}_{1-x}\text{I}_x$  nanocrystals with these two morphologies. As shown in **Chapter 2**,  $\{100\}$  facets dominate in truncated cube morphology, while  $\{111\}$  facets prevail in hexagonal prism. Since the activity of catalyst is facet dependent,<sup>27</sup> we can study the differences in the photocatalytic activity of  $\{100\}$  and  $\{111\}$  facets of  $\text{AgBr}_{1-x}\text{I}_x$  through these two different morphologies.



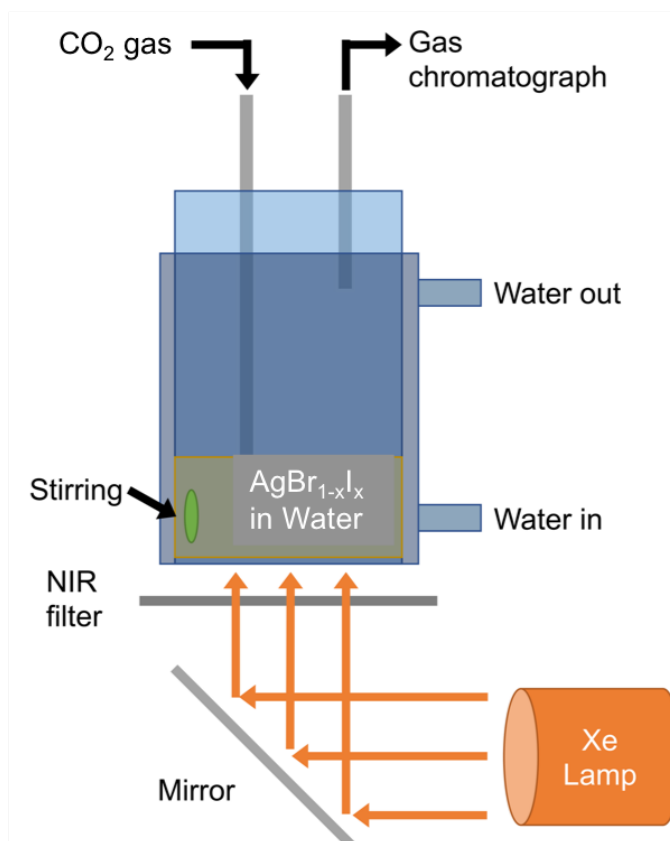


**Figure 5.2** Schematic of possible experimental set-up that can be used to test photocatalytic CO<sub>2</sub> reduction of ternary AgBr<sub>1-x</sub>I<sub>x</sub> nanocrystal. Adapted with permission from (Zhu, W.; Shen, M.; Fan, G.; Yang, A.; Meyer, J. R.; Ou, Y.; Yin, B.; Fortner, J.; Foston, M.; Li, Z.; Zou, Z.; Sadtler, B., Facet-dependent enhancement in the activity of bismuth vanadate microcrystals for the photocatalytic conversion of methane to methanol, *ACS Appl. Nano. Mater.* **2018**, 1, 12, 6683-6691.). Copyright (2018) American Chemical Society.

A schematic of an experimental configuration to measure photocatalytic activity is shown in **Figure 5.2**. There have been several reports that under irradiation with a Xe lamp silver halide can reduce CO<sub>2</sub> to organic fuel such as methanol or ethanol.<sup>1-5</sup> Therefore, this would be a good photocatalytic reaction to study the activity in different crystal facets of ternary AgBr<sub>1-x</sub>I<sub>x</sub>. Organic dye degradation (such as methylene orange or blue) is another photocatalytic reaction that can be used to study the photocatalytic activity of this system. Experimental details of this reaction can be found in several previous studies.<sup>5-12</sup>

### 5.3.2 Study of Single Nanocrystal Photoluminescence (PL) Change with Fluorescence Microscopy

Single nanocrystal fluorescence microscopy was demonstrated using lead bromide nanocrystals as an example. However single nanocrystal fluorescence microscopy is a very versatile method that can be used in many material systems and situations. For instance, it has already been demonstrated by Routzahn and Jain that single nanocrystal fluorescence microscopy can study the reaction kinetics of CdSe/Ag<sup>+</sup> cation exchange reaction.<sup>13,14</sup> There are other systems, such as CdTe, CdS and cesium lead halide perovskite (CsPbX<sub>3</sub>, X = Cl, Br or I), that single nanocrystal fluorescence microscopy can possibly be employed. There are requirements that need to be satisfied for using this method. In general, single nanocrystal fluorescence microscopy is good at detecting photoluminescence changes. It could be the change either in intensity or the spectral position of emission from the nanocrystal. Of course, for different systems appropriate sets of excitation and emission filters are needed to match the material system in order to image the transformation process.

For cesium lead halide perovskite system (CsPbX<sub>3</sub>, X = Cl, Br, I), it has been shown that anion exchange between Cl<sup>-</sup>, Br<sup>-</sup> and I<sup>-</sup> can be achieved.<sup>15</sup> In this system, transformation between different halide ions changes both the spectral positions of emission and also the emission intensity. Therefore, exchange between different halide ions can be observed with this single nanocrystal fluorescence microscopy technique with appropriate settings and filters.

The influence that different surface passivation can have on photoluminescence of single semiconductor nanocrystals is another area where single nanocrystal fluorescence microscopy can be used. Photoluminescence efficiencies of semiconductor nanocrystals can be affected to a great extent by exchange of surface passivation.<sup>16-18</sup> Although in the work of Buhro's group,

ligand exchange can lead to large shifts in the spectra of quantum-confined 2D nanocrystals, still the shift of the emission spectrum is too small to be detected by this single nanocrystal fluorescence microscopy method.<sup>19-23</sup> However, the surface passivation does greatly affect the quantum yields of the semiconductor nanocrystals. For example, surface passivation of CdSe quantum dots can be reversibly exchanged between neutral-acceptor (Z-type) metal-carboxylate passivation and neutral-donor amine passivation.<sup>19,20</sup> The lowest energy absorption feature shifts by only about 4 meV which is about 1 nm shift of a 565 nm absorbance. But the exchange has a large effect on nanocrystal photoluminescence quantum efficiency. Therefore, the intensity change of the photoluminescence can be used to study in situ the exchange of surface ligands using this technique. The exchange of surface ligands has been realized in different semiconductor nanocrystals.<sup>16,17,18</sup> However, besides several NMR studies the in situ study of the dynamics of this exchange process is still lacking. Single nanocrystal fluorescence microscopy can be used to acquire more insights.

Similar to the effects of exchange of surface passivation, surface defects, such as vacancies, also can affect the photoluminescence emission of semiconductor nanocrystals.<sup>24,25</sup> For example, both oxygen vacancies in metal oxide perovskites and photo-annealing with oxygen are reported to have big effect on the performance of photoluminescence emission of perovskite.<sup>24,25</sup> Therefore, with single nanocrystal fluorescence microscopy method we can study the effects of oxygen and oxygen vacancy on the performance of metal halide/oxide perovskite. To control the oxygen contact, the accessory of environmental chamber can be used. Certain methods are needed to introduce oxygen vacancies into metal oxide perovskite. For example, in tungsten oxide system H<sub>2</sub>O<sub>2</sub> is used to oxidize and introduce surface oxygen vacancies into the system. We can intentionally introduce certain surface defects to semiconductor nanocrystal to study the

change of photoluminescence emission. This method may give more direct evidence to link surface defects and the performance of semiconductor nanocrystals.

In our previous study of CdTe quantum dot thin films, we showed that the stability of CdTe thin film can be increased by atomic layer deposition (ALD) of a thin layer of alumina ( $\text{Al}_2\text{O}_3$ ).<sup>26</sup> Low stability is also a serious problem for lead halide perovskite, which limits their applications. Single nanocrystal fluorescence microscopy can also be used to study the degradation of semiconductor nanocrystals, which would feature a turn-off event of photoluminescence emission of nanocrystals. It can also study the effects of various stabilizing methods on semiconductor nanocrystals, such as ALD coating of layers of a more stable material.

## 5.4 References

1. An, C.; Wang, J.; Jiang, W.; Zhang, M.; Ming, X.; Wang, S.; Zhang, Q., Strongly visible-light responsive plasmonic shaped AgX:Ag (X = Cl, Br) nanoparticles for reduction of CO<sub>2</sub> to methanol, *Nanoscale* **2012**, 4(18), 5646-5650.
2. Asi, M. A.; He, C.; Su, M.; Xia, D.; Lin, L.; Deng, H.; Xiong, Y.; Qiu, R.; Li, X., Photocatalytic reduction of CO<sub>2</sub> to hydrocarbons using AgBr/TiO<sub>2</sub> nanocomposites under visible light, *Catal. Today* **2011**, 175(1), 256-263.
3. Zhang, X.; Li, J.; Lu, X.; Tang, C.; Lu, G., Visible light induced CO<sub>2</sub> reduction and Rh B decolorization over electrostatic-assembled AgBr/palygorskite, *J. Colloid Interface Sci.* **2012**, 377, 277-283.
4. Cai, B.; Wang, J.; Han, D.; Gan, S.; Zhang, Q.; Wu, Z.; Niu, L., Ternary alloyed AgCl<sub>x</sub>Br<sub>1-x</sub> nanocrystals: facile modulation of electronic structures toward advanced photocatalytic performance, *Nanoscale* **2013**, 5(22), 10989-10995.
5. Cai, B.; Wang, J.; Gan, S.; Han, D.; Wu, Z.; Niu, L., A distinctive red Ag/AgCl photocatalyst with efficient photocatalytic oxidative and reductive activities, *J. Mater. Chem. A* **2014**, 2(15), 5280-5286.
6. Zhu, M.; Chen, P.; Liu, M., Ag/AgBr/Graphene oxide nanocomposite synthesized via oil/water and water/oil microemulsions: a comparison of sunlight energized plasmonic photocatalytic activity, *Langmuir* **2012**, 28(7), 3385-3390.

7. Hu, C.; Peng T.; Hu X.; Nie, Y.; Zhou, X.; Qu, J.; He, H., Plasmon-induced photodegradation of toxic pollutants with Ag–AgI/Al<sub>2</sub>O<sub>3</sub> under visible-light irradiation, *J. Am. Chem. Soc.* **2010**, 132(2), 857-862.
8. Choi, M.; Shin, K. H.; Jang, J., Plasmonic photocatalytic system using silver chloride/silver nanostructures under visible light, *J. Colloid Interface Sci.* **2010**, 341(1), 83-87.
9. An, C.; Peng, S.; Sun, Y., Facile synthesis of sunlight-driven AgCl: Ag plasmonic nanophotocatalyst, *Adv. Mater.* **2010**, 22(23), 2570-2574.
10. Dong, R.; Tian, B.; Zeng, C.; Li, T.; Wang, T.; Zhang, J., Ecofriendly synthesis and photocatalytic activity of uniform cubic Ag@AgCl plasmonic photocatalyst, *J. Phys. Chem. C.* **2013**, 117(1), 213-220.
11. Ye, L.; Liu, J.; Gong, C.; Tian, L., Peng, T.; Zan, L., Two different roles of metallic Ag on Ag/AgX/BiOX (X = Cl, Br) visible light photocatalysts: surface plasmon resonance and Z-scheme bridge, *ACS Catal.* **2012**, 2(8), 1677-1683.
12. Wang, Y.; Sun, L.; Fugetsu, B., Morphology-controlled synthesis of sunlight-driven plasmonic photocatalysts Ag@AgX (X = Cl, Br) with graphene oxide template, *J. Mater. Chem. A* **2013**, 1, 12536-12544.
13. Routzahn, A. L.; Jain, P. K., Single-nanocrystal reaction trajectories reveal sharp cooperative transitions, *Nano Lett.* **2014**, 14, 987-992.
14. Routzahn, A. L.; Jain, P. K., Luminescence blinking of a reacting quantum dot, *Nano Lett.* **2015**, 15, 2504-2509.

15. Protesescu, L.; Yakunin, S.; Bodnarchuk, I. M.; Krieg, F.; Caputo, R.; Hendon, H. C.; Yang, R.; Walsh, A.; Kovalenko, V. M., Nanocrystals of cesium lead halide perovskites (CsPbX<sub>3</sub>, X = Cl, Br, and I): novel optoelectronic materials showing bright emission with wide color gamut, *Nano Lett.* **2015**, 15(6), 3692-3696.
16. Ji, X.; Copenhaver, D.; Sichmeller, C.; Peng, X., Ligand bonding and dynamics on colloidal nanocrystals at room temperature: the case of alkylamines on CdSe nanocrystals, *J. Am. Chem. Soc.* **2008**, 130(17), 5726-5735.
17. Munro, A. M.; Ginger, D. S., Photoluminescence quenching of single CdSe nanocrystals by ligand adsorption, *Nano Lett.* **2008**, 8(8), 2585-2590.
18. Munro, A. M.; Jen-La Plante, I.; Ng, M. S.; Ginger, D. S., Quantitative study of the effects of surface ligand concentration on CdSe nanocrystal photoluminescence, *J. Phys. Chem. C* **2007**, 111(17), 6220-6227.
19. Anderson, N. C.; Hendricks, M. P.; Choi, J. J.; Owen, J. S., Ligand exchange and the stoichiometry of metal chalcogenide nanocrystals: spectroscopic observation of facile metal-carboxylate displacement and binding, *J. Am. Chem. Soc.* **2013**, 135(49), 18536-18548.
20. Frederick, M. T.; Amin, V. A.; Weiss, E. A., Optical properties of strongly coupled quantum dot–ligand systems, *J. Phys. Chem. Lett.* **2013**, 4(4), 634-640.
21. Koole, R.; Liljeroth, P.; de Mello Donegá, C.; Vanmaekelbergh, D.; Meijerink, A., Electronic coupling and exciton energy transfer in CdTe quantum-dot molecules, *J. Am. Chem. Soc.* **2006**, 128(32), 10436-10441.

22. Koole, R.; Luigjes, B.; Tachiya, M.; Pool, R.; Vlugt, H.; de Mello Donegá, C.; Meijerink, A.; Vanmaekelbergh, D., Differences in cross-link chemistry between rigid and flexible dithiol molecules revealed by optical studies of CdTe quantum dots, *J. Phys. Chem. C* **2007**, 111(30), 11208-11215.
23. Buckley, J. J.; Couderc, E.; Greaney M. J.; Munteanu, J.; Riche, C. T.; Bradforth, S. E.; Brutchey, R. L., Chalcogenol ligand toolbox for CdSe nanocrystals and their influence on exciton relaxation pathways, *ACS Nano* **2014**, 8(3), 2512-2521.
24. Tian, Y.; Peter, M.; Unger, E.; Abdellah, M.; Zheng, K.; Pullerits, T.; Yartsev, A.; Sundström, V.; Scheblykin, I. G., Mechanistic insights into perovskite photoluminescence enhancement: light curing with oxygen can boost yield thousandfold, *Phys. Chem. Chem. Phys.* **2015**, 17(38), 24978-24987.
25. Hwang, H. Y., Oxygen vacancies shine blue, *Nat. Mater.* **2005**, 4, 803-804.
26. Yin, B.; Sadtler, B.; Berezin, M. Y.; Thimsen, E., Quantum dots protected from oxidative attack using alumina shells synthesized by atomic layer deposition, *Chem. Commun.* **2016**, 52(74), 11127-11130.
27. Wang, H.; Yang, J.; Li, X.; Zhang, H.; Li, J.; Guo, L., Face-dependent photocatalytic properties of AgBr nanocrystals, *Small* **2012**, 8, 2802-2806.



# Appendix

## Matlab Scripts for Data Analysis

### Script for Waiting time Analysis of Trajectories of Single Nanocrystals

```
data = xlsread(filename.xlsx');
% plot(data(:,1),data(:,161));
% xlim([198,202]); % second column
% xlim([250,255]); % second column
turnon = 0;
[sz1 sz2] = size(data);
for r = 3:sz2
    timeatfourhundred = 1;
    noise = data(1:100,r);
    normdis = fitdist(noise,'Normal');
    threshold = normdis.mu+6*normdis.sigma;
    while data(timeatfourhundred,r)<= threshold
        timeatfourhundred = timeatfourhundred +1;
        if timeatfourhundred == sz1
            break;
        end
    end
    turnon(r-2)=data(timeatfourhundred,1);
end
filename = 'resultfilename.xlsx';
xlswrite(filename,turnon);
```

## Script for Switching time Analysis of Trajectories of Single Nanocrystals

```
data = xlsread('filename.xlsx');
% plot(data(:,1),data(:,161));
% xlim([198,202]); % second column
% xlim([250,255]); % second column

[sz1 sz2] = size(data);
for r = 3:sz2

    signal1 = data(1:200,r); %baseline values before reaction
    signal2 = data((sz1-200):sz1,r); % baselne after reaction
    base1 = fitdist(signal1,'Normal');
    base2 = fitdist(signal2,'Normal');
    Iin = base1.mu;
    Ifin = base2.mu;
    Idiff = Ifin-Iin;
    halfintensity = 1;
    while data(halfintensity,r)<= (0.5*(Iin+Ifin))
        halfintensity = halfintensity +1;
    end
    thalf = data(halfintensity,1);

    modelfun = @(b,t)(Iin+Idiff./(1+exp(-b(1).*t+b(2))));
    b_fitted = nlinfit(data(:,1),data(:,r),modelfun,[2,2]); %
    initial value is 'b(1)=2 and b(2)=2'
    b(1,r-2) = b_fitted(1); %writhe the fitted b to a matrix
    b(2,r-2) = b_fitted(2); % is b(1) and second row is b(2)
    figure(r-2)

plot(data(:,1),data(:,r),'*',data(:,1),modelfun(b_fitted,data(:,
1)), 'r')%plot the figure
end
filename = 'switching time D 0.2mg part 3.xlsx';
xlswrite(filename,b);
```